

Multidimensional Nonlinear Femtosecond Spectroscopy of Biological Molecules

*A thesis submitted for the degree of
Doctor of Philosophy*

by

Craig Norman Lincoln

*Centre for Atom Optics and Ultrafast Spectroscopy
Swinburne University of Technology
Melbourne, Australia*

April 29, 2007

for James R. Colless (1954-2001)
a man who inspired living life to the full
and the importance of knowledge.

I am among those who think that science has great beauty. A scientist in his laboratory is not only a technician: he is also a child placed before natural phenomena which impress him like a fairy tale.

— *Marie Curie (1867-1934)*

Abstract

In this thesis photon echo spectroscopy is extended by measuring the spectrum of the scattered signal (spectrally resolved photon echo) and by using two different wavelengths for the different applied laser pulses (two-colour photon echo), in order to investigate the ultrafast dynamics in biological molecules. To characterise the signal response of the spectrally resolved measurement a theoretical study using the Multimode Brownian Oscillator (MBO) model is performed. The MBO model describes the interaction of the analyte of interest and the surrounding environment in terms of a time-dependent correlation function $M(t)$. The inverse linewidth of the measured signal spectra is found to correspond well with the temporal width of the photon echo pulse and an analytical fit to the signal is able to reasonably describe both the coupling strength and the dynamics of the time-dependent correlation function.

The spectrally resolved and two-colour measurement techniques are applied to a laser dye, rhodamine 101, to characterise the signal response (photophysics) of a molecule that does *not* undergo a chemical reaction. The measurement of the nonlinear signal spectra for rhodamine 101 proved invaluable in identifying the different underlying photophysical processes that would otherwise have been difficult given only integrated intensity data. Another interesting result of measuring the signal spectra is the ability to characterise separately the ground and excited state dynamics. Information about the dynamics of fast processes that are otherwise difficult to determine can be extracted using the two-colour technique. The combination of the spectrally resolved and two-colour techniques showed that AC-Stark effects are present and need to be considered when performing photon echo (transient grating) experiments.

The new technique, two-colour spectrally resolved photon echo spectroscopy, is applied to the biological system carbonmonoxy myoglobin (MbCO). Upon illumination MbCO undergoes a reaction where the carbonyl complex dissociates to form deoxy-myoglobin (deoxy-Mb). This study provides supporting evidence for the mechanism and the dynamics of the initial steps involved in this photodissociation reaction. We show that a change in spin state from the low spin bound state to the high spin unbound state occurs in the first 200 fs after excitation: the photophysics of photodissociation involve a second (intermediate) excited state with a lifetime of around 200 fs for MbCO and *not* vibrational cooling of a hot ground state as proposed in a previous model. Other photophysical time scales are also estimated: the Fe-CO bond breakage occurs within 25 fs and the lifetime of the Q-band levels is 35 fs.

Acknowledgements

I would like to thank past and present members of the Centre for Atom Optics and Ultrafast Spectroscopy. Specifically, I would like to thank Peter Hannaford for giving me the opportunity to do a PhD, introducing me to a particularly interesting field of science that I love and generally providing guidance and support. Jeremy Bolger for providing me with a basic understanding of optics in the early days, Lap Van Dao for his expertise in nonlinear spectroscopy and his patience, Barbara McKinnon and Brian Dalton for their invaluable support in developing my understanding of quantum mechanics and the theory outlined in thesis. There are of course more people, Wayne Rolands, Falk Scharnberg, Heath Kitson, Damian Bird, Drew Morrish, Shannon Whitlock, Breton Hall, Petriisa Eckle, Paul Stoddart and more who provided moral support, general discussions, knowledge and lunchtime partners.

Other Swinburne University people of note are Margret Wong who provided a great deal of expertise in organic chemistry that proved invaluable in bridging the gap between measured observables and chemical structure and for her always fresh face and positive attitude. Greg Lonergan, may he rest in peace, who gave me my first opportunities in research and Mark Luckey and Edmund Lascaris who help to guide me during the same period.

Jaro Sperling and Harold Kaffmann who showed me the best of Vienna and exposed me to the broad range of available femtosecond spectroscopic techniques including photon echo peak shift. Delmar Larsen also deserves thanks for putting me straight on some of the more technical details of the peak shift technique. The experience gain from these people came at a critical time of my candidature and opened my eyes to the potential of the field.

Trevor Smith for seeing my potential and providing me with employment

for the last years and for his assistance along with Damian Bird in the final days of the thesis.

To my family and friends. Together they have dragged me up when I was down, given me perspective when all I could see was work and pushed me to finish.

Last but definitely not least, a special thanks goes to my Mother. She was there when it was needed and her gentle touch while pushing me to finish was greatly appreciated.

Declaration

This thesis contains no material which has been accepted for the award of any other degree or diploma. To the best of my knowledge, this thesis contains no material previously published or written by another person except where due reference is made in the text of the thesis. All work presented is primarily that of the author. Prof. Lap Van Dao performed the measurements of the Rhodamine 101 experimental data though all analytical and theoretical fitting was performed by the author.

.....

Craig N. Lincoln

April 29, 2007

Contents

Abstract	i
Acknowledgements	iii
Declaration	v
Contents	vi
List of Figures	viii
List of Tables	xi
1 Introduction	1
1.1 Dynamics of Physiological Chemistry	2
1.2 Linear Spectra, Homogeneous and Inhomogeneous Broadening	3
1.3 Ultrafast Coherence Techniques: Photon Echo Spectroscopy .	8
1.4 Thesis Outline	13
2 Theoretical Background	15
2.1 Introduction	16
2.2 Theoretical Model	19
2.2.1 Response Function Formalism	19
2.2.2 Multimode Brownian Oscillator and Cumulant Ex- pansion	23
2.2.3 Limiting Cases of $M(t)$: Discrete and Continuous Modes	27
2.3 Physical Significance of Response Functions and Feynman Di- agrams	30
2.4 Relationship Between Measured Signals and Third-Order Po- larisation	33
2.4.1 Integrated Signal	33

2.4.2	Spectrally Resolved Signal	33
2.4.3	Special Cases	33
2.5	Spectrally Resolved Transient Grating Signals	34
2.5.1	Relationship to the Correlation Function	34
2.5.2	Laser Pulse Width Dependence of Spectrally Resolved Transient Grating Signals	38
2.5.3	Inverse Linewidth Laser Wavelength and Linear Chirp Dependence	42
2.6	Summary	42
3	Experimental Details	44
3.1	The Femtosecond Ti:Sapphire Laser System	45
3.2	Experimental Arrangement	45
3.3	Sample Preparation	50
3.4	Data Analysis	51
3.4.1	Numerical Calculations	51
3.4.2	Inverse Linewidth, Third-Order Polarisation Tempo- ral Width and Peak Shift	52
3.4.3	Analytical Fitting	53
4	Spectrally-Resolved Photon Echoes of a Laser Dye	56
4.1	Introduction	57
4.2	Spectrally Resolved Transient Grating of Rhodamine 101	60
4.2.1	Laser-Wavelength Dependent One-Colour Spectra	60
4.2.2	Laser-Wavelength Dependent Two-Colour Spectra	69
4.2.3	Laser-Wavelength Dependence and Effect of Rapid In- traband Population Relaxation	77
4.3	Summary	94
5	Spectrally-Resolved Photon Echoes of Heme-Based Bio- logical Molecules	96
5.1	Introduction	97
5.2	Biological Function and Crystal Structure of Heme Proteins	98
5.3	Electronic and Vibrational Spectra	102
5.4	Photophysics of Heme-CO photolysis	107
5.4.1	Vibrationally Excited <i>Hot</i> Ground State Model	107
5.4.2	Multiple Excited State Model	110

5.5	One-Colour Spectrally Resolved Photon Echoes of Deoxy-Mb and MbCO	114
5.5.1	Results	115
5.5.2	Discussion	122
5.5.3	Additional Features of One-Colour Spectrally Resolved Photon Echoes	133
5.5.4	Summary	135
5.6	Two-Colour Spectrally Resolved Transient Grating of Heme Proteins	136
5.6.1	Results	136
5.6.2	Discussion	142
5.7	Summary	144
6	Summary and Future Prospects	145
	Bibliography	150
	Appendices	2
A	Example Code	2
A.1	RunP3_Calc	3
A.2	P3_t_t12_t23.m	5
A.3	RIRIV.m	8
A.4	RIIRIII.m	12

List of Figures

1.1	Portrait of Albrecht von Haller the “Father of Physiology” (1708-1777).	1
1.2	Schematic diagram of a standard absorption and fluorescence measurement. Dashed lines indicate data processing to present the data as spectra.	4

1.3	Effect of homogeneous and inhomogeneous broadening on the absorption lineshape.	6
1.4	Schematic of coherent techniques involving one, two and three pulses.	10
2.1	Flow chart showing the theoretical framework of the response function formalism and the Multimode Brownian Oscillator model.	17
2.2	(a) Graphic representation of the MBO model. (b) Displaced Harmonic Oscillator.	24
2.3	(a) Pulse sequence for three-pulse photon echo including relevant delay times t_{12} and t_{23} as indicated. (b) Double-sided Feynman diagrams used for a perturbative description of the third-order polarisation $P^{(3)}$	32
2.4	Calculated spectrally resolved transient grating results.	36
2.5	Calculated results of the effect of laser pulse width on inverse linewidth.	39
2.6	Calculated inverse linewidth	41
3.1	Experimental arrangement for photon echo and transient grating experiments showing the three beam lines and two optical delay lines. Enlargement shows the cross-section of the arrangement of the three laser pulses were arranged and the three possible signal wavevectors.	46
3.2	Measured transient grating intensity for carbonmonoxy myoglobin (solid line) and the sample cell filled with water (dashed line).	49
4.1	Rhodamine 101 absorption and fluorescence spectra and chemical structure	57
4.2	One-colour spectrally resolved transient grating spectra of rhodamine 101	61
4.3	Time-integrated transient grating spectra of rhodamine 101	62
4.4	Intensity, centre frequency and inverse linewidth plots for three laser wavelengths (a) 560 , (b) 575 and (c) 590 nm.	64

4.5	One-colour transient grating centre frequencies measured using 575 nm laser pulses of two signal channels as labelled. Solid lines are analytical fits. See text for details.	69
4.6	Two-colour spectrally resolved transient grating spectra of rhodamine 101	70
4.7	Two-colour transient grating integrated intensity curves of rhodamine 101	71
4.8	Energy level diagrams for rhodamine 101	78
4.9	CSRS and CARS ladder diagrams	82
4.10	Schematic representation of dynamics Stoke shift	84
4.11	Two-colour transient grating integrated intensity curves from literature	86
4.12	Energy level diagrams of rhodamine 101	89
4.13	AC-Stark light shifts and broadening	91
5.1	Crystal structure of myoglobin	101
5.2	Absorption spectra of deoxy-Mb and MbCO and heme energy level diagram	103
5.3	Proposed photodissociation mechanism from literature	108
5.4	Multiple excited state model adapted from literature	111
5.5	One-colour photon echo and spectrally resolved transient grating of MbCO and deoxy-Mb	117
5.6	One-colour photon echo peak shift and spectrally resolved transient grating spectral width results for MbCO and deoxy-Mb	118
5.7	One-colour integrated transient grating intensity of deoxy-Mb and MbCO at 600 nm.	119
5.8	One-colour difference centre frequency of MbCO compared to deoxy-Mb at 600 nm	120
5.9	Transient grating intensity, centre frequency and spectral width results for MbCO measured using 585 nm laser pulses	121
5.10	Electronic structure of MbCO model complex as a function of the Fe-CO bond distance	124
5.11	Schematic of structural effect of spin state change	132
5.12	Spectrally resolved one-colour photon echo results for deoxy-Mb measured using 600 nm laser pulses	134

5.13	Spectral width results from data presented in Fig. 5.12	135
5.14	Two-colour spectrally resolved transient grating spectra of deoxy-Mb and MbCO as indicated.	137
5.15	Two-colour transient grating intensity results for deoxy-Mb and MbCO	137
5.16	Difference centre frequency result taken from the two-colour centre frequency results for deoxy-Mb and MbCO. See text for details.	139
5.17	Two-colour transient grating spectral width signals for deoxy-Mb and MbCO	139
5.18	Two-colour transient grating spectral width signals with the exponential components removed for deoxy-Mb and MbCO. Matrix pencil method fits shown as solid lines and the retrieved Fe-His component included as an offset solid line. The retrieved Fourier spectra of the fit are shown in the right column.	141

List of Tables

2.1	Parameters of the fits presented in Fig. 2.4.	37
2.2	Parameters for analytical fits to the inverse linewidth $\Delta t_{\text{FWHM}}(t_{23})$ for four different laser pulse widths 15, 30, 55 and 80 fs shown in Fig. 2.5	40
3.1	Signal Wavevectors, pulse sequences and resultant response functions for resonant four-wave mixing.	47
4.1	Parameters for theoretical fits to the data presented in Figs. 4.2 and 4.4	67
4.2	Parameters for analytical fits to the data presented in Figure 4.5	68

4.3	Parameters of analytical fit to one- and two-colour transient grating integrated intensity results presented in Figure 4.7.	73
4.4	Results of analytical fits of Voigt profiles to the time-integrated one- and two-colour spectra.	75
4.5	Experimental transition wavelengths for one- and two-colour transient grating spectra (reproduced from Table 4.2) compared to those calculated taking into account the AC-Stark effect	92
5.1	Resonance Raman modes for deoxy-Mb and MbCO from literature	104
5.2	Calculated mode assignments based on measured Nuclear Resonance Vibrational Spectroscopy of iron normal modes quoted in wavenumbers (cm^{-1}) for heme model complexes Fe(TPP)(2-MeHIm) and Fe(TPP)(CO)(1-MeIm) of deoxy- and carbonmonoxy-heme proteins, respectively	105
5.3	Least-square fit results for measured one-colour peak shift and spectral width signals of MbCO.	115
5.4	Least-square fit results for measured one-colour transient grating intensity (Int), peak shift (PS) and spectral width (PW) for deoxy-Mb (Mb) and MbCO at 600 nm.	116
5.5	Exponential components of matrix pencil method fits to transient grating intensity (Int), spectral width (PW) and centre frequency (CF) for MbCO measured using 585 nm laser pulses.	122
5.6	Results of least squares fitting of two-colour transient grating intensity and spectral width for deoxy-Mb (Mb) and MbCO	140

Chapter 1

Introduction



Figure 1.1: Albrecht von Haller the “Father of Physiology” (1708-1777) revolutionized our knowledge of blood flow and heart action. He clarified the relation between respiration and blood flow. He explained nerve action in muscles. He gave us new insights into human reproduction and birth defects [1]. Image taken from [2].

1.1 Dynamics of Physiological Chemistry

The desire to understand plant and animal physiology has been the endeavour of many scientists since the early work of the two fathers of physiology Erasistratus of Alexandria (350-250 B.C.) and Albrecht von Haller of Berne (1708-1777) [3–5]. While many physiological chemical reactions have been discovered there are still many subtleties that are not understood as evidenced recently by the discovery of nitric oxide as a vascular signalling molecule, for which Furchgott, Ignarro and Murad were awarded a Nobel prize in 1998 [6]. Studying the dynamics of biochemical reactions makes possible the discovery of subtle synergies and new pathways. However, the nature of the surrounding environment is often interconnected with reaction rate processes and in some cases determines whether reactions occur or not.

Examples of the surrounding environment include liquid solvents and proteins in the form of a globin, enzyme or antibody which can significantly inhibit or enhance the physiological reactions, i.e., a prosthetic group embedded in a globin while still having contact with the surrounding liquid media. In this scenario there is coupling between the prosthetic group and the associated protein, the prosthetic group and the solvent molecules, as well as the protein and the solvent molecules. This complex picture is common for biochemical systems and creates a need for an easy to perform and interpret measurement technique which will provide enough degrees of freedom to unravel the many different contributions to a signal.

One technique that meets this requirement is femtosecond photon echo spectroscopy, which is ideally suited to studies in the liquid state where broadening processes can often dominate and interfere when using other optical methods based on absorption measurements [7–16]. Photon echo spectroscopy is one of a class of multidimensional nonlinear coherent tech-

niques which has seen major theoretical and experimental developments in the last ten years [17–24]. These developments have culminated in techniques designed in the optical regime to probe and discriminate electronic, vibrational, solvation and reaction dynamics for complex molecular systems in solution.

In this Chapter the various types of solute/solvent interactions that can occur are introduced and their effect on linear spectra is discussed. This is followed by a brief description of the various forms of the photon echo technique and how it overcomes some of the problems for studying biochemical and chemical reactions in solution. The Chapter finishes with a brief outline of this thesis.

1.2 Linear Spectra, Homogeneous and Inhomogeneous Broadening

The simplest spectroscopic technique is an absorption measurement. In a typical absorption experiment the sample is subjected to a beam of light of intensity I_0 and the attenuated intensity I_a is measured at the detector and the absorbance $A = \log(I_0/I_a)$ is plotted against a scan of the frequency ω (Fig. 1.2). Closely related is a measurement of the spontaneous emission from the sample performed by measuring the fluorescent radiation I_f as a function of frequency ω (Fig. 1.2). The resultant absorption and fluorescence spectra can reveal information about the molecules in the sample from the position, intensity and width of the peaks. The position and intensity of the peaks can be directly related to the Franck-Condon transition probability and the difference between the absorption and fluorescence maxima represents the *Stokes shift* (2λ). The width and shape of the peaks carries

information about the local environment of the sample molecules as well as the intramolecular dynamics. It will become apparent that there are various limitations in interpreting the intramolecular dynamics of the sample molecules and intermolecular dynamics of local interactions from the width of absorption and fluorescence spectra.

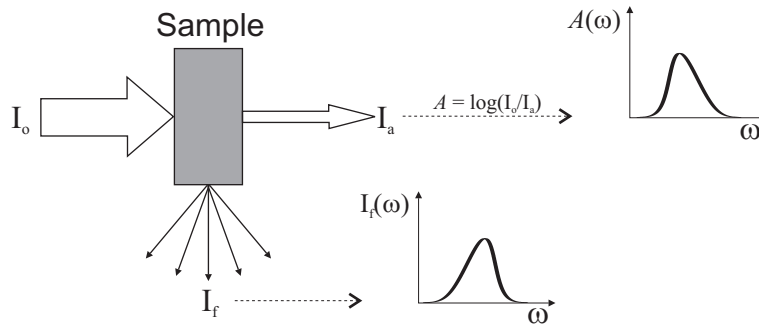


Figure 1.2: Schematic diagram of a standard absorption and fluorescence measurement. Dashed lines indicate data processing to present the data as spectra.

The following describes the concepts of line broadening and optical dephasing as they pertain to systems comprising an ensemble of two-level systems with an energy separation $\hbar\omega_{eg}^o$. Using the theoretical description presented in Chapter 2, based on the Multimode Brownian Oscillator (MBO) model [19], the dynamics affecting the width of the absorption and fluorescence spectra are captured in the time-dependent modulation of the energy separation of the molecular levels of the sample:

$$\delta\omega_{eg}^o(t) = \omega_{eg}^o(t) - \langle\omega_{eg}^o\rangle, \quad (1.1)$$

where $\langle\omega_{eg}^o\rangle$ represents the ensemble-average of the macroscopic system. The ensemble-averaged energy level fluctuations can be expressed in the form of

a time-dependent correlation function:

$$M(t) = \frac{\langle \delta\omega_{eg}^o(0) \delta\omega_{eg}^o(t) \rangle}{\langle (\delta\omega_{eg}^o)^2 \rangle}. \quad (1.2)$$

The time-dependent correlation function $M(t)$ is related to the line broadening function $g(t)$, which in turn can be related to the linear absorption $I_a(\omega)$ and fluorescence $I_f(\omega)$ lineshapes as follows [19](see Chapter 2):

$$I_a(\omega) = \frac{1}{\pi} Re \int_0^\infty dt \exp[i(\omega - \omega_{eg})t] \exp[-g(t)], \quad (1.3)$$

$$I_f(\omega) = \frac{1}{\pi} Re \int_0^\infty dt \exp[i(\omega - \omega_{eg} + 2\lambda)t] \exp[-g^*(t)], \quad (1.4)$$

where $\omega_{eg} \equiv \omega_{eg}^o - \lambda$ is the first moment of absorption, 2λ is the Stokes shift and $g^*(t)$ is the complex conjugate of $g(t)$.

Now consider an ensemble of identical oscillators that do not interact with the surrounding environment or each other. The system is free to evolve in time and will be correlated for long times, limited only by the natural lifetime τ_e approximately 10^{-8} s (typically). In the time domain (for times $\ll \tau_e$) the system will evolve as an undamped sinusoid which would approach an infinitesimally narrow lineshape in the frequency domain after transformation (Fig. 1.3).

If the same ensemble is coupled to a weakly interacting local environment, the local environment will cause the system to depart from a perfect sinusoidal behaviour as each two-level system interacts differently with the surrounding environment. This causes each oscillator in the ensemble become out of phase, a process called optical dephasing. The system now begins to lose the long time correlation seen in the previous case and decays to zero as $t \rightarrow \tau_e$. Thus, the process of optical dephasing of the oscillators in the ensemble causes damping in the time domain and broadens the

absorption and fluorescence spectra. The two major types of dephasing or broadening mechanisms for molecules in solution are homogeneous and inhomogeneous broadening (Fig. 1.3).

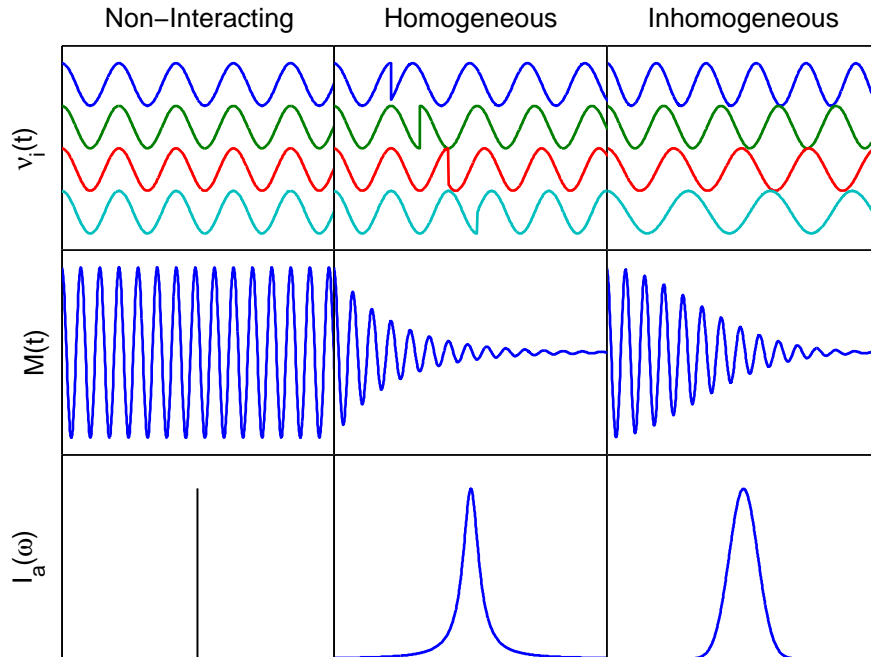


Figure 1.3: Sample coordinate trajectories $\nu_i(t)$, time-dependent correlation function $M(t)$ and absorption spectra $I_a(\omega)$ are depicted for three hypothetical two-level systems. A system of non-interacting harmonic oscillators is shown in the left column, an homogeneously broadened system in the middle column and an example of an inhomogeneously broadened system in the right column. Figure adapted from [25].

Two typical cases of oscillators interacting with a liquid solvent will now be considered. In the first scenario the surroundings of each oscillator change rapidly to produce a similar environment for each oscillator. The time evolution of each oscillator appears more stochastic in this case than in the natural lifetime limit due to the interaction between the oscillators and their surroundings changing rapidly with time. The optical dephasing in this case is said to be homogeneous and typically produces an exponential decay

in the time-dependent correlation function $C(t)$ which results in a Lorentzian form of the broadened absorption and fluorescence lineshape (Fig. 1.3).

Dynamic interactions between a two-level system and its environment can be inelastic, in which an exchange of energy occurs, or elastic, where no energy is exchanged but the frequency is modulated in some way. The optical dephasing from inelastic collisions which contributes to the decay of the time-dependent correlation function is referred to as energy relaxation and is typically characterised by an exponential decay rate of $1/2T_1$, where T_1 is the population relaxation time. The term pure dephasing is used to describe the effect of elastic interactions on the decay of the correlation function, or equivalently the broadening of the spectrum. The decay of the time-dependent correlation function due to pure dephasing is often characterised by an exponential decay rate of $1/T_2^*$, where T_2^* is the pure dephasing time. The decay rates of energy relaxation and pure dephasing are combined to produce a total homogeneous dephasing rate,

$$\frac{1}{T_2} = \frac{1}{2T_1} + \frac{1}{T_2^*}. \quad (1.5)$$

It should be noted that the dynamical line broadening terminology introduced here is also applied to systems where decay rates of correlation functions are not exponential.

In the second hypothetical scenario each oscillator has a slightly different local environment, which does not change significantly over the course of time. In this case, the interaction between the inhomogeneous environments and the oscillators results in a shift in the energy separation away from the unperturbed energy $\hbar\omega_{eg}^o$, i.e., each frequency shift is different given that our ensemble of oscillators experience different static environments. As the

oscillators evolve in time they still exhibit sinusoidal behaviour but oscillate at different frequencies due to their inhomogeneous surroundings. Assuming the distribution of frequencies is Gaussian, the time-dependent correlation function will have a Gaussian decay which results in a Gaussian broadened absorption and fluorescence lineshape when transformed (Fig. 1.3). This hypothetical scenario is a limiting case of an inhomogeneously broadened system.

An absorption or fluorescence spectrum of a sample in a *real* solution may have both homogeneous and inhomogeneous characteristics. One could imagine a hypothetical two-level system between the two limiting cases in which a distribution of inhomogeneous environments arises from extremely slow solvent motions while dynamical interactions from faster solvent motions occur within each environment. Unfortunately, the linear response of a system does not distinguish between dephasing processes of different time scales. The advantage of some nonlinear techniques is their ability to selectively eliminate inhomogeneous contributions and extract only the part for which dynamical (homogeneous) interactions dominate.

1.3 Ultrafast Coherence Techniques: Photon Echo Spectroscopy

Photon echo spectroscopy belongs to the class of multidimensional nonlinear optical techniques that are somewhat analogous to multidimensional nuclear magnetic resonance techniques. The techniques hold promise for providing detailed structural and dynamical characterisation of complex molecular systems in solution. The following description of the photon echo technique is based on a theoretical treatment outlined by Zinth and Kaiser [23].

In the simplest coherence experiment one short laser pulse with area¹ $A = \pi/2$ impinges upon the sample. This pulse creates optical coherence between the ground and excited states which is measured as a macroscopic electric polarisation P . This polarisation P immediately begins to dephase due to population relaxation, pure dephasing and an inhomogeneous distribution of frequencies. Figure 1.4(a) shows a schematic diagram of the decay of the polarisation $P(t)$ as a function of time t . Two profiles for the decay of the polarisation are shown. First, the long time component shows the homogeneous component decaying exponentially with a dephasing time T_2 , and second a fast decay due to interference between an inhomogeneous distribution of resonant frequencies, where information about T_2 is essentially lost.

In a two-pulse photon echo experiment the first pulse ($A = \pi/2$) similarly creates a macroscopic electric polarisation, which immediately begins to dephase. However, the arrival of the second pulse with pulse area $A = \pi$ at a variable delay time t_{12} causes the dephasing of the polarisation $P^{(3)}(t_{12}, t)$ ² to be reversed until the system rephases at $t = t_{12}$, where time zero corresponds to the arrival of the second pulse (Fig. 1.4(b)). The rephasing at $t = t_{12}$ removes the effects of inhomogeneous broadening. However, fast frequency fluctuations cause irreversible homogeneous dephasing, and therefore there is not perfect rephasing at time $t = t_{12}$.

The dependence on the delay time, t_{12} , of the time-integrated intensity of $P^{(3)}(t_{12}, t)$ provides a probe of the time scale of the homogeneous dephasing dynamics (T_2). The temporal behaviour of the homogeneously decaying

¹The area A of the pulse is related to the Rabi frequency Ω of the system by $A = \int dt \Omega$, where $\Omega = \mu_{ge} E_0 / \hbar$ and E_0 is the electric field operator of the applied laser pulse and μ_{ge} is the transition dipole matrix element.

²Here $P^{(3)}$ denotes that only the third-order component of the polarisation is being considered. This will be discussed in more detail in Chapter 2.

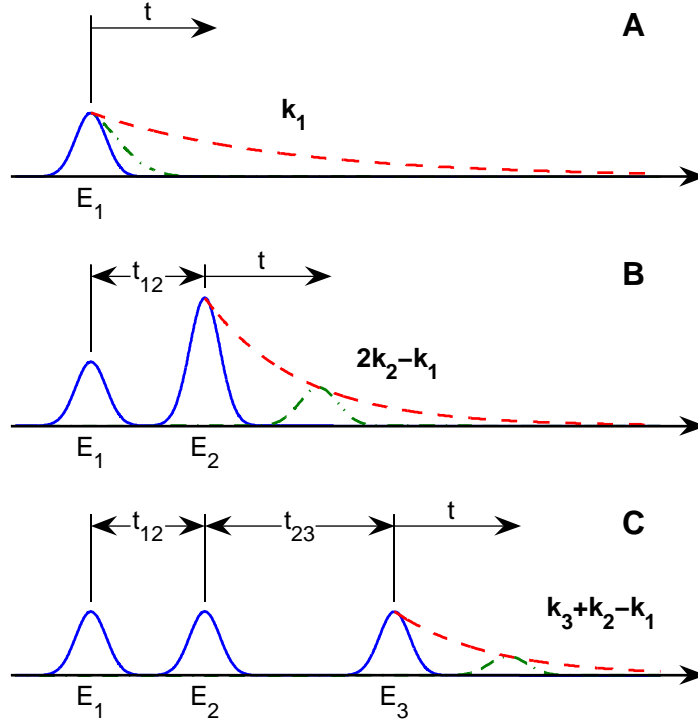


Figure 1.4: Schematic of coherent techniques involving one, two and three pulses. The electric field pulses (solid peaks) excite the sample. The resulting coherent signal is shown for homogeneously broadened transitions (dashed line), and for inhomogeneously broadened transitions (dotted and dashed line). (a) A single excitation pulse E_1 with wavevector \vec{k}_1 . Homogeneously broadened transitions lead to an exponential decay with dephasing time T_2 , while interference of an inhomogeneous distribution of resonant frequencies causes a faster decay. (b) Two excitation pulses E_1 and E_2 with wavevectors \vec{k}_1 and \vec{k}_2 give an echo in the direction $2\vec{k}_2 - \vec{k}_1$. For inhomogeneously broadened transitions the echo is emitted at time $t = t_{12}$. The echo amplitude measured as a function of t_{12} allows determination of the dephasing time T_2 . (c) When three excitation pulses E_1, E_2, E_3 are applied the coherent signal emitted in the direction $\vec{k}_3 + \vec{k}_2 - \vec{k}_1$ allows determination of the dephasing time T_2 and the energy relaxation time T_1 . Figure adapted from [23].

polarisation for an inhomogeneously broadened system is different to that of the one-pulse case decaying now as $\exp(-2t_{12}/T_2)$. The generated signal is measured in the phase matching direction $2\vec{k}_2 - \vec{k}_1$.

The three-pulse photon echo experiment involves the first pulse ($A = \pi/2$) again creating a macroscopic polarisation which immediately begins to decay. In this scheme the second pulse that arrives at a delay time t_{12} is a $\pi/2$ -pulse rather than a π -pulse. This second $\pi/2$ -pulse creates population in either the ground or excited states in which the coherence is *stored* [26]. A third $\pi/2$ -pulse then interacts with the sample at delay time t_{23} and causes the system to rephase the inhomogeneous component of the polarisation decay to produce a photon echo at time $t = t_{12}$, where time zero corresponds to the arrival of the last (third) pulse (Fig. 1.4(c)). The signal is measured in the phase matching direction $\vec{k}_3 + \vec{k}_2 - \vec{k}_1$ and is maximum for three $\pi/2$ -pulses.

The temporal dependence of the time-integrated intensity of $P^{(3)}(t_{23}, t_{12}, t)$ now provides a probe of the population relaxation T_1 by varying t_{23} , where t_{23} is called the *population* time, and the homogeneous dephasing dynamics by varying t_{12} , where t_{12} is called the *coherence* time. It can be seen when pulses 2 and 3 are coincident ($t_{23} = 0$, Fig. 1.4) the three-pulse experiment reduces to the two-pulse measurement. The decay of the third-order polarisation as a function of t_{12} has the same relationship as found in the two-pulse case, $\exp(-2t_{12}/T_2)$. The time-integrated intensity of $P^{(3)}(t_{23}, t_{12}, t)$ as a function of t_{23} for a closed two-level system decays as $\exp(-2t_{23}/T_1)$. Thus, it is possible with the three pulse photon echo experiment to determine the pure dephasing time, T_2^* , using Eq. 1.5.

There are two major forms of the three-pulse photon echo experiment: (i) three-pulse photon echo peak shift and (ii) transient grating. Three-

pulse photon echo peak shift involves scanning the coherence time t_{12} and measuring the time, Δt_{12}^* (peak shift), at which the intensity peaks for fixed values of the population time t_{23} . Transient grating is a special case of the photon echo experiment where the first two pulses are coincident in time $t_{12} = 0$ and only the population time t_{23} is scanned. Both methods are capable of estimating the slow part of the time-dependent correlation function $M(t)$ that describes the various line broadening (optical dephasing) processes and intramolecular vibrational (nuclear) motion [8, 21, 22]. The advantage of the photon echo peak shift is its ability to estimate the amount of *static* inhomogeneous broadening [21, 22].

In both the photon echo peak shift and the transient grating experiments the signal is measured as the integrated (time and spectrum) intensity. An extension of these techniques involves spectrally resolving the emitted signal using a spectrometer. The measured spectrum can be related to the macroscopic polarisation $P^{(3)}(t_{23}, t_{12}, t)$ through Fourier transformation around time t [27–36]. Measuring the signal spectrum provides another useful experimental degree of freedom that can be used to further separate the various processes (optical dephasing, vibrational and population relaxation) contributing to the decay of the macroscopic polarisation $P^{(3)}(t_{23}, t_{12}, t)$.

This thesis investigates the signal dependence of spectrally resolved transient grating and photon echo spectroscopy. This includes investigation of the relationship between the spectral width and position of the signal spectrum and the time-dependent correlation function $M(t)$. The signal response of the spectrally resolved signal when the technique is extended to include two-colour excitation. Two-colour excitation denotes the case when the wavelength of the first two laser pulses is different to the wavelength of the third, i.e., $\lambda_{1,2} \neq \lambda_3$. Two-colour excitation has previously been applied

to photon echo peak shift and transient grating [37–41]; however it will be shown that the spectrally resolved measurement provides additional information on the dynamics and structure of the underlying quantum system within this regime. The development and implementation of the spectrally resolved measurement of the photon echo signal using single and two different wavelength(s) (one- and two-colour) for the applied pulses in the visible region to study biological molecules is the primary aim of this thesis.

1.4 Thesis Outline

This thesis describes the development of the spectrally resolved two-colour three-pulse photon echo technique in the visible region for application to complex molecular systems in solution.

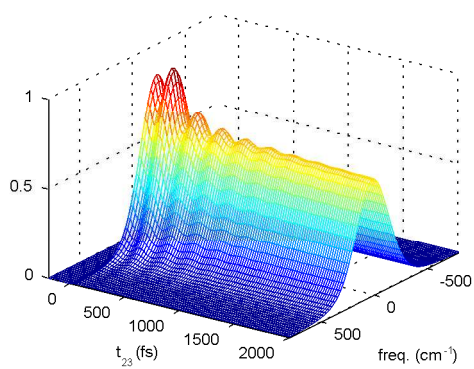
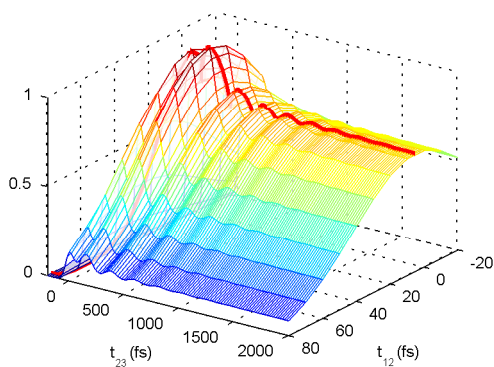
Chapter 2 introduces the theoretical framework for describing the signal response based on the previously developed linear response formalism and the Multimode Brownian Oscillator model [17–19]. Theoretical calculations are then employed to show the relationship between the spectral width and position of the spectrally resolved measurement and the time-dependent correlation function $M(t)$ which describes the solute/solvent system. Chapter 3 describes the femtosecond laser system and the optical arrangement used to perform the photon echo experiments as well as data processing.

In Chapter 4 the spectrally resolved one- and two-colour experimental technique is applied to the laser dye rhodamine 101, where the effect of rapid intraband vibrational relaxation on the measured transient grating spectrum as well as the solvation dynamics using one-colour excitation are investigated. This is followed by two-colour experiments to study the transient effects on the initially created wavepacket as it moves from the spectral window defined by the first two laser pulses into that of the third pulse.

Chapter 5 investigates the initial events involved in the photolytic dissociation of the carbonyl complex of the heme protein myoglobin. Here photon echo peak shift, spectrally resolved photon echo and two-colour spectrally resolved transient grating are used to investigate the ultrafast dynamics of a chemical reaction. Finally, the thesis finishes with a summary and proposal for future work in Chapter 6.

Chapter 2

Theoretical Background



2.1 Introduction

In Chapter 1 it was discussed how multidimensional photon echo spectroscopy provides a means for distinguishing between homogeneous broadening, inhomogeneous broadening, vibrational and population dynamics for systems in solution. Relationships between the variable time delays and the dephasing and population dynamics were introduced. However, for real systems the measured signals are often more complex than the Bloch picture, having higher vibrational density of states and multiple time scales for dephasing and population dynamics. Thus, it is often necessary to perform theoretical calculations to model the measured signals in order to separate the relative magnitudes and time scales for the various intra- and inter-molecular dynamics.

As mentioned in Chapter 1, major theoretical advances have accompanied the development of multidimensional nonlinear spectroscopy. One of the most successful theoretical frameworks is the response function formalism when used with the Multimode Brownian Oscillator (MBO) model [17–19]. The treatment employs response function theory within the semiclassical Liouville-Maxwell model. This is used to calculate the optical polarisation, from which the emitted signal can be obtained. The MBO model is used to find analytical solutions to the (non)linear response functions for large systems at finite temperatures.

Figure 2.1 shows the sequence for evaluating the various signals relevant to this investigation. The aim of any modelling is to determine the correlation functions for a system from which all of the (non)linear experimental observables can then be evaluated (Fig. 2.1). The oscillator-bath correlation functions $M(t)$ express the ensemble-averaged molecular energy level fluctuations (solvent-correlation function) which relate the solution dynam-

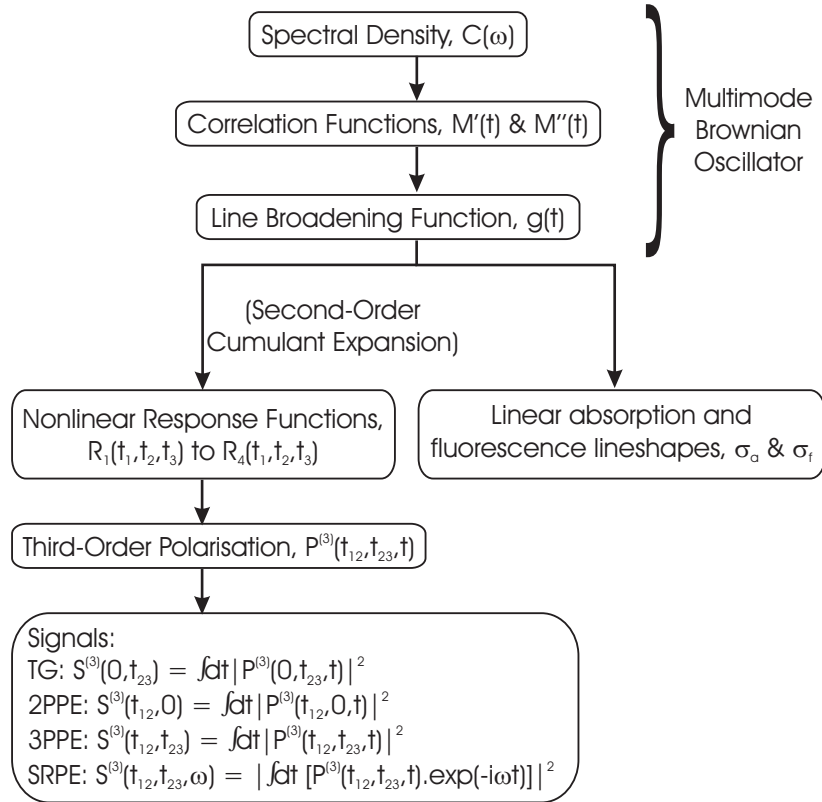


Figure 2.1: Flow chart showing the theoretical framework of the response function formalism and the Multimode Brownian Oscillator model, which relates (non)linear experimental results to the correlation function $M(t)$, where $M'(t)$ $M''(t)$ are the real and imaginary parts, respectively. Here TG = transient grating, 2PPE = Two-Pulse Photon Echo, 3PPE = Three-Pulse Photon Echo and SRPE = Spectrally Resolved Photon Echo.

ics (dephasing) to the quantum molecular system. Thus, a complete set of correlation functions would separately contain all the information regarding inhomogeneous broadening, homogeneous broadening and vibrational dynamics for any given system.

Using the theoretical framework introduced in this Chapter calculations were performed to investigate the relationship between the spectrally resolved measurement of the photon echo and the correlation function $M(t)$. It has been shown analytically by de Boeij *et al.* [21] and Cho *et al.* [22], using the MBO model, that a direct relationship exists between the photon echo peak shift and the slow part of the correlation function $M(t)$. A similar relationship between the transient grating or the transient absorption intensity and the correlation function $M(t)$ has also been shown using model calculations by Joo *et al.* [8]. It is shown using model calculations that the inverse linewidth of the spectrally resolved signal measured as a function of the population time t_{23} can also be used to determine the slow part of the correlation function $M(t)$.

This Chapter contains an outline of the theoretical model beginning with the response function formalism as a method of obtaining the third-order polarisation, followed by the second-order cumulant expansion and the MBO method of evaluating these response functions. The theory is then applied to experimental systems by representing the measured signal as a function of the third-order polarisation. This Chapter closes with a comparison of the (fully integrated) stimulated photon echo and the spectrally resolved stimulated photon echo methods by performing theoretical calculations of both signals for a model system and discussing the characteristics of each.

2.2 Theoretical Model

2.2.1 Response Function Formalism

The theoretical framework introduced in this section is based on the work of Mukamel and coworkers [19] and is included here for completeness. Adopting the semiclassical Maxwell-Liouville equations of motion the transverse radiation field $E(\mathbf{r}, t)$ is treated classically and the solute/solvent system quantum mechanically. Assuming the dipole approximation for the field-sample interaction, gives the interaction Hamiltonian

$$H_{int}(t) = -E(\mathbf{r}, t) \cdot \mathbf{V}, \quad (2.1)$$

where \mathbf{V} is the dipole operator. The position- and time-dependent polarisation $P(\mathbf{r}, t)$ is given by the expectation value of the dipole operator \mathbf{V} :

$$P(\mathbf{r}, t) = Tr[\mathbf{V}\rho(t)], \quad (2.2)$$

where $\rho(t)$ is the time-dependent density matrix operator for the sample. An important assumption is now made that the interaction with the radiation field is sufficiently weak to allow a perturbative, order-by-order, expansion of the density matrix operator and therefore the polarisation induced by the applied field. This gives:

$$\rho(t) = \rho^{(0)}(t) + \rho^{(1)}(t) + \rho^{(2)}(t) + \rho^{(3)}(t) + \dots \quad (2.3)$$

and

$$P(\mathbf{r}, t) = P^{(0)}(\mathbf{r}, t) + P^{(1)}(\mathbf{r}, t) + P^{(2)}(\mathbf{r}, t) + P^{(3)}(\mathbf{r}, t) + \dots \quad (2.4)$$

where

$$P^{(n)}(\mathbf{r}, t) \equiv Tr[\mathbf{V}\rho^{(n)}(t)]. \quad (2.5)$$

Here $P^{(n)}(\mathbf{r}, t)$ denotes the polarisation to n th order in the applied field. It is assumed that the polarisation vanishes in the absence of the applied field so that $P^{(0)} = 0$. Note that $P^{(n)}(\mathbf{r}, t)$ contains products of $n + 1$ dipole operator factors \mathbf{V} . Finally, if a perturbative expansion of the density matrix operator $\rho(t)$ (Eq. 2.3) is performed and substituted into Eq. 2.4 then the n th order polarisation becomes:

$$P^{(n)}(\mathbf{r}, t) \propto \int_0^\infty dt_n \int_0^\infty dt_{n-1} \cdots \int_0^\infty dt_1 S^{(n)}(t_n, t_{n-1}, \dots, t_1) \\ E(\mathbf{r}, t - t_n)E(\mathbf{r}, t - t_n - t_{n-1}) \cdots E(\mathbf{r}, t - t_n - t_{n-1} \cdots - t_1), \quad (2.6)$$

where for the case when all commutators act to the right

$$S^{(n)}(t_n, t_{n-1}, \dots, t_1) = \left(\frac{i}{\hbar}\right)^n \theta(t_1)\theta(t_2) \cdots \theta(t_n) \\ \times \langle \mathbf{V}(t_n + \cdots + t_1)[\mathbf{V}(t_{n-1} + \cdots + t_1), [\cdots [\mathbf{V}(t_1), [\mathbf{V}(0), \rho(-\infty)]] \cdots]] \rangle \quad (2.7a)$$

or when they act to the left

$$S^{(n)}(t_n, t_{n-1}, \dots, t_1) = \left(\frac{i}{\hbar}\right)^n \theta(t_1)\theta(t_2) \cdots \theta(t_n) \\ \times \langle [[[\cdots [\mathbf{V}(t_n + \cdots + t_1), \mathbf{V}(t_{n-1} + \cdots + t_1)] \cdots], \mathbf{V}(t_1)], \mathbf{V}(0)]\rho(-\infty) \rangle, \quad (2.7b)$$

where $\theta(t_1)$ to $\theta(t_n)$ is the Heaviside step function. The n th-order *response function*, $S^{(n)}(t)$, carries all the information necessary for the calculation of optical measurements. Here Mukamel's notation is followed [19], where

$t_1 \cdots t_n$ are the time intervals between successive time-ordered field-sample interactions, t_1 is the earliest time interval and t_n is the last. It is noted that the polarisation at any given time can depend only on the applied field at earlier times such that:

$$S^{(n)}(t_n, t_{n-1}, \dots, t_1) = 0 \text{ if } t_n < 0. \quad (2.8)$$

This is ensured by the Heaviside step function [$\theta(t_n) = 1$ for $t_n > 0$ and $\theta(t_n) = 0$ for $t_n < 0$] that appears in the expressions for $S^{(n)}$ (Eqs. 2.7a and 2.7b).

In order to adequately interpret the experimental techniques to be introduced, for an isotropic medium and relatively weak applied fields only the first- and third-order polarisation need to be considered. The first- and third-order response functions are represented as the so-called *Liouville space pathways*. In Liouville space all ordinary Hilbert space operators are treated as vectors and the bras and kets as pairs. Each component of the vector represents the dynamics of a pair and the time evolution of the density operator is then given by acting from the left. Thus, after all the commutators have been evaluated, the linear response function can be recast as:

$$S^{(1)}(t_1) = \frac{i}{\hbar} \theta(t_1) [J(t_1) - J^*(t_1)] \quad (2.9)$$

where

$$\begin{aligned} J(t_1) &= \langle \mathbf{V}(t_1) \mathbf{V}(0) \rho(-\infty) \rangle, \\ J^*(t_1) &= \langle \mathbf{V}(0) \mathbf{V}(t_1) \rho(-\infty) \rangle. \end{aligned} \quad (2.10)$$

The two terms in Eq. 2.9 represent the two Liouville space pathways that contribute to the linear response. Since the n th order response functions

contain $n + 1$ dipole interactions such that the dipole operators (V 's) can act from the right or left (as in Eqs. 2.7a and 2.7b) the third-order response function has $2^n = 8$ terms:

$$S^{(3)}(t_3, t_2, t_1) = \left(\frac{i}{\hbar}\right)^3 \theta(t_1)\theta(t_2)\theta(t_3) \sum_{\alpha=1}^4 [R_\alpha(t_3, t_2, t_1) - R_\alpha^*(t_3, t_2, t_1)], \quad (2.11)$$

where

$$R_1(t_3, t_2, t_1) = \langle \mathbf{V}(t_1)\mathbf{V}(t_1 + t_2)\mathbf{V}(t_1 + t_2 + t_3)\mathbf{V}(0)\rho(-\infty) \rangle, \quad (2.12a)$$

$$R_2(t_3, t_2, t_1) = \langle \mathbf{V}(0)\mathbf{V}(t_1 + t_2)\mathbf{V}(t_1 + t_2 + t_3)\mathbf{V}(t_1)\rho(-\infty) \rangle, \quad (2.12b)$$

$$R_3(t_3, t_2, t_1) = \langle \mathbf{V}(0)\mathbf{V}(t_1)\mathbf{V}(t_1 + t_2 + t_3)\mathbf{V}(t_1 + t_2)\rho(-\infty) \rangle, \quad (2.12c)$$

$$R_4(t_3, t_2, t_1) = \langle \mathbf{V}(t_1 + t_2 + t_3)\mathbf{V}(t_1 + t_2)\mathbf{V}(t_1)\mathbf{V}(0)\rho(-\infty) \rangle. \quad (2.12d)$$

An exact solution exists for the response functions outlined above for the case in which a two-level system is coupled to *harmonically* vibrating nuclear degrees of freedom. Moreover, if only a few selected and relevant degrees of freedom are explicitly followed, while treating the remaining degrees of freedom as a thermal bath described using quantum statistical mechanics, it is possible to consider large systems at finite temperatures, i.e., a *reduced description*. One method to obtain an analytical solution of the response functions for a reduced description system is to use the MBO model [19] which involves using a cumulant expansion truncated at the second order.

Before continuing, however, it is important to note that the response functions were calculated for a simple model of an isolated small particle in real space as a function of position \mathbf{r} . In order to consider a system of arbitrary size it is important to include explicit vector notation for the radiation field and the polarisation and recast the polarisation expression

through Fourier relations into momentum (\vec{k}) space to provide a macroscopic picture. The derivations are not included here but can be found in Reference [19] on pages 123-127; however, there are several important outcomes. (i) The expression for the radiation fields become a mixed time and frequency representation. This allows the fields to be approximated as a slowly varying envelope where the time-dependent component $E(t)$ varies on a much slower timescale than the optical periods ω^{-1} . (ii) The number of permutations in the calculation of the polarisation can be significantly reduced once a particular \vec{k}_s is selected, i.e., $\vec{k}_s = \vec{k}_3 + \vec{k}_2 - \vec{k}_1$ for the third-order measurements considered in this thesis. The reason this simplification can be made is that each change in sign of $\vec{k}_j \rightarrow -\vec{k}_j$ is also accompanied by reversing the sign of the corresponding frequency $\omega_j \rightarrow -\omega_j$ and consequently some the Liouville space pathways contain highly oscillatory terms where the molecular and radiation field frequencies add, whereas in other contributions these frequencies subtract. The former terms make a very small contribution and may be neglected. This approximation is known as the rotating wave approximation and greatly simplifies calculations. (iii) For the sake of clarity the tensor notation is hereafter dropped.

2.2.2 Multimode Brownian Oscillator and Cumulant Expansion

The Multimode Brownian Oscillator method of calculating the response functions is based on a model containing two electronic states, a ground state $|g\rangle$ and an electronically excited state $|e\rangle$, linearly coupled to harmonically vibrating nuclear degrees of freedom, denoted by \mathbf{q} . Specifically, \mathbf{q} can represent discrete intra-molecular modes $\mathbf{q}_{\text{intra}}$, as well as motions of the thermal bath \mathbf{q}_{bath} which are treated as a continuum (Fig. 2.2(a)). Figure

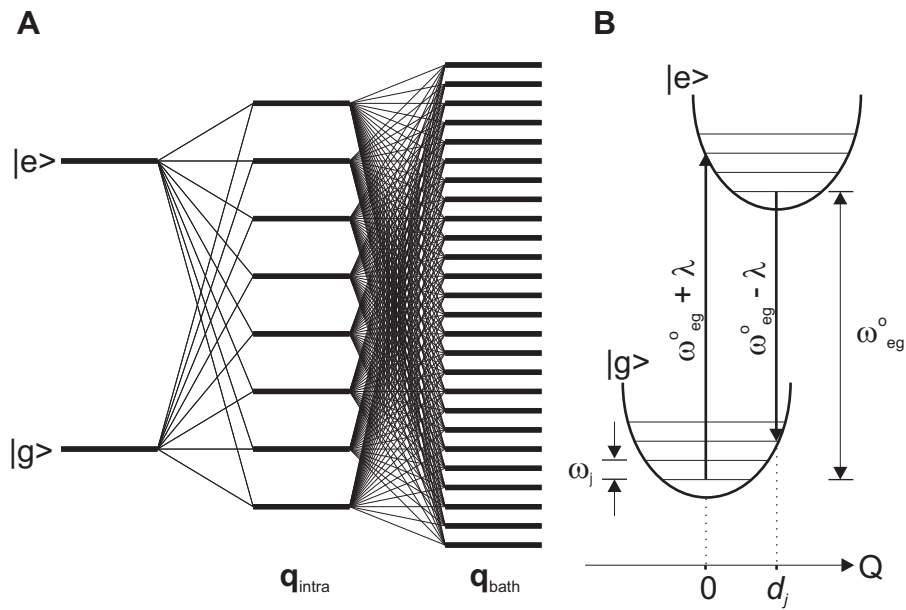


Figure 2.2: (a) Graphic representation of the MBO model beginning with a two-level system linearly coupled to several intra-molecular modes ($\mathbf{q}_{\text{intra}}$) which in turn are linearly coupled to a thermal bath (\mathbf{q}_{bath}). (b) Displaced Harmonic Oscillator where the excited state $|e\rangle$ is displaced along the nuclear coordinate Q by d_j for a single vibrational mode of frequency ω_j . $\omega_{eg}^o + \lambda$ and $\omega_{eg}^o - \lambda$ represent the first moment of the absorption and fluorescence maximum, respectively, where 2λ is the Stokes shift.

2.2(b) shows the Franck-Condon representation for a two-level system where the excited state is displaced along the nuclear coordinate Q by d_j . The 0-0 electronic transition frequency is denoted by ω_{eg}^o and the total reorganisation energy $\lambda = \sum_j \lambda_j$ is the magnitude of the system-bath fluctuations and is related to the displacement d_j by:

$$\lambda = \sum_j \lambda_j = \sum_j \frac{m_j \omega_j^2 d_j^2}{2}, \quad (2.13)$$

where m_j and ω_j are the reduced mass and frequency for the j -th mode, respectively.

In the MBO model the time-dependent correlation function $M_j(t)$ describes dephasing (e.g., due to (in)homogeneous broadening) through the fluctuations of the transition frequency of the j -th mode. A line broadening function $g_j(t)$ for the j -th mode can be evaluated from $M_j(t)$ thus:

$$g_j(t) = \Delta_j^2 \int_0^t d\tau_1 \int_0^{\tau_1} d\tau_2 M_j'(\tau_2) - i\lambda_j \int_0^t d\tau [1 - M_j''(\tau)], \quad (2.14)$$

where Δ_j is the electron-vibration coupling strength for the j -th Brownian oscillator and $M_j'(t)$, $M_j''(t)$ are the real and imaginary parts of $M_j(t)$, respectively. In the high temperature limit ($k_B T \gg \hbar\omega_j$), Δ_j^2 and λ_j are related by $\Delta_j^2 = 2k_B T \lambda_j / \hbar$ [8]. For a typical multimode system $g(t) = \sum_j g_j(t)$. As stated in the Introduction the steady-state absorption and fluorescence spectra can be calculated from the line broadening function $g(t)$:

$$\sigma_a(\omega) = \frac{1}{\pi} \text{Re} \int_0^\infty dt \exp[i(\omega - \omega_{eg})t] \exp[-g(t)], \quad (2.15)$$

$$\sigma_f(\omega) = \frac{1}{\pi} \text{Re} \int_0^\infty dt \exp[i(\omega - \omega_{eg} + 2\lambda)t] \exp[-g^*(t)], \quad (2.16)$$

where $\omega_{eg} = \omega_{eg}^o - \lambda$ is the first moment of absorption and $g^*(t)$ is the

complex conjugate of $g(t)$. Once $g(t)$ is given, the response functions R_1 through to R_4 (Eqs. 2.12) can be calculated perturbatively assuming the Condon approximation and using a second-order cumulant expansion [19]:

$$\begin{aligned}
R_1(t_3, t_2, t_1) &= \exp(-i\omega_{eg}t_1 - i\omega_{eg}t_3) \\
&\times \exp \left[-g^*(t_3) - g(t_1) - g^*(t_2) \right. \\
&\quad \left. + g^*(t_2 + t_3) + g(t_1 + t_2) - g(t_1 + t_2 + t_3) \right], \quad (2.17a)
\end{aligned}$$

$$\begin{aligned}
R_2(t_3, t_2, t_1) &= \exp(i\omega_{eg}t_1 - i\omega_{eg}t_3) \\
&\times \exp \left[-g^*(t_3) - g^*(t_1) + g(t_2) \right. \\
&\quad \left. - g(t_2 + t_3) - g^*(t_1 + t_2) + g^*(t_1 + t_2 + t_3) \right], \quad (2.17b)
\end{aligned}$$

$$\begin{aligned}
R_3(t_3, t_2, t_1) &= \exp(i\omega_{eg}t_1 - i\omega_{eg}t_3) \\
&\times \exp \left[-g(t_3) - g^*(t_1) + g^*(t_2) \right. \\
&\quad \left. - g^*(t_2 + t_3) - g^*(t_1 + t_2) + g^*(t_1 + t_2 + t_3) \right], \quad (2.17c)
\end{aligned}$$

$$\begin{aligned}
R_4(t_3, t_2, t_1) &= \exp(-i\omega_{eg}t_1 - i\omega_{eg}t_3) \\
&\times \exp \left[-g(t_3) - g(t_1) - g(t_2) \right. \\
&\quad \left. + g(t_2 + t_3) + g(t_1 + t_2) - g(t_1 + t_2 + t_3) \right]. \quad (2.17d)
\end{aligned}$$

The second-order cumulant expansion provides an exact solution for this harmonic model. Using Eqs. 2.6 and 2.11 and substituting the four response functions Eqs. 2.17(a-d) an expression can be obtained for the full third-order polarisation (Eq. 2.25 below). However, the form of the correlation function $M(t)$ for various limiting cases of the MBO model need to be considered.

2.2.3 Limiting Cases of $M(t)$: Discrete and Continuous Modes

High frequency underdamped modes

First, for a weakly damped mode ($\gamma_j < 2\omega_j$) the real and imaginary parts of the correlation function become indistinguishable [19, 21] and

$$M(t) \equiv M'(t) \equiv M''(t) = \exp\left(-\frac{\gamma_j t}{2}\right) \left[\cos \omega_j t + \frac{\gamma_j}{2\omega_j} \sin \omega_j t \right] \quad (2.18)$$

and the line broadening function:

$$g(t) = g'(t) + g''(t), \quad (2.19a)$$

$$g'(t) = \frac{2\Delta_j^2}{\omega_j(\gamma_j^2 + 4\omega_j^2)^2} \times \left[2\omega_j (-3\gamma_j^2 + \gamma_j^3 t + 4\omega_j^2 + 4\gamma_j \omega_j^2 t) + \exp\left(-\frac{\gamma_j t}{2}\right) \times (6\gamma_j^2 \omega_j - 8\omega_j^3) \times \cos(\omega_j t) + \exp\left(-\frac{\gamma_j t}{2}\right) \times \gamma_j (\gamma_j^2 - 12\omega_j^2) \times \sin(\omega_j t) \right], \quad (2.19b)$$

$$g''(t) = \frac{-i\lambda_j}{\omega_j(\gamma_j^2 + 4\omega_j^2)} \times \left[(-4\gamma_j \omega_j + \gamma_j^2 \omega_j t + 4\omega_j^3 t) + \exp\left(-\frac{\gamma_j t}{2}\right) \times (4\gamma_j \omega_j) \times \cos(\omega_j t) + \exp\left(-\frac{\gamma_j t}{2}\right) \times (\gamma_j^2 - 4\omega_j^2) \times \sin(\omega_j t) \right], \quad (2.19c)$$

where

$$\lambda_j = \frac{\Delta_j^2}{\omega_j} \tanh\left(\frac{\hbar\omega_j}{2k_B T}\right). \quad (2.20)$$

If the high temperature limit $k_B T \gg \hbar\gamma_j$ holds, then

$$\lambda_j = \frac{\Delta_j^2 \hbar}{2k_B T}. \quad (2.21)$$

Underdamped modes are usually employed to model intra-molecular vibrational modes.

Strongly Overdamped Modes

Another useful example is the case of a strongly overdamped mode ($\gamma_j \gg \omega_j$) within the high temperature limit $k_B T \gg \hbar \Lambda_j$, where $\Lambda_j = \omega_j^2 / \gamma_j$ is the inverse correlation time of the system-bath fluctuations. The correlation functions then become

$$M'(t) = M''(t) = \exp(-\Lambda_j t) \quad (2.22)$$

and the line broadening function:

$$g(t) = \frac{\Delta_j^2}{\Lambda_j^2} [\exp(-\Lambda_j t) + \Lambda_j t - 1] - i(\lambda_j / \Lambda_j) [\exp(-\Lambda_j t) + \Lambda_j t - 1]. \quad (2.23)$$

A strongly overdamped mode is often used to characterise solvation. As discussed in the Introduction, solvation is characterised by two processes: homogeneous broadening and inhomogeneous broadening. It is common for these two processes to be separated based on the associated time scales, usually *short* in the case of homogeneous broadening and *long* for inhomogeneous broadening. It has been shown [19] that Eq. 2.23 approximates a Lorentzian lineshape in the limit when the nuclear dynamics (Λ_j^{-1}) are fast compared with the vibronic coupling strength (Δ_j) and is used to model homogeneous broadening. In the opposite limit when the nuclear dynamics are slow compared with the coupling strength Eq. 2.23 approximates a Gaussian lineshape and is used to model inhomogeneous broadening.

In another approach, the ultrafast (< 200 fs) component of solvation dynamics has been found to be purely Gaussian in nature and results from free (small amplitude) motions of solvent molecules. In this case the correlation functions take the form [8]:

$$M'(t) = M''(t) = \exp\left(-\frac{\omega_0^2 t^2}{2}\right). \quad (2.24)$$

Note it has been shown that there is no apparent difference between using Eqs. 2.23 and 2.24 in calculations of the full third-order polarisation [8].

Continued Overleaf

2.3 Physical Significance of Response Functions and Feynman Diagrams

For a two-level system with an infinite excited state lifetime and applying the rotating wave approximation the third-order polarisation in the phase matching direction $\vec{k}_s = -\vec{k}_1 + \vec{k}_2 + \vec{k}_3$ is given by [19]:

$$\begin{aligned}
P^{(3)}(t, t_{12}, t_{23}) = & \\
& \left(\frac{i}{\hbar}\right)^3 \int_0^\infty dt_3 \int_0^\infty dt_2 \int_0^\infty dt_1 \left\{ [R_2(t_3, t_2, t_1) + R_3(t_3, t_2, t_1)] \right. \\
& \times E_3(t - t_3) E_2(t + t_{23} - t_3 - t_2) E_1^*(t + t_{12} + t_{23} - t_3 - t_2 - t_1) \\
& \times \exp[i(\omega_3 + \omega_2 - \omega_1)t_3 + i(\omega_2 - \omega_1)t_2 - i\omega_1 t_1] \\
& + [R_1(t_3, t_2, t_1) + R_4(t_3, t_2, t_1)] \\
& \times E_3(t - t_3) E_2(t + t_{23} - t_3 - t_2 - t_1) E_1^*(t + t_{12} + t_{23} - t_3 - t_2) \\
& \times \exp[i(\omega_3 + \omega_2 - \omega_1)t_3 + i(\omega_2 - \omega_1)t_2 + i\omega_2 t_1] \left. \right\} \\
& + \left\{ [R_2(t_3, t_2, t_1) + R_3(t_3, t_2, t_1)] \right. \\
& \times E_3(t - t_3 - t_2) E_2(t + t_{23} - t_3) E_1^*(t + t_{12} + t_{23} - t_3 - t_2 - t_1) \\
& \times \exp[i(\omega_3 + \omega_2 - \omega_1)t_3 + i(\omega_2 - \omega_1)t_2 - i\omega_1 t_1] \\
& + [R_1(t_3, t_2, t_1) + R_4(t_3, t_2, t_1)] \\
& \times E_3(t - t_3 - t_2 - t_1) E_2(t + t_{23} - t_3) E_1^*(t + t_{12} + t_{23} - t_3 - t_2) \\
& \times \exp[i(\omega_3 + \omega_2 - \omega_1)t_3 + i(\omega_2 - \omega_1)t_2 + i\omega_2 t_1] \left. \right\}. \tag{2.25}
\end{aligned}$$

Here $\omega_n (n = 1, 2, 3)$ are the carrier frequencies of the applied fields E_1 to E_3 and t is the time with respect to the third pulse (Fig. 2.3(a)). The response functions R_2 and R_3 (Fig. 2.3(b)) describe the real photon echo in an inhomogeneously broadened system, which for complete rephasing

peaks at $t = t_{12}$. R_1 and R_4 (Fig. 2.3(b)) describe the virtual echo (free-induction decay, FID) which peaks at $t = 0$ regardless of the nature of the line broadening mechanism. Furthermore R_1 and R_2 describe the system when it evolves in the excited state during the population period, and R_3 and R_4 describe the dynamics in the ground state (Fig. 2.3(b)).

The evolution of the third-order polarisation during the three time durations (t_1, t_2, t_3) can be interpreted as either propagation in a coherence state, in which the system either dephases during t_1 or t_3 or rephases during t_3 , or in a population state during t_2 , with no dephasing or rephasing (Fig. 2.3(b)). The first pulse interaction creates a coherence state, in which the system evolves as a superposition between the ground state and the excited states. If the system evolves with no further interactions with the E -fields, it will completely dephase as a free-induction decay (FID). The second pulse interaction then creates a population state, in which the system evolves either in the ground or excited states. During this period, the system ceases to dephase and instead evolves via the population dynamics associated with the respective electronic states. The third and final pulse interaction creates another coherence state. When this second coherence state is the complex conjugate of the first, e.g., when the second and third pulses are $\pi/2$ pulses, the system can rephase and generate a photon echo, e.g., R_2 and R_3 . By contrast, when the system evolves in the same manner as the first coherence period, it continues to dephase, leading to a FID or virtual echo. The rephasing capability of the system is stored in the population state by the coupling of the coherence and the populations by the nonlinear laser-molecule interaction and may be subsequently destroyed by dephasing processes, e.g., solvation. When the population period is long, the system may lose its capacity to rephase during the final interaction, and

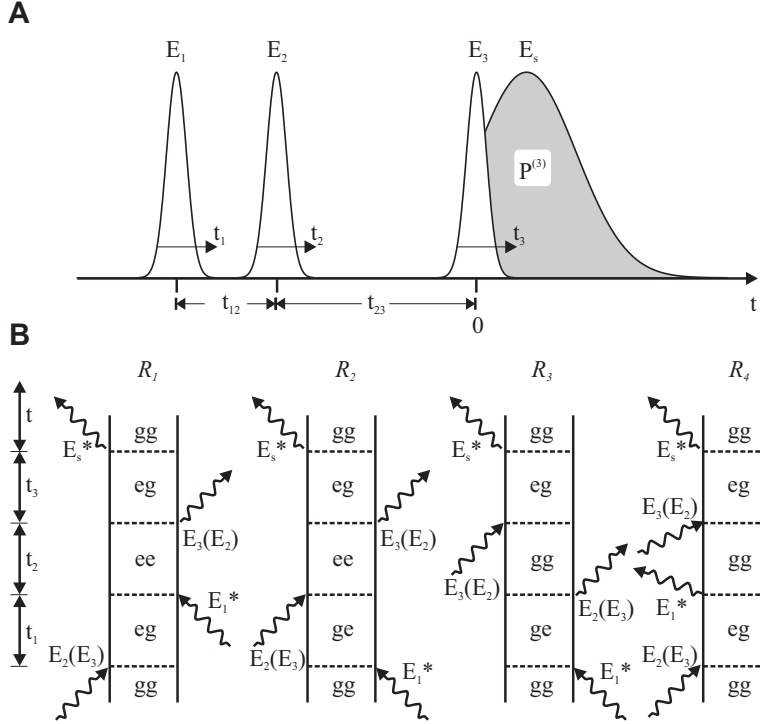


Figure 2.3: (a) Pulse sequence for three-pulse photon echo including relevant delay times t_{12} and t_{23} as indicated. (b) Double-sided Feynman diagrams used for a perturbative description of the third-order polarisation $P^{(3)}$ with wavevector $-\vec{k}_1 + \vec{k}_2 + \vec{k}_3$ of a two-level system with ground state $|g\rangle$ and excited state $|e\rangle$. These diagrams are governed by several rules: (i) The density operator is represented as two vertical lines. The left line represents the ket and the right the bra. (ii) Time runs vertically from bottom to the top. (iii) An interaction with a radiation field is represented as a wavy line and horizontal dashed lines. (iv) Each diagram has an overall sign of $(-1)^n$ where n is the number of interactions from the right (bra). This is because each time an interaction V acts from the right in a commutator it carries a minus sign. (v) Each interaction is assigned an arrow and labelled by the corresponding field E_j . An arrow pointing to the right represents a contribution of $E(t) \exp(-i\omega t + i\vec{k} \cdot \mathbf{r})$ to the polarisation and an arrow pointing to the left represents a $E^*(t) \exp(i\omega t - i\vec{k} \cdot \mathbf{r})$ contribution. (vi) The overall frequency of the term is the sum of the three frequencies ω_1, ω_2 and ω_3 with their appropriate signs. Note **gg** and **ee** represent the populations ρ_{gg} and ρ_{ee} , respectively, while **eg** and **ge** represent the coherences ρ_{eg} and ρ_{ge} , respectively. The electric fields (E) in parenthesis are given for $t_{23} < 0$. Rephasing diagrams R_2 and R_3 describe the real echo, while R_1 and R_4 describe the so-called virtual echo (free-induction decay) signal.

then during the third period the system response again resembles a FID.

2.4 Relationship Between Measured Signals and Third-Order Polarisation

2.4.1 Integrated Signal

The general expression for the stimulated photon echo (SPE) is given by the total integrated signal in the $\vec{k}_s = -\vec{k}_1 + \vec{k}_2 + \vec{k}_3$ direction:

$$S_{\text{SPE}}^{(3)}(t_{12}, t_{23}) = \int_{-\infty}^{\infty} dt |P^{(3)}(t, t_{12}, t_{23})|^2. \quad (2.26)$$

The photon echo peak shift Δt_{12}^* is represented by plotting the time at which the intensity peaks along the coherence time axis t_{12} as a function of the population time t_{23} .

2.4.2 Spectrally Resolved Signal

A method for obtaining detailed information about the time evolution of the third-order polarisation is to measure the spectral profile of the SPE signal. The third-order polarisation in the frequency domain can be expressed as the Fourier transformation [20] of Eq. 2.25. The spectrally resolved signal is then given by:

$$S_{\text{SPE}}^{(3)}(\omega, t_{12}, t_{23}) = \left| \int_{-\infty}^{\infty} dt P^{(3)}(t, t_{12}, t_{23}) \exp(i\omega t) \right|^2. \quad (2.27)$$

2.4.3 Special Cases

Two special cases of the photon echo are: (i) the *two-pulse* photon echo which is calculated by setting $t_{23} = 0$ and $\omega_2 = \omega_3$, and (ii) the transient

grating signal which is calculated by setting $t_{12} = 0$. These definitions apply to both the integrated ($S_{2\text{PPE}}(t_{12}, 0)$ and $S_{\text{TG}}(0, t_{23})$) and spectrally resolved ($S_{2\text{PPE}}(\omega, t_{12}, 0)$ and $S_{\text{TG}}(\omega, 0, t_{23})$) cases.

2.5 Spectrally Resolved Transient Grating Signals

2.5.1 Relationship to the Correlation Function

To show the correspondence between the correlation function $M(t)$ and the spectrally resolved transient grating (TG) inverse linewidth, denoted as $\Delta f^{-1}(t_{23})_{\text{FWHM}}$, numerical calculation are performed using the MBO model described above. A correlation function of four Brownian oscillators is considered:

$$M(t) = A_1 \exp(-\Lambda_1 t) + A_2 \exp(-\Lambda_2 t) + A_3 + A_\nu \exp\left(-\frac{\gamma_\nu t}{2}\right) \left(\cos(\Omega_\nu t) + \left(\frac{\gamma_\nu}{2\Omega_\nu}\right) \sin(\Omega_\nu t) \right) \quad (2.28)$$

where $\Omega_\nu = [(\omega_\nu)^2 - (\gamma_\nu/2)^2]^{1/2}$. The first three terms represent solvent motion with relative amplitudes A_i and decay times Λ_i^{-1} where $\Lambda_3^{-1} = \infty$, while the fourth term with relative amplitude A_ν represents a single intramolecular vibrational mode of frequency ω_ν with decay time γ_ν^{-1} . The Brownian oscillator parameters used are listed in Table 2.1. It is noted that this function was taken from de Boeij *et al.* [21] for direct comparison to echo peak shift results and to verify the calculated results.

The spectrally resolved transient grating (TG) inverse linewidth $\Delta f_{\text{FWHM}}^{-1}(t_{23})$ was calculated from:

$$\Delta f_{\text{FWHM}}^{-1}(t_{23}) = 0.441 / \left(\sigma_f(t_{23}) 2\sqrt{2 \ln(0.5)} \right), \quad (2.29)$$

where $0.441 = \Delta f \cdot \Delta t$ is the time-bandwidth product for a transform limited Gaussian pulse [42] and $\sigma_f(t_{23})$ is the standard deviation of a fitted Gaussian to the transient grating spectrum for each point along the population time axis t_{23} . The temporal width of the photon echo pulse $\Delta t_{\text{FWHM}}(t_{23})$ was calculated using $\sigma_t(t_{23})2\sqrt{2 \ln 0.5}$ where $\sigma_t(t_{23})$ is the standard deviation of a fitted Gaussian to $S^{(3)}(t, 0, t_{23}) = |P^{(3)}(t, 0, t_{23})|^2$.

Figure 2.4 shows that a significant correspondence exists between the correlation function and the spectrally resolved transient grating inverse linewidth for a laser pulse width Δt_{E_i} of 80 fs FWHM. Moreover, the spectrally resolved transient grating inverse linewidth also corresponds well with the temporal width of the photon echo signal pulse. The correspondence to the correlation function and the temporal width of the photon echo signal constitute two of the principle findings of this thesis. Included for comparison are the photon echo peak shift and transient grating intensity signals.

To quantify the correspondence the transient grating inverse linewidth and photon echo peak shift fitted using the original correlation function $M(t)$ with the additional parameters A_0 , t_0 and $\Delta\tau$ such that $Fit(t) = A_0M(t - t_0) + \Delta\tau$. It is noted that $\Delta\tau$ was fixed and calculated as the second-order laser pulse width (i.e., $\Delta\tau = \Delta t_{E_i}/\sqrt{2}$)¹ which provided a convenient reference taken from an easily measured experimental parameter. The integrated intensity was fitted with a convolution of the above function with a system response function (see section 3.4.3 on page 54). The results for all three analytical fits are given in Table 2.1.

The spectrally resolved transient grating inverse linewidth signal underestimates the amplitudes A_1 and A_2 of the first two oscillators and over-

¹Here the second-order pulse width refers to the resultant pulse width of a second-order process, e.g. the pulse width produced from a second harmonic generation process is $\Delta t_{SHG} = \Delta t_i/\sqrt{2}$.

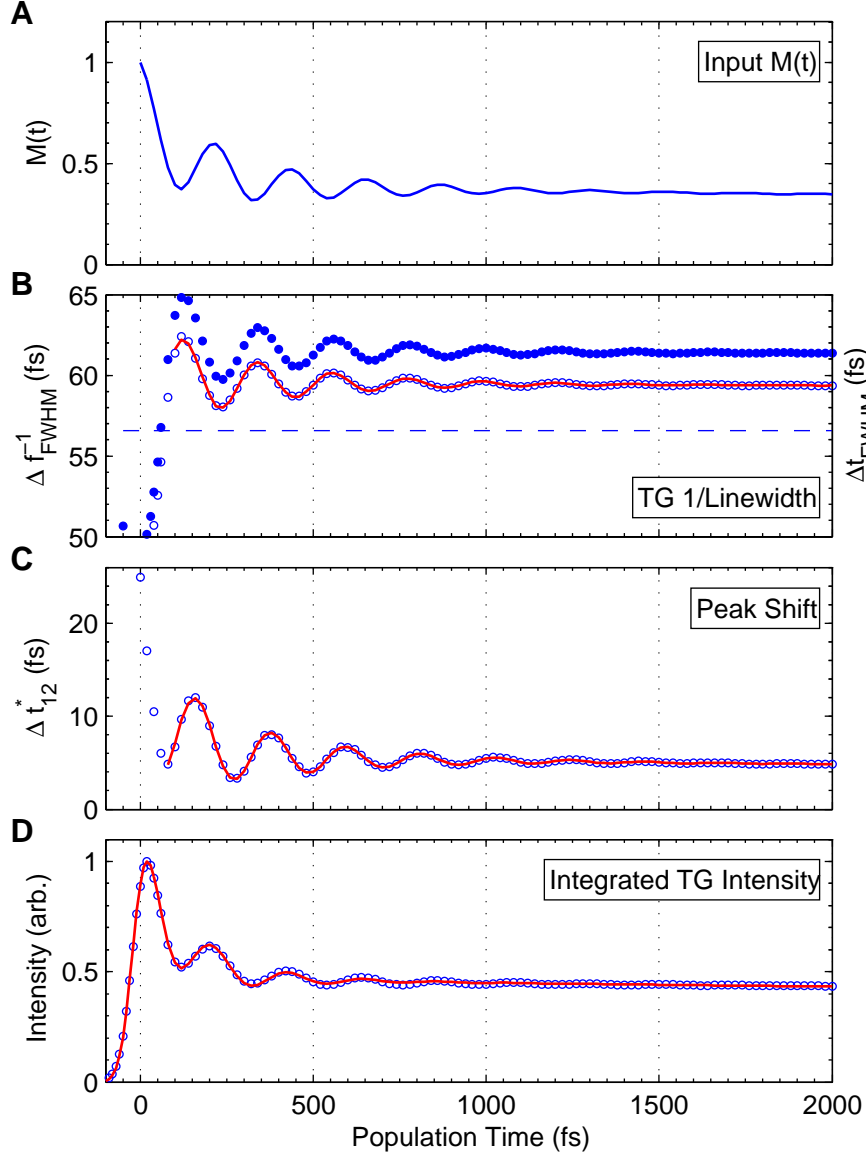


Figure 2.4: (a) A model correlation function $M(t)$ taken from [21]. Calculated (b) TG inverse linewidth $\Delta f^{-1}_{\text{FWHM}}$ (open circles) and photon echo pulse temporal width Δt_{FWHM} (closed circles, offset by +2 fs). (c) Photon echo peak shift. (d) The integrated transient grating intensity. Parameters for the analytical fits (solid lines) are listed in Table 2.1. Calculation details are given in the main text.

Table 2.1: Parameters of the fits presented in Fig. 2.4. The amplitude of the oscillators is normalised so that $\sum_i A_i = 1$ and fits were performed for $t_{23} \geq 80$ fs.

Parameter	Input $M(t)$	Fit to		
		$\Delta f_{\text{FWHM}}^{-1}$ ^a	Δt_{12} ^b	TG Int'y ^c
A_1	0.37	0.15	0.41	0.49
Λ_1^{-1} (fs)	140	143	137	83
A_2	0.13	0.03	0.11	0.07
Λ_2^{-1} (ps)	5.0	5.0	5.0	5.0
A_3	0.26	0.28	0.13	0.19
A_ν	0.24	0.53	0.35	0.25
γ_ν^{-1} (fs)	190	165	170	89
ω_ν (cm ⁻¹)	154	155	154	150
A_0	-	8.6	24	1.0
t_0 (fs)	-	-90	-59	-9
$\Delta\tau$ (fs)	-	56.6	-	-

^a The original $M(t)$ was used as the fitting function with the addition of A_0 , t_0 and $\Delta\tau$ such that: $Fit = A_0M(t - t_0) + \Delta\tau$, where $\Delta\tau = \Delta t_{E_i}/\sqrt{2}$ was fixed.

^b $Fit = A_0M(t - t_0)$

^c Fit is a convolution of $A_0M(t - t_0)$ with the laser pulse. Note the laser pulse width and position were free parameters as they did *not* correspond to $t_{23} = 0$ or the autocorrelation width.

estimates the amplitude A_ν . The photon echo peak shift on the other hand over-estimates the amplitudes A_1 and A_ν while under-estimating the amplitude A_3 of the static oscillator. The decay times Λ_i^{-1} and vibrational mode frequency and decay time ω_ν and γ_ν^{-1} were all well estimated by both the TG inverse linewidth and peak shift techniques. Whilst the quality of the correspondence for the photon echo peak shift signal is better overall than the transient grating inverse linewidth there still remain advantages to spectrally resolving the photon echo signals as discussed in the remaining chapters. It is noted that the TG integrated intensity can also be used to estimate the correlation function. The results of the analytical fit show in this example that the TG intensity under-estimates the decay times (ignoring Λ_2^{-1}) and follows a similar trend to the peak shift results when estimating the amplitudes.

2.5.2 Laser Pulse Width Dependence of Spectrally Resolved Transient Grating Signals

Figure 2.5 shows that an excellent correspondence exists between the spectrally resolved transient grating inverse linewidth $\Delta f^{-1}(t_{23})_{\text{FWHM}}$ and the temporal width of the photon echo signal pulse $\Delta t_{\text{FWHM}}(t_{23})$ calculated using four different laser pulse widths (15, 30, 55 and 80 fs). The parameters of the analytical fits of the original correlation function to the inverse linewidth results for each pulse width are listed in Table 2.2.

The quality of the correspondence between the input correlation function and the inverse linewidth referenced to $\Delta\tau$ diminishes as the laser pulse width is decreased. On the other hand if the amplitude of the slow Brownian oscillator is fixed, i.e., $A_3 = 0.26$, the quality of the correspondence increases as the laser pulse width is decreased. The most significant improvement can

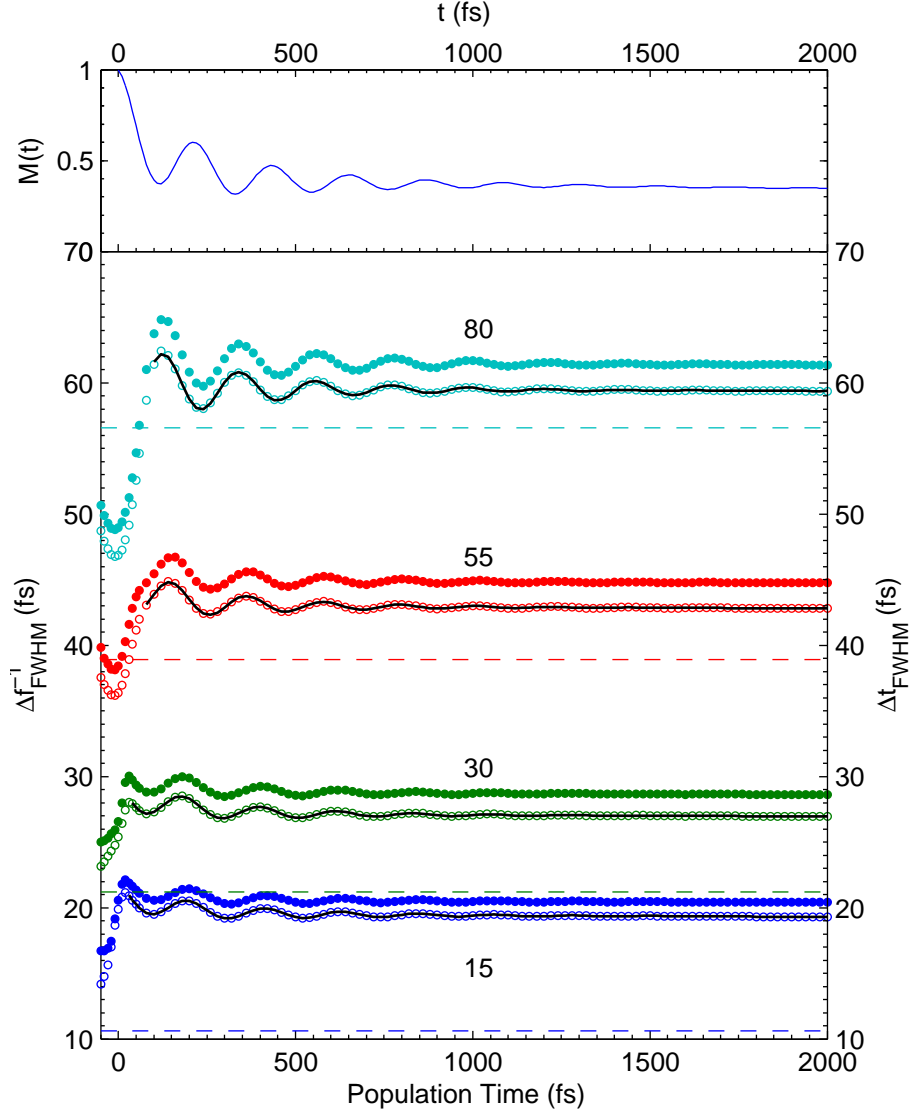


Figure 2.5: Comparison of inverse linewidth $\Delta f^{-1}(t_{23})_{\text{FWHM}}$ (open circles), photon echo signal pulse width $\Delta t_{\text{FWHM}}(t_{23})$ (closed circles, offset by +2 fs) and input correlation function $M(t)$ (top panel) for four different laser pulse widths 15, 30, 55 and 80 fs FWHM. Dashed lines are the second-order pulse widths of the applied pulses $\Delta\tau = \Delta t_{E_i}/\sqrt{2}$. Parameters for analytical fits (solid lines) are listed in Table 2.2. See text for calculation details.

be seen in the amplitudes of the first fast Brownian oscillator A_1 and the vibrational mode A_ν . The improvement of the A_1 estimate is due to the laser pulses being shorter relative to the relaxation time, $\Delta t_{E_i} = 15$ fs compared with $\Lambda_1^{-1} = 140$ fs. Similarly, the improved estimate of A_ν is due to the laser pulses being short relative to the period of the vibrational mode, 15 fs compared with approximately 216 fs. Where the inverse linewidth performs poorly is in estimating the amplitude of the second overdamped oscillator A_2 .

The ability to determine the temporal width of the photon echo signal pulse through the inverse linewidth is a significant result. It is useful to know how the temporal width of the photon echo signal pulse evolves with time. What is not well understood though and which could prove most useful is an understanding of the narrowing around time zero. Note there

Table 2.2: Parameters for analytical fits to the inverse linewidth $\Delta t_{\text{FWHM}}(t_{23})$ for four different laser pulse widths 15, 30, 55 and 80 fs shown in Fig. 2.5. Values in brackets are fit parameters for a fixed amplitude of the slow Brownian oscillator $A_3 = 0.26$

Parameter	Input $M(t)$	Fit ^a to $\Delta f_{\text{FWHM}}^{-1}$ for $\Delta t_{E_i} =$			
		15	30	55	80
A_1	0.37	0.16(0.41)	0.25(0.42)	0.28(0.33)	0.15(0.15)
Λ_1^{-1} (fs)	140	145(146)	141(141)	139(147)	143(154)
A_2	0.13	0.03(0.08)	0.04(0.06)	0.04(0.05)	0.03(0.03)
Λ_2^{-1} (ps)	5.0	5.0(5.0)	5.0(5.0)	5.0(5.0)	5.0(5.0)
A_3	0.26	0.72(0.26)	0.56(0.26)	0.40(0.26)	0.28(0.26)
A_ν	0.24	0.09(0.25)	0.16(0.26)	0.29(0.37)	0.53(0.56)
γ_ν^{-1} (fs)	190	205(205)	176(176)	160(160)	165(165)
ω_ν (cm ⁻¹)	154	154(154)	154(154)	155(154)	155(155)
A_0	-	11.4(3.7)	9.5(4.4)	8.8(5.1)	8.6(5.2)
t_o (fs)	-	-21.3(-21.2)	-35.3(-35.3)	-68.7(-69.2)	-89.8(-89.8)
$\Delta\tau$ (fs)	-	10.6(17.7)	21.2(25.0)	38.9(40.6)	56.6(56.9)

^a The original $M(t)$ was used as the fitting function with the addition of A_0 , t_o and $\Delta\tau$ such that: $Fit = A_0M(t - t_o) + \Delta\tau$.

^b Note $\Delta\tau = \Delta t_{E_i}/\sqrt{2}$ is fixed.

is a small difference between the inverse linewidth and the temporal width of the photon echo signal pulse when a 15 fs laser pulse was used. This is attributed to a Gaussian providing a poor model of the lineshape of the photon echo signal which has a significant exponential decaying component at longer times for shorter laser pulses.

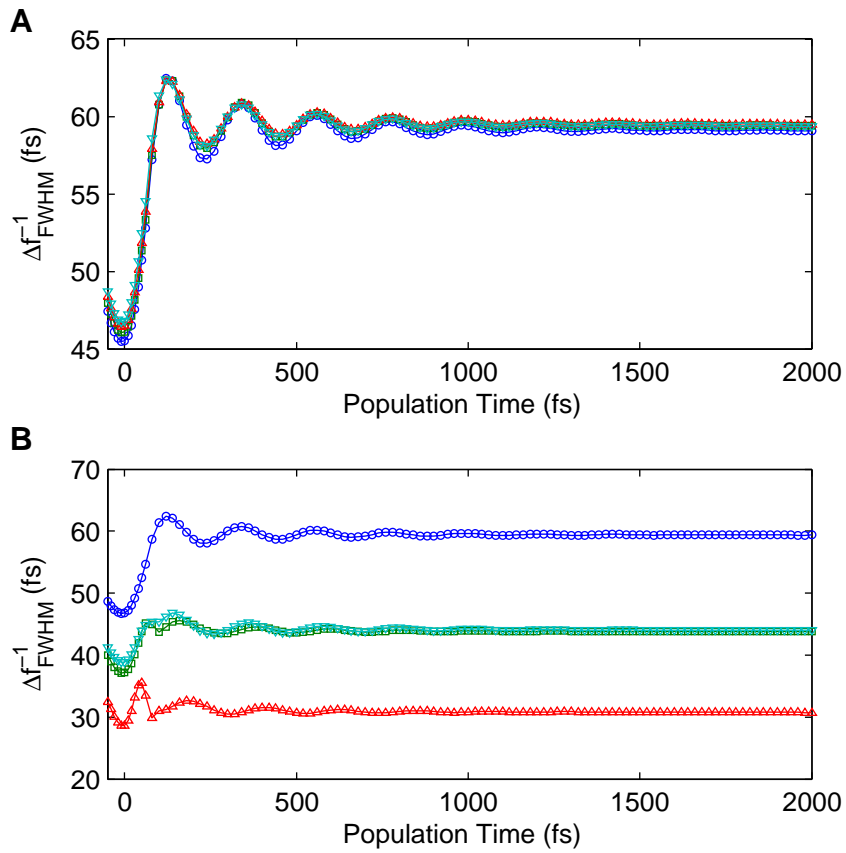


Figure 2.6: Calculated inverse linewidth at (a) four different spectral positions: 216 (circle), 0 (square), -216 (up triangle) and -432 (down triangle) cm^{-1} ; and (b) with linear chirp 0 (circle), +1 (square), +2 (up triangle) and -1 (down triangle). Lines are intended as a guide for the eye.

2.5.3 Inverse Linewidth Laser Wavelength and Linear Chirp Dependence

Figure 2.6 shows that the inverse linewidth is not significantly dependent on the spectral position of the applied laser pulses. The most significant difference is an increase in the amplitude A_ν of the underdamped Brownian oscillator. The addition of linear chirp (i.e., the instantaneous frequency $\omega(t)$ varies linearly in time, see section 3.4 on page 51) has a considerably larger effect on the inverse linewidth (Fig. 2.6). As chirp is added the spectral width of the signal increases and thus the inverse linewidth decreases. The decrease in the inverse linewidth is independent of the sign of the chirp though at short times there are some differences and a phase shift in the intramolecular vibrational mode can be seen for all times. It is noted that pulses with increasing ($B < 0$) and decreasing ($B > 0$) frequency with time are positively and negatively chirped, respectively. Here B refers to the spectral phase parameter used in the electric field expressions in Equation 2.25 (see section 3.4 on page 51).

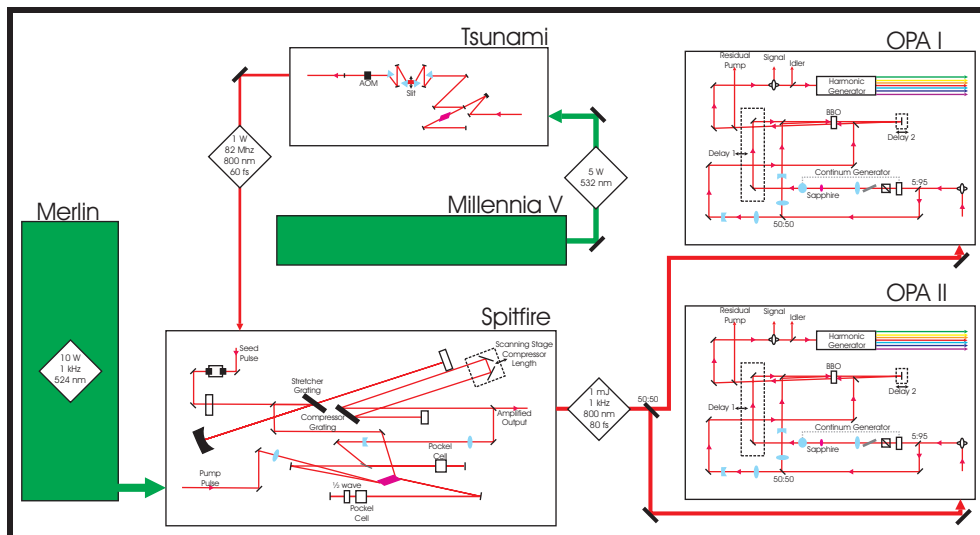
2.6 Summary

In this Chapter a theoretical framework capable of determining the underlying correlation function $M(t)$ for solute/solvent systems having multiple timescales for (in)homogeneous broadening and intramolecular nuclear motions was described. It was shown how this theoretical framework could be extended to calculate spectrally resolved photon echo spectra. It has been shown through numerical calculations using this theoretical framework that a direct relationship exists between the temporal width of the photon echo signal pulse and the inverse linewidth of the spectrally resolved transient

grating signal. Moreover, it was shown that the spectrally resolved transient grating inverse linewidth could be used to estimate the underlying correlation function $M(t)$ albeit with the addition of an arbitrary baseline. The necessity for a baseline prevents this technique from being able to estimate the amount of inhomogeneous broadening, a problem which is overcome by use of photon echo peak shift. There are, however, other advantages to spectrally resolving the photon echo signal. (i) The temporal width of the photon echo signal spectrum can be determined without the addition of another experimental time axis and the technical difficulties associated with mixing a weak signal in a nonlinear crystal. (ii) A reasonable estimate of the correlation function can be obtained by scanning only a single experimental time axis thus saving time and reducing experimental noise. (iii) Here a simple two-level system with an infinite lifetime was considered whereas *real* molecular systems are often more complex. In these cases the additional experimental degree of freedom provided by measuring the signal spectrum can prove invaluable in understanding the underlying photophysical and photochemical processes, e.g., rapid intraband population relaxation (Chapter 4) and multi-electronic level systems with ultrashort excited state lifetimes (Chapter 5).

Chapter 3

Experimental Details



3.1 The Femtosecond Ti:Sapphire Laser System

The laser system for all photon echo and transient grating experiments consisted of a 1 W, 82 MHz mode-locked Ti:sapphire oscillator (Spectra Physics - Tsunami) which produced pulses of 60 fs FWHM Sech^2 and 7.5 nJ that was pumped by a 5W CW, Nd:YVO₄, 532 nm (Spectra Physics - Millennium). These pulses were amplified using a Ti:sapphire regenerative amplifier (Spectra Physics - Spitfire) pumped by a 10 W, 1kHz Q-switched Nd:YLF. The seed pulses from the oscillator were temporally stretched and the amplifier output temporally compressed using a multi-pass grating pair configuration resulting in pulses of 80 fs FWHM Sech^2 and >0.75 mJ. The output of the regenerative amplifier was split and used to pump two independently tunable optical parametric amplifiers (OPAI and OPAL). Each optical parametric amplifier was configured for sum frequency mixing of the residual pump (800 nm) and either the signal (1.10-1.60 μm) or idler (1.60-2.93 μm) which produced visible pulses in the wavelength range 470-620 nm, approximately 90 fs FWHM Gaussian and ≥ 4.9 nm FWHM Gaussian at 550 nm. It is noted the temporal and spectral pulse width of the OPA output is dependent on wavelength and the output pulses were horizontally polarised.

3.2 Experimental Arrangement

The optical arrangement for the photon echo and transient grating experiments is given in Figure 3.1 and involves three beam lines taken from the two optical parametric amplifiers. The output from OPAI was split using a 50:50 beam splitter to produce two beam lines. The first beam line passed through an optical delay line before impinging on the sample and was assigned as E_1 , where $E_j = E_j(t) \exp(i\vec{k}_j \cdot \mathbf{r} - i\omega_j t)$, while the second beam had

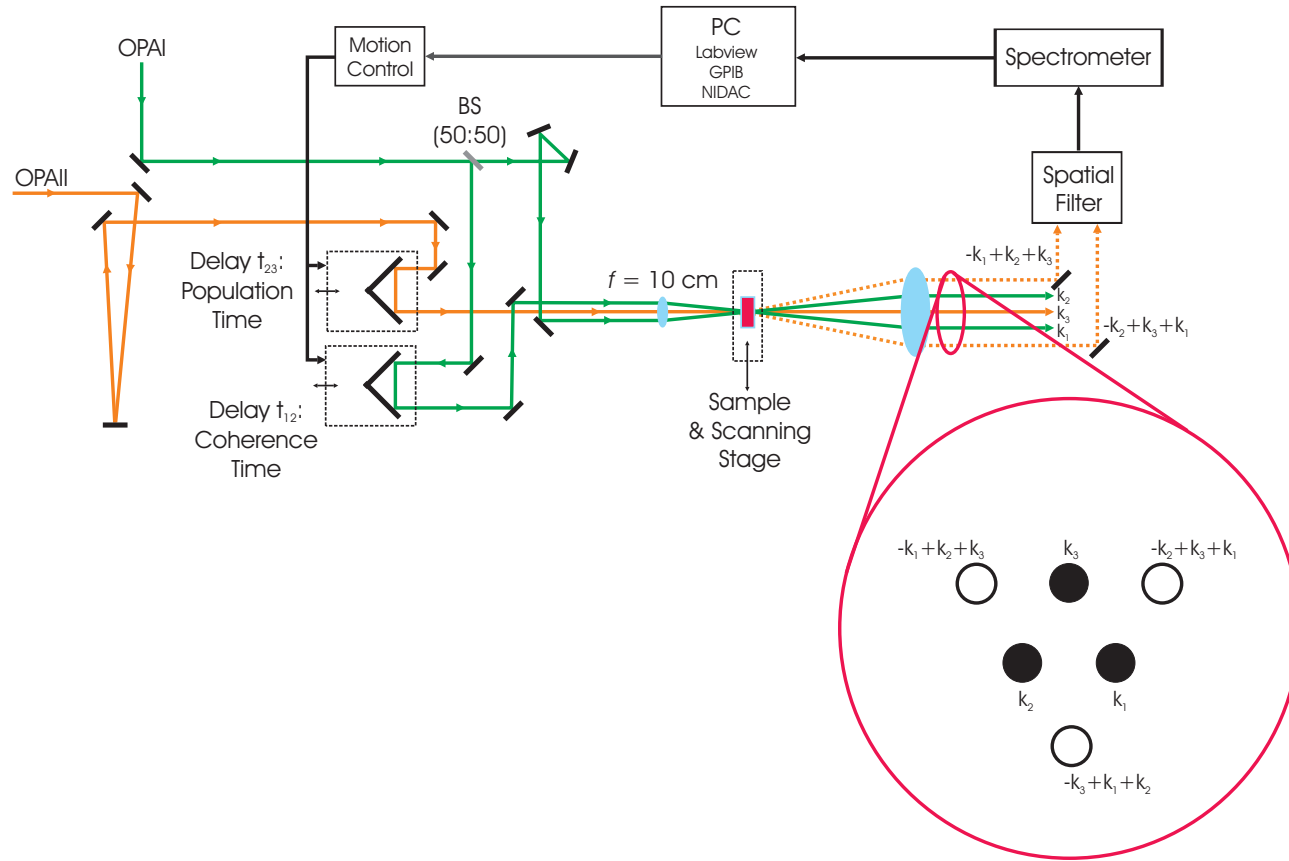


Figure 3.1: Experimental arrangement for photon echo and transient grating experiments showing the three beam lines and two optical delay lines. Enlargement shows the cross-section of the arrangement of the three laser pulses were arranged and the three possible signal wavevectors.

a fixed path and was assigned as E_2 . The output of OPAIL passed through a second optical delay line before impinging on the sample and was assigned as E_3 . The three laser pulses (E_1 to E_3) were arranged in a triangular configuration with approximately 1 cm sides and passed through an ($f = 10$ cm) plano-convex lens so that all three beam lines converged in the sample cell. This produced an approximately 6° angle between each beam (neglecting refraction at the cell) and a waist of approximately $200 \mu\text{m}$. The power of each beam line was adjusted to an average power of 100 mW, measured immediately before the sample cell, resulting in a peak intensity of approximately 3 kW/cm^2 . The emitted signal was measured in the phase-matching direction $\vec{k}_s = -\vec{k}_1 + \vec{k}_2 + \vec{k}_3$, collected using another plano-convex lens to collimate before passing through a spatial filter and a low numerical aperture ($\text{NA} = 0.25$) microscope objective into a fibre coupled spectrometer (Ocean Optics - PC2000).

The selection of a signal wavevector \vec{k}_s is based on the definition of the beam lines as E_1 , E_2 and E_3 , where for the temporal pulse ordering $E_1 \rightarrow E_2 \rightarrow E_3$ a photon echo is generated in the phase-matching direction $\vec{k}_s = -\vec{k}_1 + \vec{k}_2 + \vec{k}_3$ (Table 3.1). In this case where the first pulse E_1 precedes

Table 3.1: Signal Wavevectors, pulse sequences and resultant response functions for resonant four-wave mixing. Note response functions R_2 , R_3 describe the real photon echo while R_1 , R_4 describe the virtual echo or free-induction decay (See section 2.3 on page 30).

Signal wavevector \vec{k}_s	Coherence time	Population time	First pulse	Response functions
$-\vec{k}_1 + \vec{k}_2 + \vec{k}_3$	t_{12}	t_{23}	E_1 E_2 or E_3	R_2, R_3 R_1, R_4
$-\vec{k}_2 + \vec{k}_3 + \vec{k}_1$	t_{23}	t_{31}	E_2 E_1 or E_3	R_2, R_3 R_1, R_4
$-\vec{k}_3 + \vec{k}_1 + \vec{k}_2$	t_{31}	t_{12}	E_3 E_1 or E_2	R_2, R_3 R_1, R_4

the second E_2 the time between the pulses is defined as a positive *coherence* time (t_{12}), and the case where pulse two E_2 precedes the third pulse E_3 the time between the pulses is defined as a positive *population* time (t_{23}). Note the remaining two signal wavevectors $-\vec{k}_2 + \vec{k}_3 + \vec{k}_1$ and $-\vec{k}_3 + \vec{k}_1 + \vec{k}_2$ are equivalent to the selected signal wavevector if the temporal pulse ordering is redefined and $\omega_1 = \omega_2 = \omega_3$ (Table 3.1).

The sample cell for the rhodamine 101 experiments was a 2 mm path-length cell with 1 mm thick quartz windows whereas in the heme protein experiments the sample cell was a 1 mm path-length cell. There are two reasons for using different path-length cells: (i) In the case of rhodamine 101 the signal strength was sufficient to overcome any linear absorption of the laser pulses entering and/or the emitted signal leaving the sample, whereas for the heme proteins this was not the case, thus requiring a shorter path-length cell. (ii) The problem with a 1 mm path-length cell in combination with the small angles between the laser beams was that a signal was also generated from the quartz windows of the cell in addition to the sample. This resulted in a compromise between reducing the angles between the three laser beams and the path-length of the cell to optimise the signal intensity and minimising the signal created in the quartz windows. Fortunately the quartz window signal was partially displaced spatially from the *real* signal and therefore was mostly filtered out by the spatial filter. Figure 3.2 compares the integrated transient grating intensity of the quartz windows of the sample cell and one of the heme protein samples. The intensity of the remaining quartz window signal is approximately 20 % of that of the heme protein intensity; however the quartz window signal decays quickly and is centred around $t_{23} = 0$ whereas the signal from the heme protein is shifted to longer population times and thus the signal from the quartz could be

neglected.

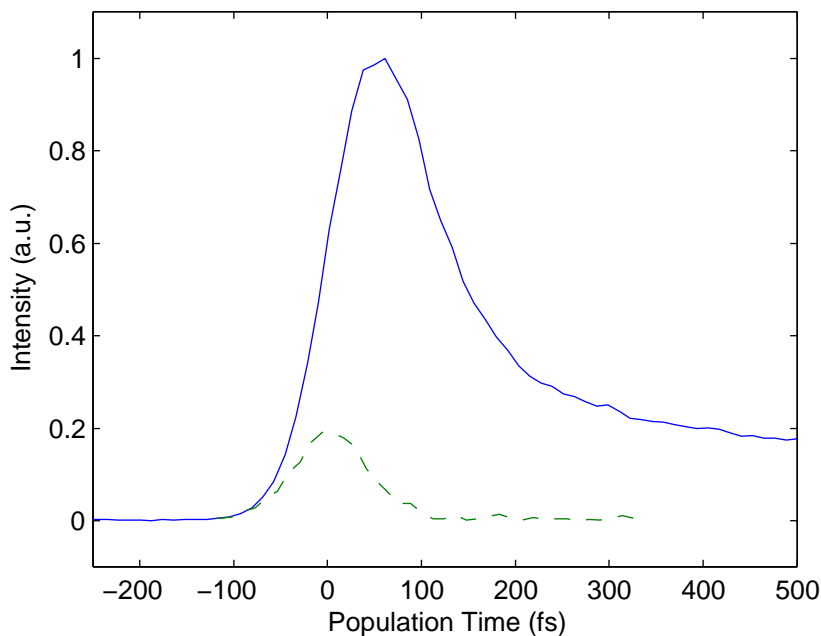


Figure 3.2: Measured transient grating intensity for carbonmonoxy myoglobin (solid line) and the sample cell filled with water (dashed line).

The sample cell was continually translated through the lasers beams to minimise localised heating in the sample and background signal caused by slow (> 1 ms for the heme proteins) sample recovery on a shot-to-shot (1 kHz) basis. The importance of minimising local heating was particularly important for the heme protein samples as they are especially sensitive to temperature causing them to denature (cook), making them opaque and thus diffusive (efficient scatterers). The primary role of the spatial filter in these experiments was to stop the scattered radiation from reaching the detector. This was important as the amount of scattered radiation (sample degradation) increased throughout the experiment and could not easily be removed during the post experimental analysis.

The fibre optic spectrometer used in these experiments, while providing a convenient method of detecting the spectrum, introduced a problem of adding structure to the spectrum. It is believed that some structure was also generated by the sample but the structure was minimised by smoothing the spectrum as it is a known problem for these spectrometers. The smoothing of the measured spectrum had the effect of reducing the resolution of the spectrometer.

3.3 Sample Preparation

Samples of rhodamine 101 (rhodamine 640 perchlorate) were supplied as dried powder from Lambdachrome (product number: 6400) and dissolved in methanol to the required concentration approximately 10^{-4} M.

Samples of horse heart myoglobin were prepared from the purified crystals supplied by Sigma (M-1882). Stock solutions of 2.5 mM (with respect to heme) were prepared by weighing out an appropriate mass of the protein and dissolving in pH 7 degassed phosphate buffer to achieve the required concentration. After vigorous mixing the stock solutions were centrifuged using a bench top centrifuge (Denver Instruments - Force 6) at 5800 g. The supernatant was then transferred to a new centrifuge tube and centrifugation repeated until no undissolved material remained. These solutions were then stored at 4°C.

The final samples of myoglobin were made by diluting appropriate volumes of the stock solution with degassed phosphate buffer pH 7 into a 1 mm path-length quartz cell. Excess sodium dithionite was added to reduce the ferric ion to the ferrous ion and the cell sealed with a rubber septum. The cell was either purged of oxygen using pure nitrogen to produce unbound samples or flushed with pure carbon monoxide (CO) to 1 atmosphere to give

the CO-bound samples. All samples were checked using a Varian - Cary 3E UV/VIS Spectrophotometer to ensure complete conversion to the required product.

3.4 Data Analysis

3.4.1 Numerical Calculations

All numerical calculations were performed using MATLAB; an example script is included in Appendix A. The step size and number of steps for integration was kept to a minimum though checked to ensure the integrated intensity profiles and spectral width did not change if either integration parameter was further optimised. Specifically, for a 80-90 fs laser pulse width the integration step was set to 10 fs and the integration length for the triple integral was set to 18 (180 fs) steps passed the positive coherence or population time, which was sufficient to include the finite pulse width and any lengthening due to the underlying system dynamics. It was not assumed that an ≥ 80 fs pulse width was short relative to the processes occurring during the coherence or population time periods; thus all four terms of Equation 2.25 were included. The spectrally resolved signal was calculated using a fast Fourier transform algorithm; however, this was checked against a discrete Fourier transform and found to give identical results.

Calculations involving chirp were restricted to linear chirp and the lines describing the laser fields, e.g.,

$$\exp(-0.5*((t(a)-t3int)/width).^2)$$

was replaced with the following:

$$\exp(-((1-i*B)/2).*((t(a)-t3int)/width).^2)$$

where B is the spectral phase parameter.

Calculations involving a shift in the signal spectral position as a function of time replaced the lines describing the spectrum of the laser pulses, e.g.,

$$\text{weg} = 2*\pi*3e2/(\text{spec}(1));$$

$$\text{om1} = 2*\pi*3e2/(\text{spec}(2));$$

$$\text{om2} = 2*\pi*3e2/(\text{spec}(3));$$

$$\text{om3} = 2*\pi*3e2/(\text{spec}(4));$$

and

$$\exp(i*(\text{om3}+\text{om2}-\text{om1})*t3\text{int} + i*(\text{om2}-\text{om1})*t2\text{int} - i*\text{om1}*t1\text{int})$$

with the following:

$$\text{weg} = 2*\pi*3e2/(\text{spec}(1));$$

$$\text{wi} = 2*\pi*3e2/(\text{spec}(2));$$

$$\text{wf} = 2*\pi*3e2/(\text{spec}(3));$$

$$\text{wft23} = \text{wf} + ((\text{wi}-\text{wf})/2)*\text{erf}(-t23/\text{spec}(4)) + ((\text{wi}-\text{wf})/2);$$

and

$$\exp(i*(\text{wft23}(\text{pop}))*t3\text{int} + i*(\text{wft23}(\text{pop})-\text{wi})*t2\text{int} - i*\text{wi}*t1\text{int})$$

3.4.2 Inverse Linewidth, Third-Order Polarisation Temporal Width and Peak Shift

The inverse linewidth, temporal width of the photon echo signal pulse and peak shift results were all determined by fitting Gaussian profiles to the respective signal. The inverse linewidth was calculated as the Fourier limited temporal width of the full-width-half-maximum spectral width taken from a Gaussian fit to the spectrally resolved signals:

$$\Delta f_{\text{FWHM}}^{-1}(t_{23}) = 0.441 / \left(\sigma_f(t_{23}) 2\sqrt{2 \ln(0.5)} \right), \quad (3.1)$$

where $0.441 = \Delta f \cdot \Delta t$ is the time-bandwidth product for a transform limited Gaussian pulse [42] and $\sigma_f(t_{23})$ is the standard deviation of a fitted Gaussian to the spectrally resolved signals.

The temporal width of the photon echo signal pulse $\Delta t_{\text{FWHM}}(t_{23})$ was calculated from $\sigma_t(t_{23})2\sqrt{2 \ln 0.5}$, where $\sigma_t(t_{23})$ is the standard deviation of a fitted Gaussian to $S^{(3)}(t, 0, t_{23}) = |P^{(3)}(t, 0, t_{23})|^2$.

The photon echo peak shift $\Delta t_{12}^*(t_{23})$ was calculated as the centre position of a Gaussian fitted to $S^{(3)}(t, t_{12}, t_{23})$ along the t_{12} axis for all values of t_{23} .

3.4.3 Analytical Fitting

Inverse Linewidth and Peak Shift

The inverse linewidth and peak shift results were fitted using a function based on the various correlation function Brownian oscillators (See section 2.2.3 on page 27) as required, such that:

$$M(t) = \sum_k A_k \times \exp(-\Lambda_k t) + \sum_l A_l \exp\left(-\frac{\gamma_l t}{2}\right) \left(\cos(\omega_l t) + \left(\frac{\gamma_l}{2\omega_l}\right) \sin(\omega_l t) \right) \quad (3.2)$$

and

$$F(t) = A_0 \times (M(t - t_0)) + C. \quad (3.3)$$

Integrated Intensity

Analytical fits to integrated intensity measurements were performed using a convolution fit such that:

$$\begin{aligned} \text{Fit}(t) &= G(t) \otimes F(t) \\ &= \int_0^\infty dt' G(t') F(t - t'), \end{aligned} \quad (3.4)$$

where $G(t)$ describes the response function and $F(t)$ is the fit function. The response function $G(t)$ was assumed to be a Gaussian pulse and the position and width were free-fit parameters rather than fixed at time zero or as the autocorrelation width. The fit function $F(t)$ was comprised of various correlation function Brownian oscillators described above.

Heme Protein Results

The high density of vibrational modes present in the heme protein results required the use of a more sophisticated procedure to fit the data. Rather than include an underdamped Brownian oscillator in the fit function the inverse linewidth data was first fit using only exponential decays to describe the dynamics. The resultant residuals were Fourier smoothed then fitted using a method called the matrix pencil method (MPM) [43]. The matrix pencil method is used because of the large number of vibrational modes present for the heme proteins; the Fourier smoothing is required because the matrix pencil method is sensitive to noise. The Fourier smoothing was applied as a low-pass filter to remove frequencies higher than those which the spectral width of the applied laser pulses could excite, $5\sigma_{\text{Laser}}$ approximately 350 cm^{-1} . The matrix pencil method [43] is an alternative method to Linear Predictive Singular Value Decomposition (LPSVD) [44] for fitting damped

sinusoids and performs better for noisy signals and/or when the data is strongly damped or truncated. In short it can be used to estimate the signal poles (z_i ; frequency and damping) of damped sinusoids directly by solving a generalised eigenvalue problem. The amplitude and phase were estimated by using linear least-squares analysis. A more detailed description and example in MATLAB code can be found in the literature [43].

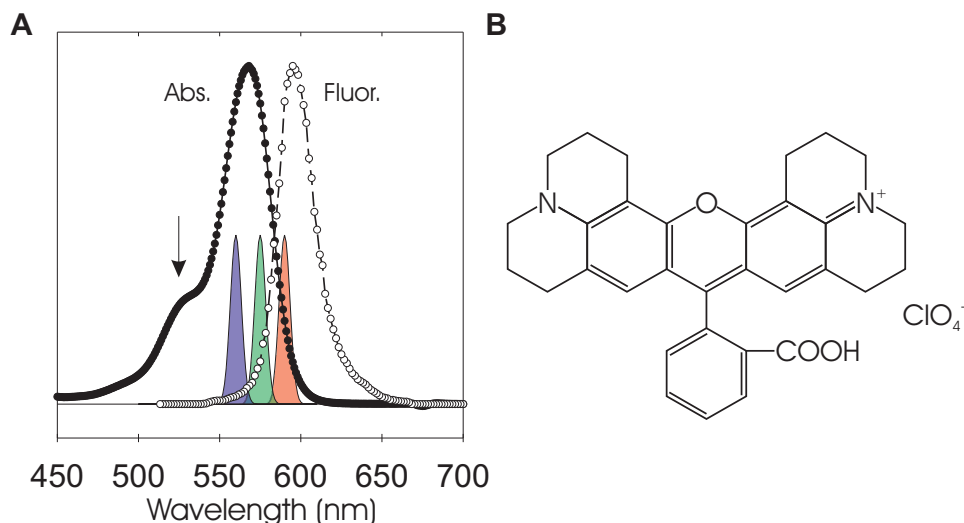
Chapter 4

Spectrally-Resolved Photon Echoes of a Laser Dye

Some of this work and related studies have appeared in the following publications:

1. L.V. Dao, C.N. Lincoln, R.M. Lowe and P. Hannaford, *Femtosecond Laser Spectroscopy*, ch. 8, "Spectrally Resolved Two-Colour Femtosecond Photon Echoes," pp. 197-224. Springer: New York, 2005.
2. L.V. Dao, C.N. Lincoln, R.M. Lowe, M.T.T. Do, P. Eckle and P. Hannaford, "Spectrally Resolved Two-Colour Femtosecond Photon Echoes: A New Multidimensional Technique for Studying Molecular Dynamics," *Laser Physics* **15**(9), pp. 1257-1268, 2005.
3. L.V. Dao, C.N. Lincoln, R.M. Lowe and P. Hannaford, "Spectrally Resolved Femtosecond Two-Color Three-Pulse Photon Echoes: Study of Ground and Excited State Dynamics in Molecules," *Journal of Chemical Physics* **120**(18), pp. 8434-8442, 2004.
4. L.V. Dao, C.N. Lincoln, M.T.T. Do, P. Eckle, R.M. Lowe and P. Hannaford, "Spectrally Resolved Femtosecond 2-Colour 3-Pulse Photon Echoes: A New Spectroscopic Tool to Study Molecular Dynamics," *Australasian Physical & Engineering Sciences in Medicine* **27**(4), p. 224-229, 2004.
5. L.V. Dao, C.N. Lincoln, R.M. Lowe and P. Hannaford, "Spectrally Resolved Two-Colour Three-Pulse Photon Echo Studies of Vibrational Dynamics of Molecules," *Physica B-Condensed Matter* **327**(1), pp. 123-128, 2003.

4.1 Introduction



In this Chapter the spectrally resolved transient grating technique is applied to a laser dye rhodamine 101 (rhodamine 640 perchlorate; Rh101) to further characterise the technique before studying the more complex biological systems. In Chapter 2 the spectrally resolved technique was applied to a model two-level system coupled to one intramolecular vibrational mode and two intermolecular solvation (homogeneous broadening) modes in the presence of inhomogeneous broadening. It was assumed for this model system that the excited state lifetime was long (infinite) compared to the relaxation time of the (in)homogeneous broadening. Rhodamine 101 on the other hand is known to undergo rapid intraband population relaxation although it has a long, of order nanoseconds, excited state lifetime. While the presence of the

rapid intraband population relaxation is not ideal for comparing the theoretical results presented in Chapter 2 to the experimentally measured results presented in this Chapter, rhodamine 101 does provide an excellent example of the advantages of spectrally resolving the transient grating signal.

Rhodamine 101 is commonly used as a laser dye, a biological fluorescence marker and as a fluorescence quantum yield standard. The chemical structure of rhodamine 101 shows there are relatively few vibrational degrees of freedom compared to other rhodamine dyes where the two amine substituents are free to rotate resulting in extremely rapid vibrational relaxation (Fig. 4.1(b)).

The steady-state absorption and fluorescence spectra for rhodamine 101 in methanol are shown in Figure ???. Taking the difference between the spectral positions of the absorption and fluorescence maxima (approximately 567 and 594 nm) and assuming the relaxation within the excited state occurs on a time scale much faster than the population decay, it is possible to estimate a Stokes shift 2λ of approximately 800 cm^{-1} and an energy gap of frequency $\bar{\omega}_{eg}^o$ approximately 17212 cm^{-1} (581 nm) between the lowest lying vibrational levels of the ground $|g, \nu_0\rangle$ and excited $|e, \nu_0\rangle$ states.

Recent studies by Marcano and Urdaneta [45] used a photothermal method to study the fluence dependence of the fluorescence quantum yield of rhodamine 101 in ethanol. The authors proposed rhodamine in solution could be considered as a two electronic level system with singlet ground and excited states. Excited state absorption and transitions into triplet states were neglected because of the low absorption cross section and very long time scales for the inter-system crossings, respectively. In order to describe the results, a model was proposed detailing three different dynamic time scales: the excited state lifetime T_{1e} , the effective dephasing

time T_2 and a vibrational (intraband) relaxation time $T_{1\nu}$. The values for the excited state lifetime and the vibrational relaxation time were found to depend on the fluence of the applied pulses. The proposed timescale ranges for two of these processes were: $2 \times 10^{-9} \text{ s} > T_{1e} > 0.35 \times 10^{-9} \text{ s}$ and $10^{-12} \text{ s} > T_{1\nu} > 2 \times 10^{-14} \text{ s}$. The effective dephasing time was set to $T_2 = 30 \text{ fs}$, in reasonable agreement with the previously measured range of $7 - 90 \text{ fs}$ for rhodamine in different solvent solutions using four-wave-mixing [46].

In this Chapter rhodamine 101 in methanol is used as a model system in the first implementation of spectrally resolved three-pulse photon echo spectroscopy in the visible region [32,33]. It will be shown how the spectrally resolved transient grating technique was used to characterise the effect of rapid intraband population relaxation and determine that rhodamine 101 has at least two distinct dephasing times. In addition it will be shown how spectrally resolved transient grating that can be used to separate the different ground and excited state contributions to the integrated intensity signal. It will be shown using two-colour spectrally resolved transient grating the transient effects as an initially created wavepacket is transferred from the spectral window defined by the first two pulses to that of the third pulse. Finally, the effect of using strong laser pulses that can induce an AC-Stark effect and shift transition wavelengths is investigated.

4.2 Spectrally Resolved Transient Grating of Rhodamine 101

4.2.1 Laser-Wavelength Dependent One-Colour Spectra

The one-colour spectrally resolved transient grating spectra of rhodamine 101 in methanol (Fig. 4.2) were measured using the experimental apparatus described in section 3.2 on page 45. Three experiments were performed using centre laser wavelengths of 560, 575 and 590 nm. The signals were measured in the phase-matching direction $\vec{k}_s = \vec{k}_3 + \vec{k}_2 - \vec{k}_1$, at a coherence time $t_{12} = 0$ and population times $t_{23} = -0.2$ to 6 ps.

The time-integrated transient grating spectrum for each experimental wavelength, 560, 575 and 590 nm, were calculated by summing over all population times (Fig. 4.3). Superimposed on the signal spectrum are the corresponding laser spectrum calculated by assuming a 90 fs pulse width and transform limited pulses. It can be seen the transient grating spectra exhibit a significant laser-wavelength dependence. In the 560 nm experiment there is a small increase in the spectral width of the transient grating spectra compared to the laser spectra. By contrast, the 575 and 590 nm signal spectra are significantly broader and red-shifted from the laser spectra. Moreover, there are significant shoulders present in both signal spectra, indicative of underlying vibronic structure. Thus, to analytically describe the 575 nm and 590 nm signal spectrum lineshapes multiple Gaussian profiles are required.

Each of the transient grating spectra were fitted using Gaussian profile(s) to describe the spectral lineshape at each population time point. To account for the structure in the spectral lineshapes of the 575 and 590 nm experiments three Gaussian profiles were used whereas only a single Gaussian was

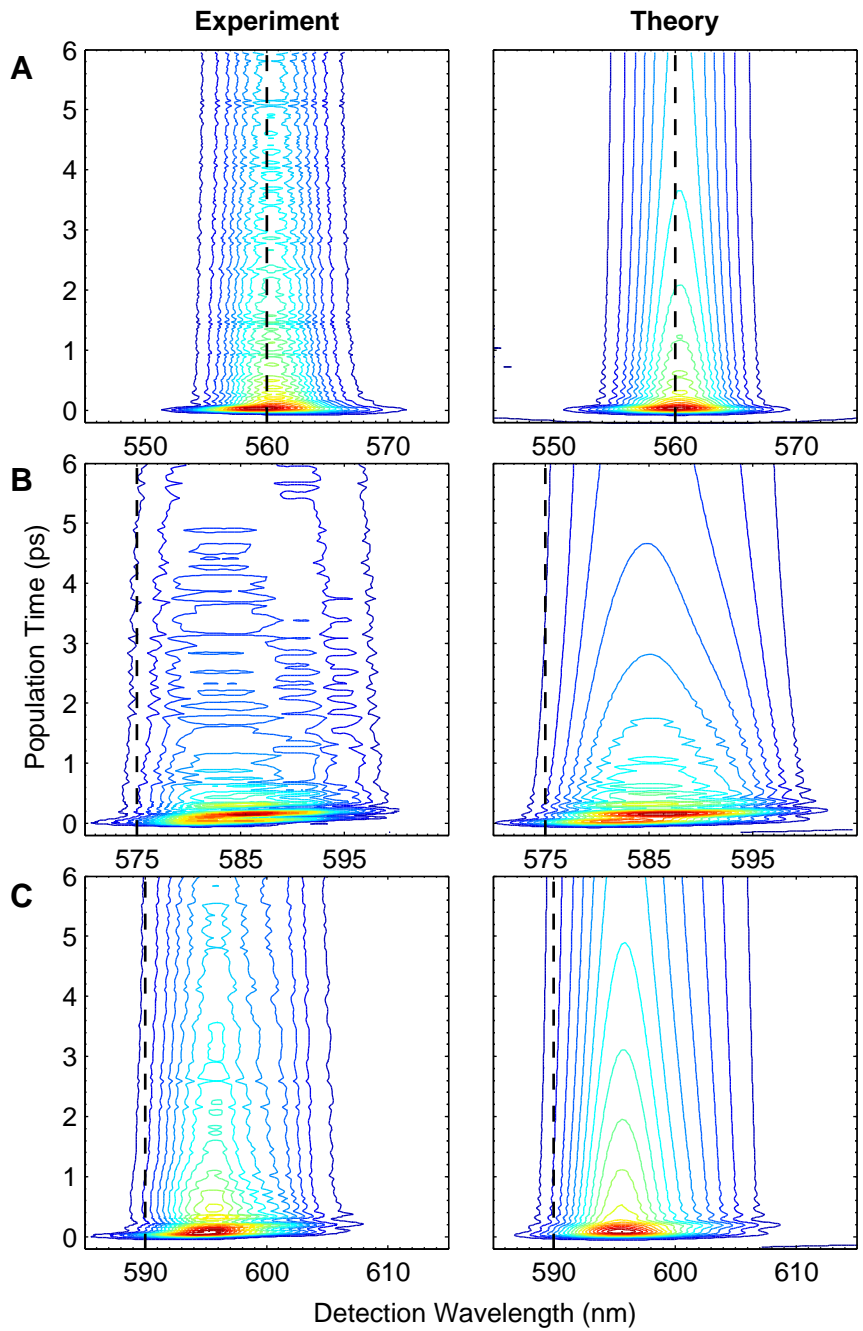


Figure 4.2: Measured and theoretical three-pulse one-colour transient grating spectra of rhodamine 101 in methanol for three different laser wavelengths centred at (a) 560 nm, (b) 575 nm and (c) 590 nm. Dashed lines indicate the central wavelength of the applied laser pulses.

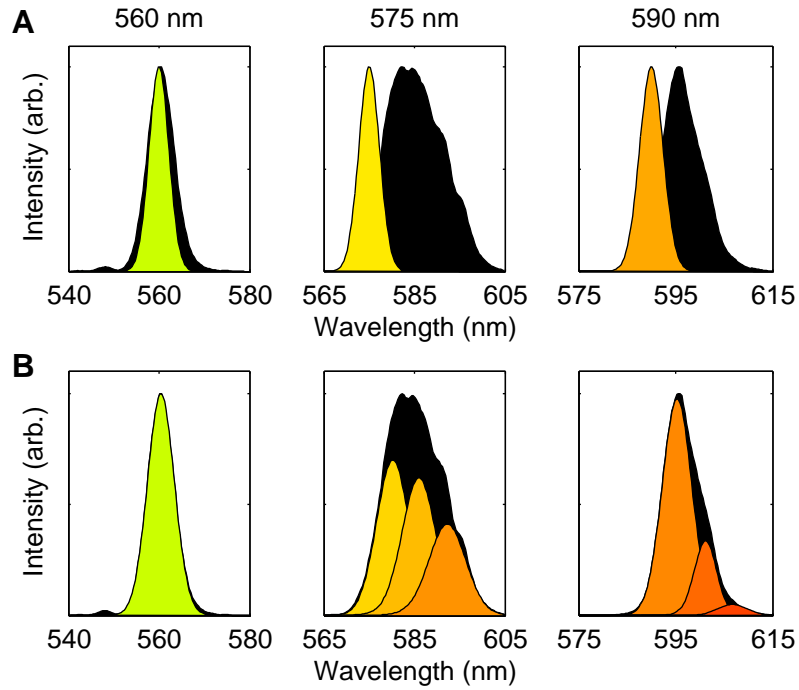


Figure 4.3: Time-integrated transient grating signal spectrum for three laser wavelengths 560, 575 and 590 nm (solid black curves). (a) Overlay of calculated laser spectrum assuming 90 fs transform limited laser pulses and a Gaussian pulse shape (Solid 560, 575 and 590 nm curves). (b) Overlay of each signal channel spectrum calculated from fitting multiple Gaussian profiles to the signal spectrum. The 560 nm signal spectrum is overlaid by one Gaussian (solid 560 nm curve), the 575 nm laser wavelength signal spectrum is overlaid with three fitted Gaussian profiles (solid 580, 586 and 593 nm curves) and the 590 nm laser wavelength signal spectrum is overlaid with three fitted Gaussian profiles (solid 595, 601, 607 nm curves).

required for the 560 nm signal spectrum (Fig. 4.3). The spectral fit results are presented as the population time-dependent integrated intensity, centre frequency and spectral width (Fig. 4.4). The variables (amplitude, centre frequency and spectral width) of three fitted Gaussian profiles used to fit the 575 nm experimental result were completely independent. By contrast, to achieve a reasonable fit for the 590 nm result the spectral width variables of the two red-shifted Gaussian profiles were fitted as a single variable. Moreover, while the contribution of the far red-shifted component appears insignificant ($< 5\%$ of the total intensity) the quality of the fit using only two Gaussian profiles became unacceptable. It is noted that each of the spectral fits have well resolved and unique centre frequencies that will from hereon be referred to as *signal channels*, i.e., the 575 nm experiment has three signal channels 580, 586 and 593 nm and the 590 nm transient grating also has three channels 595, 601 and 607 nm. The signal channels were broken down into two categories called *field-resonant* and *off-field-resonant* depending on their spectral overlap with the applied laser pulses. There are three field-resonant signal channels 560, 580 and 595 nm, the remaining signal channels are deemed off-field-resonant (Fig. 4.3).

Accompanying the measured signals are results calculated using theoretical models based on the Multimode Brownian oscillator model presented in Chapter 2 (Figs. 4.2 and 4.4). The final theoretical spectra shown in Figure 4.2 were calculated by combining the separate fits to each of the signal channel(s). Moreover, fits to the field-resonant signal channels (560, 580 and 595 nm) were calculated using Equation 4.1 (See Eqs. 2.27 and 2.25) whereas the off-field-resonant signal channels for the 575 and 590 nm experiments ([586 and 593 nm] and [601 and 606 nm], respectively) were calculated using a formalism that describes coherent Raman scattering processes (Eq. 4.2).

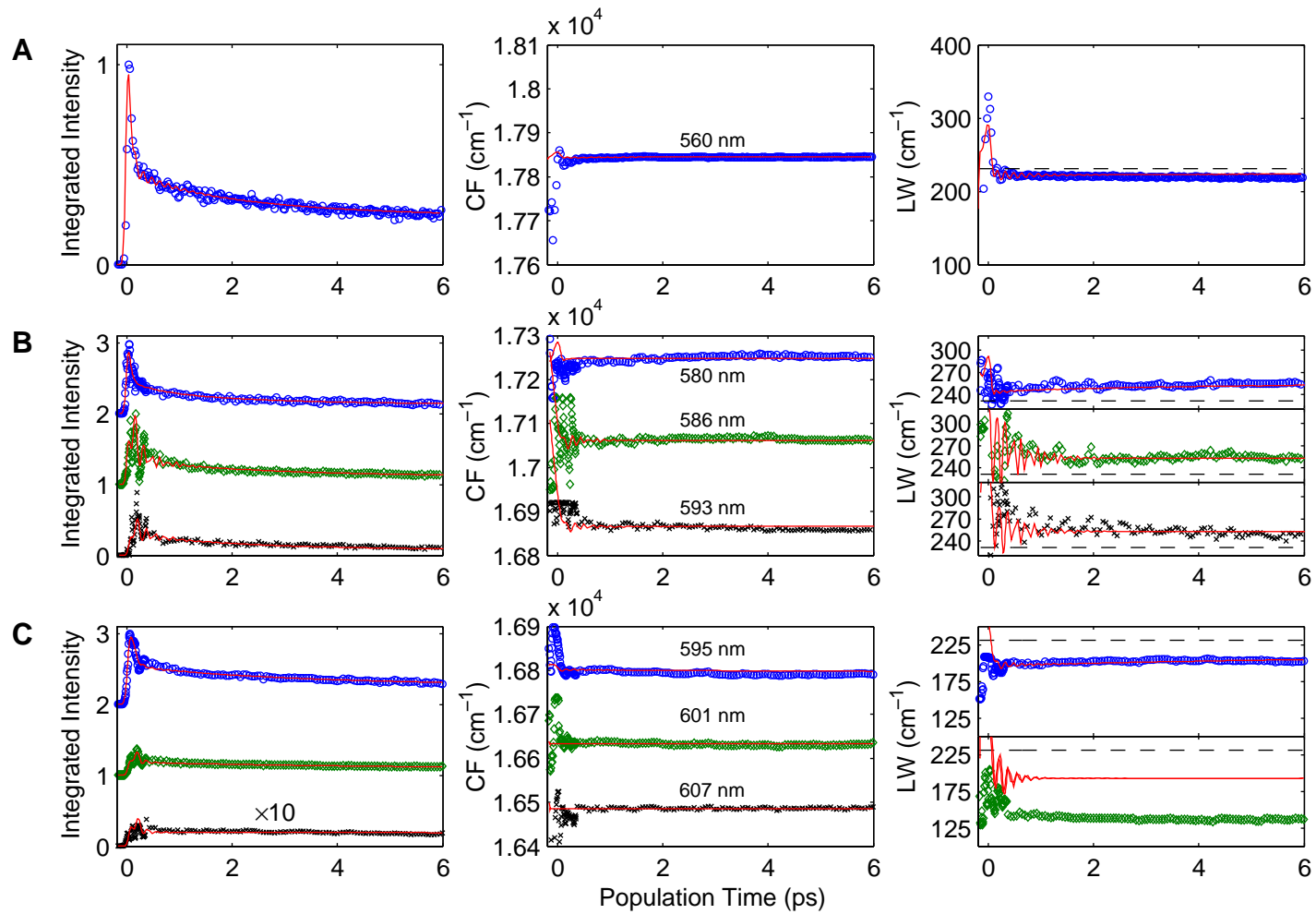


Figure 4.4: Intensity, centre frequency and inverse linewidth plots for three laser wavelengths (a) 560 , (b) 575 and (c) 590 nm. The 575 and 590 nm laser wavelength results have three separate signal channel curves (circles, diamonds and crosses) as indicated. Solid lines show the calculated theoretical fit.

In all cases the parameter optimisation was performed using least-squares fitting of the integrated intensity and visual inspection of the centre frequency and spectral width plots rather than the two-dimensional data set (i.e., wavelength versus population time).

$$S_{\text{SPE}}^{(3)}(\omega, t_{12}, t_{23}) = \left| \int_{-\infty}^{\infty} dt P^{(3)}(t, t_{12}, t_{23}) \exp(i\omega t) \right|^2. \quad (4.1)$$

The impulsive coherent Raman scattering components of the signals were calculated using the approach outlined in Ref [19] as follows:

$$\begin{aligned} S_{\text{ICRS}}(\omega, t_{23}) = & \\ & \left| \int_{-\infty}^{\infty} dt E_3(t) \exp(i\omega t) \right. \\ & \times \left| \int_0^{\infty} dt_2 E_2(t + t_{23} - \delta t_{23} - t_2) E_1^*(t + t_{23} - \delta t_{23} - t_2) \right. \\ & \times \left. \exp [i(\omega_2 - \omega_1)t_2] \chi_{\alpha\alpha}(t_2) \right|^2, \end{aligned} \quad (4.2)$$

$$\chi_{\alpha\alpha}(t) = (2/\hbar)M''(t), \quad (4.3)$$

where $M''(t)$ is the imaginary component of the correlation function $M(t)$ (Eqs. 2.18 and 2.22).

There are several assumptions made leading to Equation 4.2 (i) only the ground-state contributions to the signal (R_3, R_4 ; Eq. 2.25 [see section 2.3 on page 32]) need to be considered. Here the author [19] makes a note that under off-resonant conditions many excited electronic states need to be considered though this necessity is removed by summation over all excited states making the two-level system valid in the present formalism. (ii) For off-resonant processes, t_1 and t_3 are neglected as they are very short compared with the pulse durations. This corresponds to pulses that are long

compared with dephasing though short compared to the nuclear dynamics. (iii) Moreover, the author switched to the doorway-window formalism¹ of the nonlinear response functions, where $\omega_s = \omega_1 + \omega_3 - \omega_2$, which is weakly varying in the off-resonant condition, is replaced by an average frequency, say $\omega_p \equiv (\omega_1 + \omega_2)/2$, and for impulsive (femtosecond) techniques $\omega_1 = \omega_2$ so that all spectral dependences are neglected. Using the same description the fields can also be set to $E_1 = E_2 = E_p$. (iv) Finally, a δt_{23} term is added to take account of the finite time taken for a propagating wavepacket to relax from the spectral window created by the laser pulses (doorway) to the spectral position where the signal is emitted (window). It is noted that while this final addition is crude, it provides some insight into the underlying dynamics and is a variation from the model described in Ref. [19].

The fit parameters for the underlying correlation functions at each signal channel are listed in Table 4.1. In all of the theoretical fits the underlying correlation function used in Equations 4.1 and 4.2 comprised three over-damped (Eq. 2.22) and one under-damped Brownian oscillator(s) (Eq. 2.18), though with varying characteristics (Table 4.1). The over-damped Brownian oscillators were separable into three different relaxation time ranges 67 fs, 3-5 ps and $\gg 6$ ps characteristic of the so called *coherent artifact* or *coherent spike*, homogeneous dephasing (solvation) and (in)homogenous processes, respectively. The underdamped Brownian oscillator (vibrational mode) had a characteristic frequency f_ν of approximately 208 cm^{-1} with a relaxation time γ_ν^{-1} of approximately 240 fs (Table 4.1). The excited state lifetime T_1 is known to be 1-3 ns [46,47] and was neglected. The total coupling strength Δ was set to 0.0797 ($\lambda = 0.0809 \text{ rad fs}^{-1}$, where 2λ is the Stokes shift). Note, linear chirp ($B = 0.55$) was added to the fits of the

¹A detailed description of the doorway-window formalism can be found in Ref. [19] and is beyond the scope of this thesis.

Table 4.1: Parameters for theoretical fits to the data presented in Figs. 4.2 and 4.4. The amplitude of the oscillators was normalised so that $\sum_i A_i = 1$, $\Lambda_3^{-1} = \infty$ and the total coupling strength Δ was set to 0.0797 ($\lambda = 0.0809$ rad fs^{-1} , where 2λ is the Stokes shift). The coupling strength of each Brownian oscillator is $\Delta_i = A_i \times \Delta$.

λ_L (nm)	560	575 ^a			590 ^b		
channel	560	580	586	593	595	601	607
Eq.	4.1	4.1	4.2	4.2	4.1 ^c	4.2	4.2
A_1	0.31	0.31	0.30	0.19	0.41	0.24	0.20
Λ_1^{-1} (fs) ^d	67	67	67	67	67	67	67
A_2	0.22	0.63	0.08	0.14	0.10	0.05	0.02
Λ_2^{-1} (ps)	3.1	3.9	3.4	3.1	5.0	5.0	5.2
A_3	0.37	0.02	0.23	0.34	0.39	0.28	0.39
A_ν	0.10	0.04	0.39	0.32	0.10	0.44	0.39
γ_ν^{-1} (fs)	317	318	244	251	278	135	116
f_ν (cm^{-1}) ^e	214	215	217	199	207	203	200
A_0	0.96	0.86	0.97	0.51	0.96	0.33	0.04
δt_{23} (fs)	15	30	...	15	30
λ_s (nm) ^f	561.1	580.1	586.1	592.9	594.9	601.2	606.6

^a Linear chirp ($B = 0.55$) was included in all fits of the 575 nm data.

^b A pulse width 108 fs was used to account for the narrower pulse width of the 590 nm laser pulses.

^c Only the response functions describing a population state in the ground state (R_3 and R_4) in Equation 2.25.

^d The lower limit of Λ_1^{-1} was set to $94/\sqrt{2} = 66.5$ fs where 94 fs was the full width at half maximum of the 560 and 575 nm laser pulses.

^e $\omega_\nu = 2\pi f_\nu$

^f $\lambda_s = 2\pi c/\omega_s$ and $\omega_s = \omega_1 = \omega_2 = \omega_3$

575 nm experimental data and 108 fs laser pulses were used for the 590 nm fits to account for the variation in the spectral width of the different signal channels (Fig. 4.4). A 15 fs delay was added between each successive signal channel as the red-shift increased, e.g., the 586 and 593 nm signal channels were delayed relative to the 580 nm signal channel by 15 fs and 30 fs, respectively.

Finally, the centre frequency data for the 575 nm experiment is revisited to highlight the differences in the relaxation times between the 580 nm and the 593 nm signal channels. Analytical fits (Eqs. 4.4 and 4.5) to the 580 nm and 593 nm centre frequency signal channels were performed (Fig. 4.5) to highlight their differences and because of limitations of the theoretical model that will be discussed in more detail below. The fit was of the form:

$$M(t) = \sum_k A_k \times \exp(-\Lambda_k t) + A_\nu \exp\left(-\frac{\gamma_\nu t}{2}\right) \left(\cos(\omega_\nu t + \phi_\nu) + \left(\frac{\gamma_\nu}{2\omega_\nu}\right) \sin(\omega_\nu t + \phi_\nu) \right) \quad (4.4)$$

Table 4.2: Parameters for analytical fits to the data presented in Figure 4.5. The amplitude of the oscillators was normalised so that $\sum_i A_i = 1$. See text for details.

Signal Channel	580 nm	593 nm
A_1	0.60	0.66
Λ_1^{-1} (fs)	67	343
A_2	0.14	0.14
Λ_2^{-1} (ps)	1.2	5.8
A_ν	0.27	0.20
γ_ν^{-1} (fs)	73	228
f_ν (cm^{-1})	227	216
ϕ_ν (fs)	0	20
A_0 (cm^{-1})	-197	167
C (cm^{-1} [nm])	17254[579.6]	16850[593.5]

and

$$Fit(t) = A_0 \times M(t) + C, \quad (4.5)$$

where, $\omega_\nu = 2\pi f_\nu$. The results of the fit show the 580 nm signal channel dephasing ($\Lambda_{k's}$) and intramolecular (γ_ν) dynamics are significantly faster than the corresponding 593 nm signal channel decay times. This is assigned to differences in the ground and excited state relaxation times, respectively.

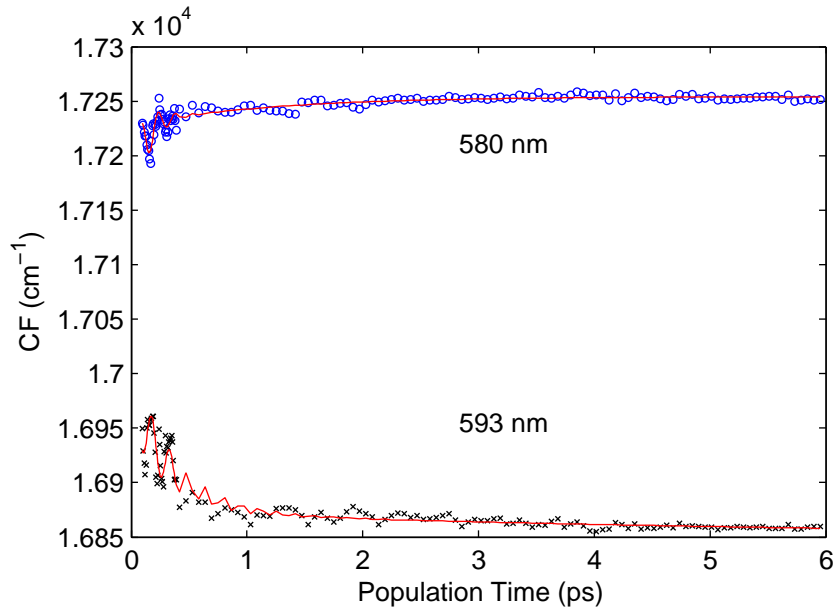


Figure 4.5: One-colour transient grating centre frequencies measured using 575 nm laser pulses of two signal channels as labelled. Solid lines are analytical fits. See text for details.

4.2.2 Laser-Wavelength Dependent Two-Colour Spectra

The experimental data presented in this section were collected using the same apparatus and three experimental wavelengths (560, 575 and 590 nm) used for the one-colour experiments. In this case, however, the wavelength of the third laser pulse was tuned to a different wavelength than the first

two pulses, i.e. $\lambda_{1,2} \neq \lambda_3$, where λ_i is the wavelength of the i th applied laser pulse E_i . Thus six experiments were carried out using the six available combinations, 560-575, 560-590, 575-560, 575-590, 590-560 and 590-575 listed in order of $\lambda_{1,2} - \lambda_3$, respectively (Fig. 4.6). The one-colour spectrally resolved transient grating spectra are also included in Figure 4.6 for comparison.

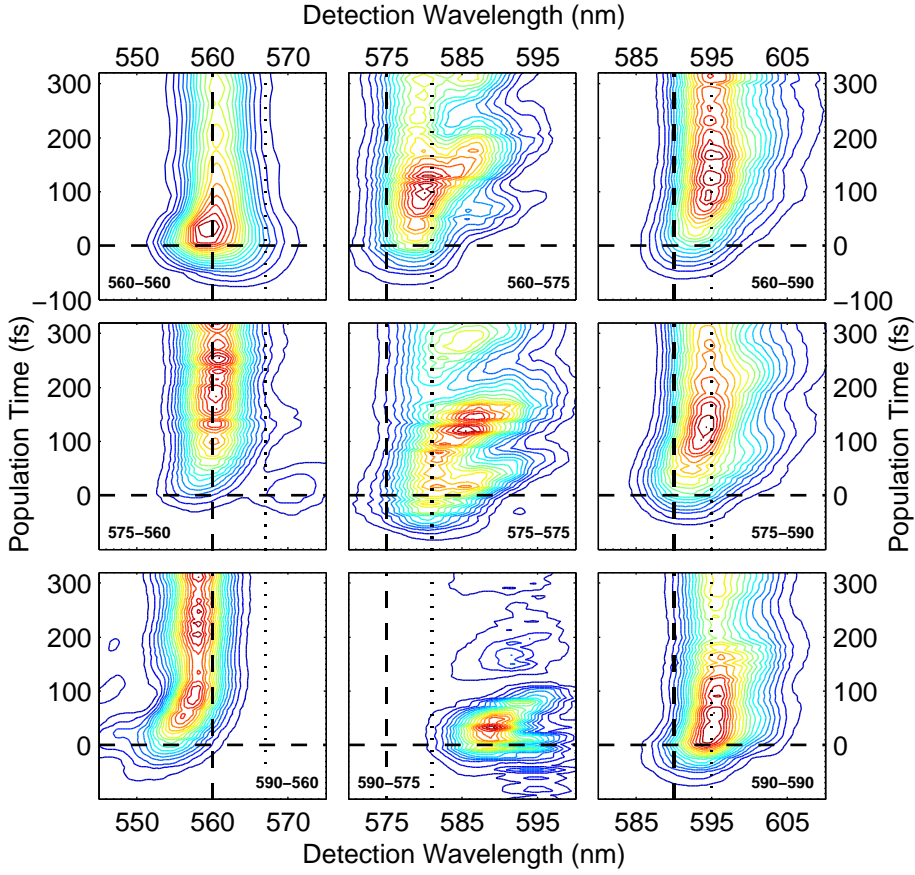


Figure 4.6: Measured two-colour three-pulse transient grating spectra of rhodamine 101 for combinations of the three laser wavelengths 560, 575 and 590 nm as indicated. Dashed lines indicate the central wavelength of the applied laser pulses (vertical) and time zero (horizontal). Dotted lines indicate the spectral positions of the absorption maximum (left column), 0-0 transition ω_{eg}^o (centre column), and the fluorescence maximum (right column). One-colour spectra are included for comparison.

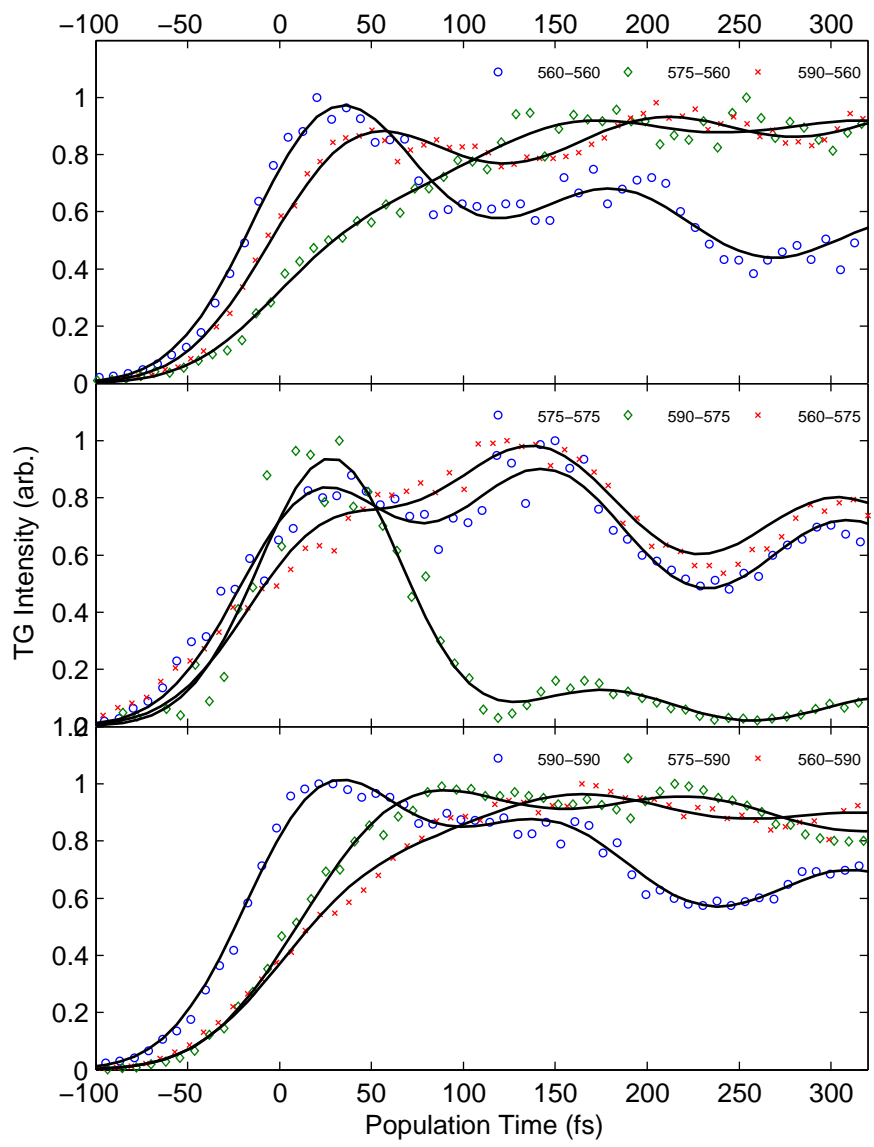


Figure 4.7: Measured two-colour three-pulse transient grating integrated intensity curves of rhodamine 101 for combinations of the three laser wavelengths 560, 575 and 590 nm as indicated. One-colour spectra are included for comparison. Solid line represent analytical fits. See text for details.

Here the initial wavepacket created by the interaction of the pump pulses $E_{1,2}$ is referred to as the *doorway* state and the region specified by the spectral width and position of the probe pulse E_3 as the *window* state. Moreover, the case when the doorway state is blue-detuned from the window state $\lambda_{1,2} > \lambda_3$ is termed *downhill* and conversely when the doorway is red-detuned from the window $\lambda_{1,2} < \lambda_3$ as *uphill*.

To illustrate more clearly the difference between the one- and two-colour signal response the integrated intensity results (Fig. 4.7) were not separated into separate signal channels, as was the case for the one-colour section above. The two-colour integrated intensity signals (with the exception of the 590-575 result) were fitted using an analytical expression $F(t)$ that includes two overdamped and one underdamped correlation function $M(t)$ (Eqs. 2.22 and 2.18) convoluted with the system response function $G(t)$ such that:

$$\begin{aligned} Fit(t) &= G(t) \otimes F(t) \\ &= \int_0^\infty dt' G(t') F(t-t'), \end{aligned} \quad (4.6)$$

$$\begin{aligned} F(t) &= A_1 \times [1 - \exp(-\Lambda_1 t)] + A_2 \times \exp(-\Lambda_2 t) \\ &+ A_\nu \exp\left(-\frac{\gamma_\nu t}{2}\right) \left(\cos(\omega_\nu t + \phi_\nu) + \left(\frac{\gamma_\nu}{2\omega_\nu}\right) \sin(\omega_\nu t + \phi_\nu) \right), \end{aligned} \quad (4.7)$$

where $G(t)$ was assumed to be a Gaussian centred at $t_{23} = 0$ and full width at half maximum 94 fs. Note the first overdamped correlation function in Equation 4.7 is an exponential rise rather than the conventional exponential decay. The one-colour and the 590-575 two-colour integrated intensity signals were fitted with an analytical expression $F(t)$ where the first overdamped correlation function in Equation 4.7 is replaced with the an expo-

nential decay such that:

$$F(t) = A_1 \times \exp(-\Lambda_1 t) + A_2 \times \exp(-\Lambda_2 t) + A_\nu \exp\left(-\frac{\gamma_\nu t}{2}\right) \left(\cos(\omega_\nu t + \phi_\nu) + \left(\frac{\gamma_\nu}{2\omega_\nu}\right) \sin(\omega_\nu t + \phi_\nu) \right). \quad (4.8)$$

Table 4.3: Parameters of analytical fit to one- and two-colour transient grating integrated intensity results presented in Figure 4.7. The amplitude of the oscillators was normalised so that $\sum_i A_i = 1$.

$\lambda_{E_{1,2}} - \lambda_{E_3}$ (nm)	A_1	Λ_1^{-1} (fs)	A_2	Λ_2^{-1c} (fs)	A_ν	γ_ν^{-1d} (fs)	f_ν^d (cm^{-1})	ϕ_ν (fs)
560-560 ^a	0.43	65	0.31	3100*	0.26	240	208	23
575-560 ^b	0.60	80	0.29	367	0.11	240	208	-2
590-560 ^b	0.43	97	0.45	64	0.12	240	208	42
575-575 ^a	0.39	65	0.28	3500*	0.32	240	208	-13
590-575 ^a	0.67	10	0.08	1983	0.25	240	208	-31
560-575 ^b	0.30	25	0.42	75	0.27	240	208	-18
590-590 ^a	0.50	63	0.30	4000*	0.20	240	208	-10
575-590 ^b	0.62	47	0.28	236	0.11	240	208	3
560-590 ^b	0.51	51	0.36	155	0.12	240	208	66

^a Fit using Equations 4.6 and 4.8, see text for details.

^b Fit using Equations 4.6 and 4.7, see text for details. Note Λ_1^{-1} is a rise time.

^c Asterisk * denotes fixed values.

^d All values were fixed at $\gamma_\nu^{-1} = 240$ fs and $f_\nu = 208$ cm^{-1} .

The analytical fit results of the one- and two-colour integrated intensity signals are listed in Table 4.3. The results for the two-colour experiments, with the exception of 590-575, show; (i) a delayed signal response and associated rise time that results in a shifted intensity peak position, (ii) the rise time increases as the wavelength difference $\Delta\lambda = |\lambda_{1,2} - \lambda_3|$ increases for both uphill and downhill ([80 compared with 97 fs for 575-560 compared with 590-560] and [47 compared with 51 fs for [575-590 compared with 560-590]), (iii) the absolute value of the uphill rise times is greater than the downhill rise times (80/97 fs for 575-560/590-560 compared with 25/47/51

fs for 560-575/575-590/560-590) and iv) the absolute value of the rise times vary considerably for different probe wavelengths with the same wavelength difference (80/25/47 575-560/560-575/575-590). It is noted that while the same wavelength difference for different spectral ranges does *not* equate to an equal energy difference the discrepancy is less than 5 % of the total energy difference.

It is not immediately obvious from the fit parameters but visual comparison of the two-colour integrated intensities (excluding 590-575) compared to the one-colour curves, reveals that after the initial slower rise the two-colour curves appear to asymptote to a maximum. This asymptotic behaviour is taken into account in the analytical fits by the exponential rise function that asymptotes to the corresponding pre-exponential factor A_i . The 590-575 intensity profile has a unique signal response with respect to the other one- or two-colour experiments. The signal is dominated by a coherent artifact feature followed by a weak long lived decay with pronounced modulation (quantum beat).

The spectral features of the two-colour transient grating spectra with respect to the corresponding one-colour signal vary considerably (Fig. 4.6). To quantify the spectral properties a time-integrated transient grating spectrum was calculated by summing over population times $t_{23} > 130$ fs for each experiment (not shown). These spectra were fitted using Voigt profile(s) to describe the lineshape. The one-colour time-integrated spectra were also fitted for comparison and the nomenclature for the signal channels maintained, e.g., when the third pulse is 575 nm there are three signal channels 580, 586 and 593 nm. The width of the peaks (in nanometres) was kept constant across all signal channel(s) for a given spectral lineshape fit.

The results of the fit to the integrated-intensity spectra are listed in Table

4.4. Also included in Table 4.4, as a reference, are unperturbed transition wavelengths calculated for a simple harmonic oscillator with an absorption maximum 567 nm and a single vibrational mode with frequency 207.5 cm⁻¹. The spectral width of the one-colour signal channel(s) at different laser-wavelengths follow the order $\Delta\nu_{575} > \Delta\nu_{560} > \Delta\nu_{590}$. This is attribute to the different spectral widths of the applied laser pulses which follow the same order. This is important because it will be used to explain most of the measured variation of the two-colour spectra.

The downhill 560-575 spectra compared to the corresponding one-colour 575-575 spectrum shows a marked blue-shift of the 580 and 586 nm signal channels (578.8 < 580.5 nm and 586.6 < 586.9 nm), spectral narrowing of each signal channel (213 < 259 cm⁻¹) and a significantly smaller contribution from the 593 nm signal channel (5 < 24%). The downhill 575-590 compared to one-colour 590-590 spectra exhibit a blue-shift for all three signal channels (593.8 < 595.0, 599.7 < 600.5 and 607.0 < 607.6 nm), a broadening of the spectral width of each signal channel (208 > 182 cm⁻¹) and a

Table 4.4: Results of analytical fits of Voigt profiles to the time-integrated one- and two-colour spectra. See text for details.

Para ^a	$\lambda_{1,2} \setminus \lambda_3$	560	575			590		
λ_c (nm)	560	560.4	578.8	586.6	593.5	594.5	600.6	607.5
sw (cm ⁻¹)		219	219	213	208	201	197	193
% Area		99.2	50.9	44.3	4.8	69.1	26.0	4.9
λ_c (nm)	575	560.4	580.5	586.9	593.3	593.8	599.7	607.0
sw (cm ⁻¹)		227	265	259	253	212	208	203
% Area		95.7	41.7	34.1	24.2	57.8	34.8	7.4
λ_c (nm)	590	558.1	579.0	586.5	593.2	595.0	600.5	607.6
sw (cm ⁻¹)		208	256	250	244	186	182	178
% Area		96.6	15.4	29.9	54.7	65.1	32.8	2.1
λ_c (nm)	UNP ^b	560.4	580.7	587.7	595.0	595.0	602.4	610.1

^a Voigt profiles were used to fit the data.

^b Proposed unperturbed transitions calculated assuming absorption maximum 567 nm and a single vibrational frequency of 207.5 cm⁻¹.

small increase in the contribution from the 607 nm signal channel ($7 > 2\%$). The downhill 560-590 compared to the one-colour 590-590 spectrum only significantly blue-shifts in the 595 nm signal channel ($594.5 < 595.0$ nm), the spectral width is broadened ($197 > 182$ cm^{-1}) and the contribution of the 607 nm signal channel is slightly increased ($5 > 2\%$). It is noted that the spectral width of the signal channel(s) for each downhill time-integrated spectrum follows the same laser-wavelength dependence as the one-colour spectra, i.e., $\Delta\nu_{575} > \Delta\nu_{560} > \Delta\nu_{590}$. Furthermore, the contributions of the far red-shifted signal channel for a given probe wavelength also follows the same trend, i.e., for $\lambda_3 = 590$ nm the % Area contributions of signal channel 607 nm are $7.4 > 4.9 > 2.1\%$ for $\lambda_{1,2} = 575, 560$ and 590 nm; and when $\lambda_3 = 575$ the % Areas of channel 593 nm are $24.2 > 4.8$ for $\lambda_{1,2} = 575, 560$ nm. Finally, all of the centre wavelengths of the downhill and corresponding one-colour signal channels are blue-shifted from the unperturbed values (Table 4.4) with the exception of the 595 nm signal channel for the one-colour 590-590 experiment.

The uphill 575-560 spectrum compared to the 560-560 result has the same centre wavelength (560.4 nm) though the spectral width is broader ($227 > 218$ cm^{-1}). By contrast, the uphill 590-560 spectrum is significantly blue-shifted relative to the 560-560 spectrum ($558.1 < 560.4$ nm) and spectrally narrower ($208 < 219$ cm^{-1}). Again the spectral width is pump-laser-wavelength dependent, i.e., the spectral width varies as $575 - 560 > 560 - 560 > 590 - 560$ experiments. It is noted that the contribution of the 560 nm signal channel to the 560 nm probe results is not 100% because other insignificant (contribute $< 5\%$) spectrally shifted signals were included in the fit but were neglected for clarity. The uphill 590-575 spectrum is blue-shifted from the 575-575 result ($579.0 < 580.5$, $586.5 < 586.9$

and $593.2 < 593.3$ nm), spectrally narrower ($250 < 259$ cm^{-1}) and the contributions of the signal channels is reversed, i.e., the contributions decrease with decreasing channel wavelength whereas in the one-colour case the blue channel is maximum and decreases with increasing channel wavelength. It is noted that it is difficult to see the blue signal channel response in Figure 4.6 because the coherent artifact around time zero (which is neglected here) suppresses the longer time response of the system.

4.2.3 Laser-Wavelength Dependence and Effect of Rapid Intraband Population Relaxation

To understand the laser-wavelength dependence of the transient grating spectra it is necessary to take into account the signal response to both the effect of rapid intraband population relaxation and homogeneous dephasing. The strongest evidence for the presence of intraband population relaxation is the absence of any signal centred near the central frequency of the laser pulses in the 575 nm and 590 nm experiments (Figs. 4.2, 4.3 and 4.6). The absence of the signal near the centre frequency of the laser pulses at population times greater than the pulse overlap region ($t_{23} > 130$ fs) can only result from any levels near these wavelengths undergoing rapid depopulation within the laser pulse width (approximately 90 fs FWHM). The question arises, though, as to why similar behaviour was not measured at 560 nm. To illustrate the laser-wavelength dependence of the signal, separate energy level diagrams with the three experimental laser wavelengths overlaid are presented (Fig. 4.8). The energy level diagrams were created assuming a Stokes shift 2λ of 800 cm^{-1} , an absorption maximum of 567 nm and a single vibrational mode of frequency 200 cm^{-1} . Here $1/T_{1\nu}$ refers to the rapid intraband population relaxation.

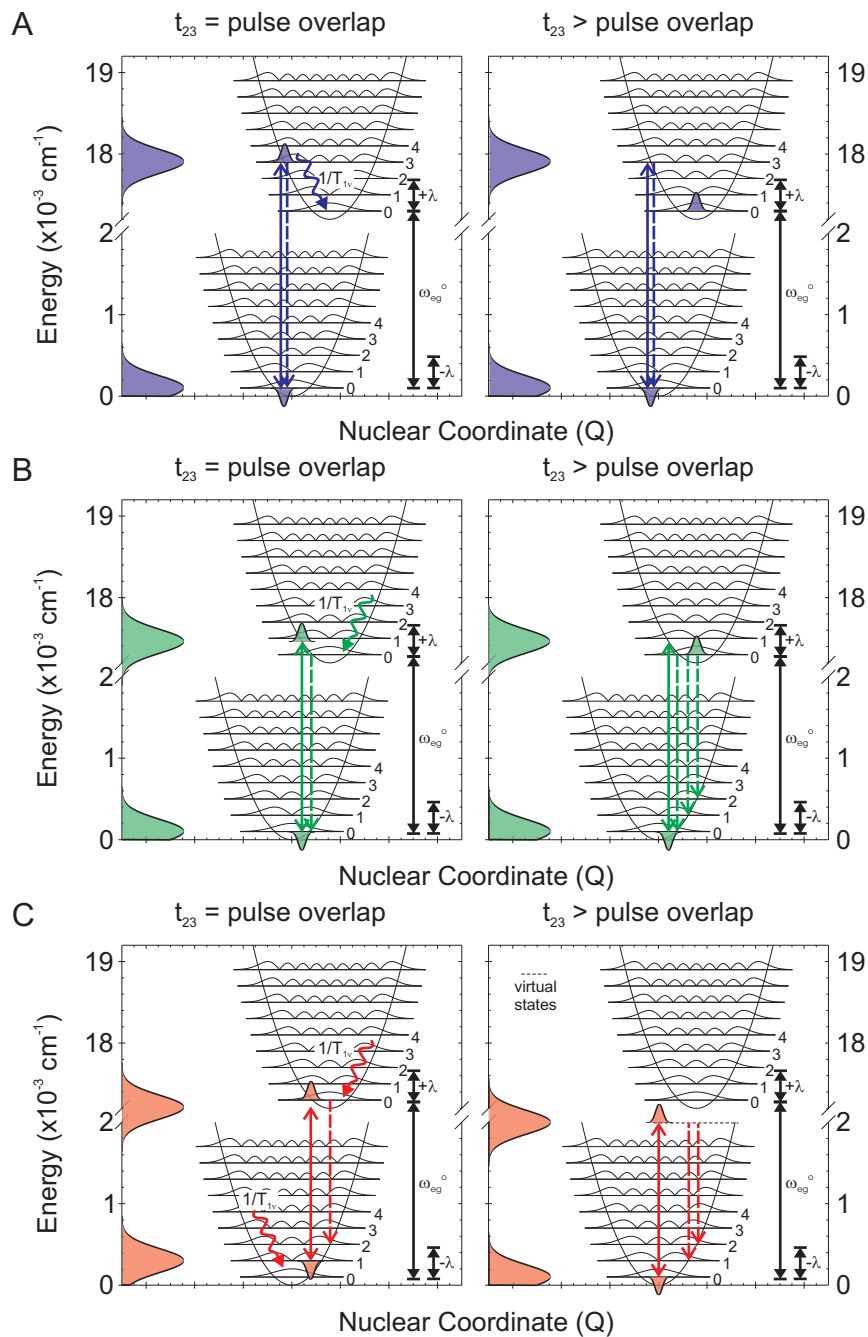


Figure 4.8: Energy level diagrams for a simple harmonic oscillator with absorption maximum of 567 nm coupled to a single vibrational mode of 200 cm^{-1} . Solid double headed arrows indicate energy of (a) 560, (b) 575 and (c) 590 nm laser pulses. Dashed lines indicate proposed transitions for the emission of the scattered signals.

In the 560 nm case the laser pulses interact with the lowest vibrational level of the ground state and the higher energy ν_3 vibrational level of the excited state (Fig. 4.8). For simplicity it is assumed there is no initial excitation of thermally populated vibrational levels of the ground state. After the initial excitation the excited state wavepacket relaxes via the rapid intraband population relaxation to the ν_0 vibrational level that resides outside the accessible energy levels for the 560 nm laser pulses. In a transient grating experiment, however, the signal response is sensitive to contributions from both the excited state wavepacket and the ground state hole. Thus, the signal response at population times greater than the pulse overlap region $t_{23} > 130$ fs (assuming $1/T_{1\nu}$ is pulse width-limited) is indicative of the ground state hole dynamics since the excited state wavepacket is no longer able to be coupled by the 560 nm laser pulses. The problem of how the signal, which is stimulated emission, is generated can be explained by considering that the scattered signal is emitted at a time t approximately equal to the coherence time t_{12} which in the transient grating case is zero. Moreover, the assertion that the first and third pulses only generate coherent states and not a population state is conceptual and not strictly true as evidenced by the population actually being dependent on t_{13} rather than t_{23} (see section 5.5.2 on page 125) [11]. Thus, the signal is instantaneously emitted from the ν_3 level after the third pulse is applied.

The absence of any significant spectral shift from the centre laser frequency in the transient grating spectrum can be explained by the 560 nm laser pulses being centred on the ν_3 level. It is interesting to note that during the pulse overlap region $t_{23} < 130$ fs there is a weak signal centred around the ν_2 approximately 17637 cm^{-1} (567 nm) vibrational level that does not persist for longer times (Figs. 4.2 and 4.8). This provides

direct evidence for the presence of the rapid relaxation of the excited state wavepacket. In this scenario, a more thorough modelling process would have included a population relaxation component that removed the contribution of response functions R_1 and R_2 that describe the system with an excited state population during the second time period t_2 (see section 2.3 on page 32). Developing a more rigorous theoretical model of this type would have required switching to a wavepacket based formalism, a process that was beyond the scope of this thesis.

The 575 nm case presents a different set of signal responses to the 560 nm experiment, since the 575 nm laser pulses are capable of coupling together any population residing in the lowest energy vibrational levels of the excited and ground states. To begin, for simplicity, the following will focus on the highest energy signal channel (580 nm). The effect of the rapid intraband population relaxation $1/T_{1\nu}$ is to shift the transient grating spectrum to longer wavelengths for population times greater than the pulse overlap region $t_{23} > 130$ fs (Fig. 4.8). Specifically, the 575 nm laser pulses are centred between the vibrational levels $\nu_{0,1}$ of the excited state (Fig. 4.8) and the spectra at short population times $t_{23} < 130$ fs reflect this. As an aside, the short population time signal is blue-shifted relative to the longer time signal; however, it is not centred at 575 nm which is proposed to be indicative of the extremely short ($T_{1\nu} \ll 94$ fs) population time of vibrational levels $\nu_{1,2}$, i.e., the short time spectrum is already shifted to longer wavelengths as population relaxation occurs during the leading edge of the 90 fs laser pulses such that at the peak much of the signal is already being generated from the ν_0 level. At longer population times t_{23} the signal is centred around ω_{eg}^o approximately 17212 cm^{-1} (581 nm) where it persists on the measured timescale.

The signal response for the remaining two signal channels of the 575 nm experiment (586 and 593 nm) have been modelled as coherent Raman scattering. Signals comprising both degenerate four wave mixing (DFWM) and coherent Raman scattering (both Stokes and anti-Stokes) have been reported for iodine vapour [48, 49]. The major difference between the rhodamine 101 spectra measured at 575 nm and the spectrum reported for iodine vapour is only a coherent Stokes Raman scattering (CSRS) signal was detected whereas the reported signal also comprises a coherent anti-Stokes Raman scattering (CARS) component.

The absence of a CARS signal in the rhodamine 101 transient grating spectra is attributed to the effect of the rapid intraband population relaxation. Consider the time evolution diagrams for the CSRS and CARS processes (Fig. 4.9), the CSRS signal is generated from the lowest vibrational level of the excited state after a delay time t_{23} whereas the CARS signal is emitted from a higher lying vibrational level. In the case of rhodamine 101 where the rapid intraband population relaxation leaves the excited state population in the lowest lying vibrational level only the CSRS processes is possible. Thus no CARS signal was measured for rhodamine 101. It is noted that there are more diagrams for both the CSRS and CARS processes; however, for simplicity diagrams that involve excitation from thermally populated higher lying ground state vibrational levels were neglected.

The 590 nm transient grating spectra presents a different set of signal responses from both the 575 and the 560 nm cases. The high energy signal channel 595 nm was modelled using only the response functions R_3 and R_4 that describe the system in the ground state during the population period t_2 . In contrast to the 560 nm case, where the initial contribution from the excited state is significant, the 596 nm signal channel is only weakly cou-

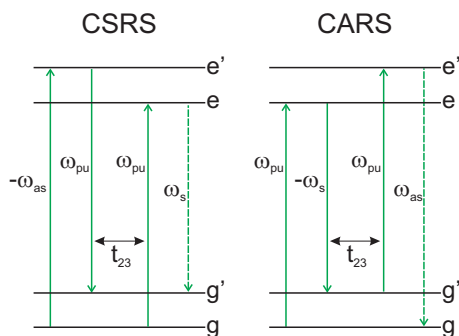


Figure 4.9: Time evolution diagrams describing femtosecond coherent Stoke Raman scattering (CSRS) and coherent anti-Stoke Raman scattering (CARS) processes.

pled to the excited state because it must involve excitation from thermally populated high lying vibrational levels of the ground state (Fig. 4.8). Thus the processes described in the first panel ($t_{23} = \text{pulse overlap}$) of Figure 4.8 for the 590 nm experiment were neglected. The choice to only include ground state populations is further supported by the higher quality of the fit compared to the result obtained with all four response functions (not shown). It is noted that there is a significant phase shift of the quantum beat modulation relative to the coherent artifact peak for the two different fits.

The signal response from the remaining two signal channels 601 and 607 nm is again attributed to coherent Raman scattering processes. The CSRS signal channels compared to the DFWM channel (595 nm) are spectrally narrower and are weaker. The smaller spectral width was initially attributed to limitations in resolving the different signal channels during the analytical fit of the spectra. Whilst it is believed that this is, in part, the case the theoretical fits follow the trend where the calculated CSRS signals were narrower than the calculated degenerate four wave mixing (DFWM). The photophysics underlying this trend are not well understood; however, it

would seem to be a result of not being resonant with the excited state as this narrowing was not observed in the 575 nm experiment. The decreasing contribution of the signal channels as the red-shift increases is attributed to the smaller spectral width of the 590 nm laser pulses compared to the 575 nm laser pulses. This can be understood by considering the spectral overlap of the laser pulses with the underlying vibronic structure (Fig. 4.8). The initial laser pulses interact and prepare higher lying vibrational levels to generate the CSRS signal response. If the laser spectral width is broad then a greater number of levels can be coupled or, as the case is here, the coupling to far detuned levels is greater.

Separation of Ground and Excited State Dynamics

One of the more exciting applications of the spectrally resolved technique is the ability to separate ground- and excited-state molecular dynamics [50]. When a molecule undergoes impulsive excitation, i.e., the pulse duration is shorter than a vibrational period, a nuclear wavepacket is created in the excited state and a hole created in the ground state. Using sufficiently broad spectrum laser pulses and solvent/solute systems showing a large reorganisation energy (Stokes shift) it is possible to simultaneously interrogate both the particle and hole dynamics. Immediately after excitation the centre frequency of the hole and the particle spectra will be equal according to the Frank-Condon principle. As intermolecular dynamics (solvation) and chromophore intramolecular nuclear dynamics proceed, the frequencies of the two components shift to their equilibrium counterparts, i.e., steady-state absorption and fluorescence spectra, respectively (Fig. 4.10).

The experimental results measured at 575 nm roughly correspond to the scenario depicted in Figure 4.10. Figure 4.5 shows the centre frequency

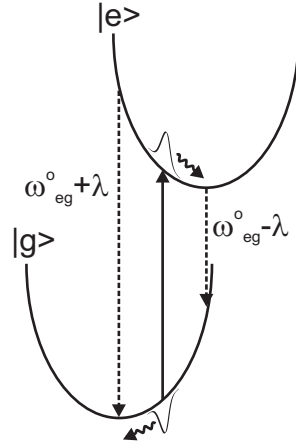


Figure 4.10: Schematic representation of the transient grating experiment and the dynamic Stokes shift of the particle and hole wavepackets in the spectral diffusion limit. For the excitation wavelength (solid arrow) $\omega_L < \omega_{eg}^o + \lambda$, where ω_L is the laser frequency, the particle will show a red shift towards the fluorescence maximum $\omega_{eg}^o - \lambda$, and the hole makes a blue shift towards the absorption maximum $\omega_{eg}^o + \lambda$. Adapted from [19].

curves for 580 and 593 nm signal channels of the 575 nm experimental wavelength spectra. The centre frequency traces show marked differences in their dynamics. The 580 nm signal channel, corresponding to ω_{eg}^o transition frequency, shows a significant time-dependent blue shift. Thus this signal is assigned to represent the hole dynamics. Conversely, the 593 nm signal channel, closely corresponding to the fluorescence maximum, undergoes a marked time-dependent red shift and is assigned to the particle dynamics. Using these assignments it is now possible to track the ground-state and excited-state dynamics. The results of least squares fitting (Table 4.2) show the relaxation times for the two overdamped Brownian oscillators vary significantly for the hole dynamics compared to the particle. The hole in the ground state relaxes with two decay times approximately 67 fs and 1.2 ps while the much slower particle in the excited state relaxes in approximately 340 fs and 5.8 ps. The faster relaxation of the ground state hole is in good

agreement with previous studies of laser dyes dissolved in methanol [50].

Two-Colour Discussion-Underlying Physical Processes

A preliminary theoretical study of two-colour transient grating experiments reported by Kwak *et al.* shows that the peak of the two-colour integrated intensity curves shift with both the wavelength difference between $\lambda_{1,2}$ and λ_3 and the relaxation rates Λ_i of the system (Fig. 4.11) [41]. Specifically, as the wavelength difference $\Delta\lambda = |\lambda_{1,2} - \lambda_3|$ increases the rise time increases and shifts the delay time at which the intensity peaks. As $\Delta\lambda$ is further increased to near the Stokes shift 2λ of the system the intensity appears not to reach a peak but to asymptote to a maximum value. When the decay rate of a fast overdamped mode is increased the intensity curve peak is again shifted to longer delay times and the coherence artifact is broadened. The short time decay for rhodamine 101 is assumed not to change in these measurements and thus this last effect is included for completeness. It is noted that the theoretical model used by Kwak *et al.* to qualitatively describe the signal response to the photophysical processes does *not* provide for a pump pulse that is detuned from the absorption maximum and as such could *not* be used to fit the measured rhodamine 101 data. Another limitation of the theory is that it does *not* include contributions from intramolecular vibrational motion (underdamped Brownian oscillators) and was only used to describe downhill intensity curves. Nonetheless, it does provide a good qualitative description of the measured rhodamine 101 two-colour transient grating integrated intensity curves with the exception of the 590-575 case (Fig. 4.7).

The following provides a brief description of the underlying photophysical processes that lead to the difference between one- and two-colour signal

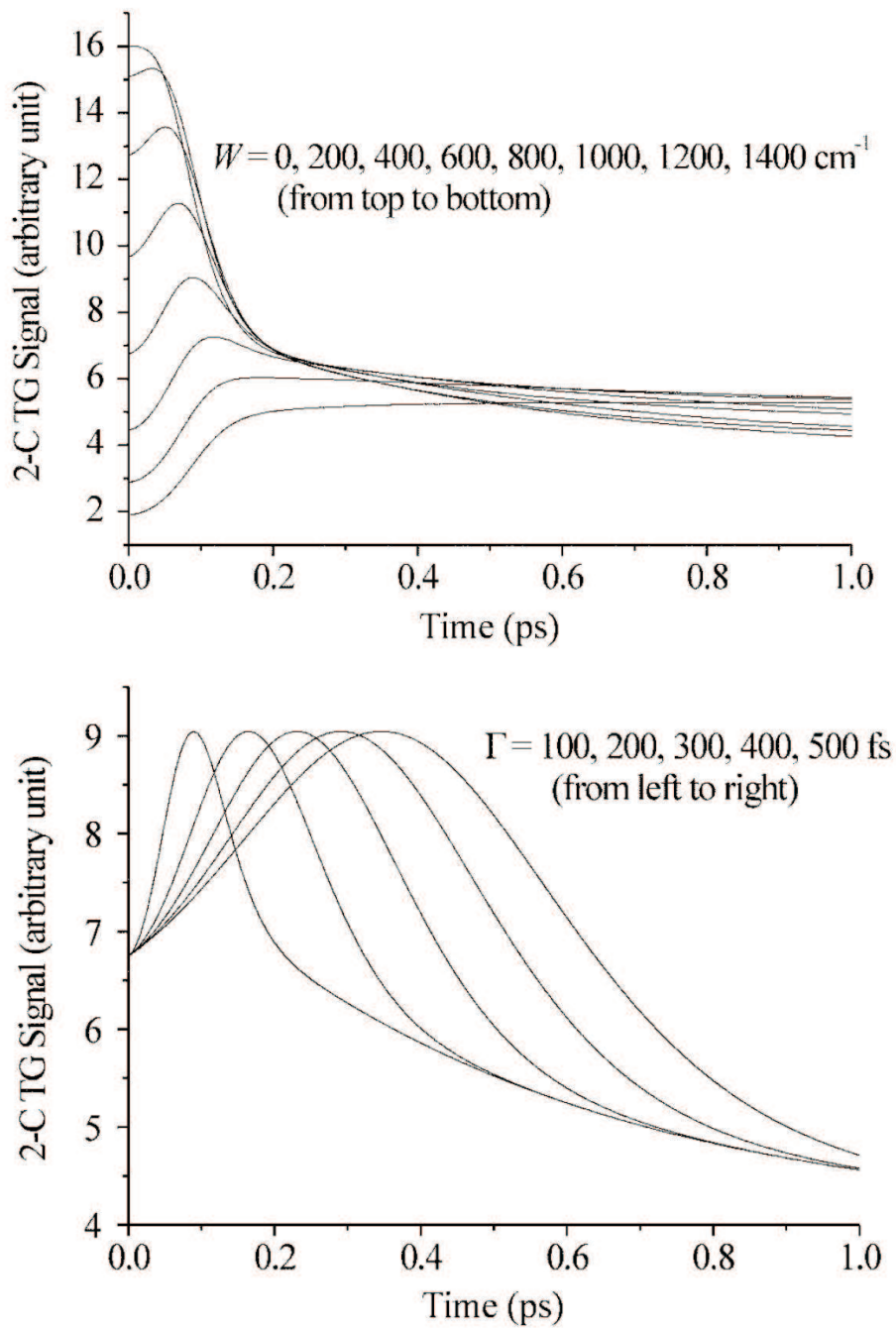


Figure 4.11: Two-colour transient grating integrated intensity curves (a) as a function of laser detuning (W) of the probe pulse for a system with Stokes shift 1200 cm^{-1} , overdamped modes 100 fs and 1 ps, pumped on resonance. Note positive values of W are red-detuned from the pump. (b) Dependence on the dephasing time (Γ) of the first overdamped mode for a fixed detuning $W = 800 \text{ cm}^{-1}$. Note data reproduced from reference [41].

response. One-colour transient grating signals have the same doorway and window states and thus the decay measures how rapidly the initially created wavepacket moves away from the doorway state and the signal decays monotonically. by contrast, because of the difference between the doorway and window states in two-colour transient grating experiments the signal can initially rise as the propagating wavepacket passes into the window state before moving out again [41]. In the case when the window state is tuned near the Stokes shift the excited state wavepacket and ground state hole no longer move out of the window state and the signal asymptotes to a maximum value. In the description provided by Kwak *et al.* chromophore-solvent relaxation processes (solvation) provide the mechanism for propagating the wavepacket/hole from the doorway to the window state.

The integrated intensity curves for rhodamine 101 (excluding 590-575) are in good qualitative agreement with the model proposed by Kwak *et al.*. Visual inspection shows that the one-colour intensity curves decay monotonically after excitation while the two-colour curves show an initial rise resulting in a delayed intensity peak followed by a slower decay on the measured timescale. The results of the analytical fit to the data also follow the trend where the rise time increases with increasing wavelength difference $\Delta\lambda$. The longer rise time for the uphill compared to the downhill intensity curves is also in agreement with the experimental results reported by Kwak *et al.*. It is proposed that the 590-575 case is also consistent with the other two-colour results; however, the expected integrated intensity curve is masked by the dominant coherent artifact component of the signal.

While the above description is sufficient to qualitatively describe the integrated intensity signal response it does not contain enough detail to explain the spectral features of the spectrally resolved signal. To account for

the spectral features of the two-colour spectra the photophysical processes discussed for the one-colour results and the difference in the spectral width of the applied laser pulses need to be considered. Moreover, the possibility of light shifts induced by the AC-Stark effect will be introduced that were not considered above.

The spectral width of each signal channel and the contribution of far-red-shifted signal channels to the total time-integrated spectrum follow the spectral width of laser pulses with the exception of the 590-575 experiment. Specifically, in each row or column of Table 4.4 the spectral widths follow the trend $\Delta\nu_{575} > \Delta\nu_{560} > \Delta\nu_{590}$ where the subscript denotes the wavelength of the probe for rows and the pump for columns. Similarly, this trend is followed for the % Area contribution of the far-red-shifted channels in the results probed at 575 or 590 nm (excluding 590-575). This can be understood by considering the spectral overlap of the laser pulses with the underlying vibronic structure (Fig. 4.12). The initial laser pulses interact and prepare higher lying vibrational levels to generate the CSRS signal response. If the laser spectral width is broad then a greater number of levels can be coupled or, as the case is here, the coupling to far detuned levels is greater.

To explain the wavelength dependence of the light shifts of transition wavelengths for different laser wavelengths and signal channel wavelengths for the same laser wavelength the AC-Stark effect is invoked. To semi-quantitatively describe the AC-Stark effect the Cohen-Tannoudji approach was used for the weak intensity limit $\Omega \ll 1/T_2$, where Ω and $1/T_2$ are the Rabi frequency and total dephasing rate, respectively [51]. The light shift

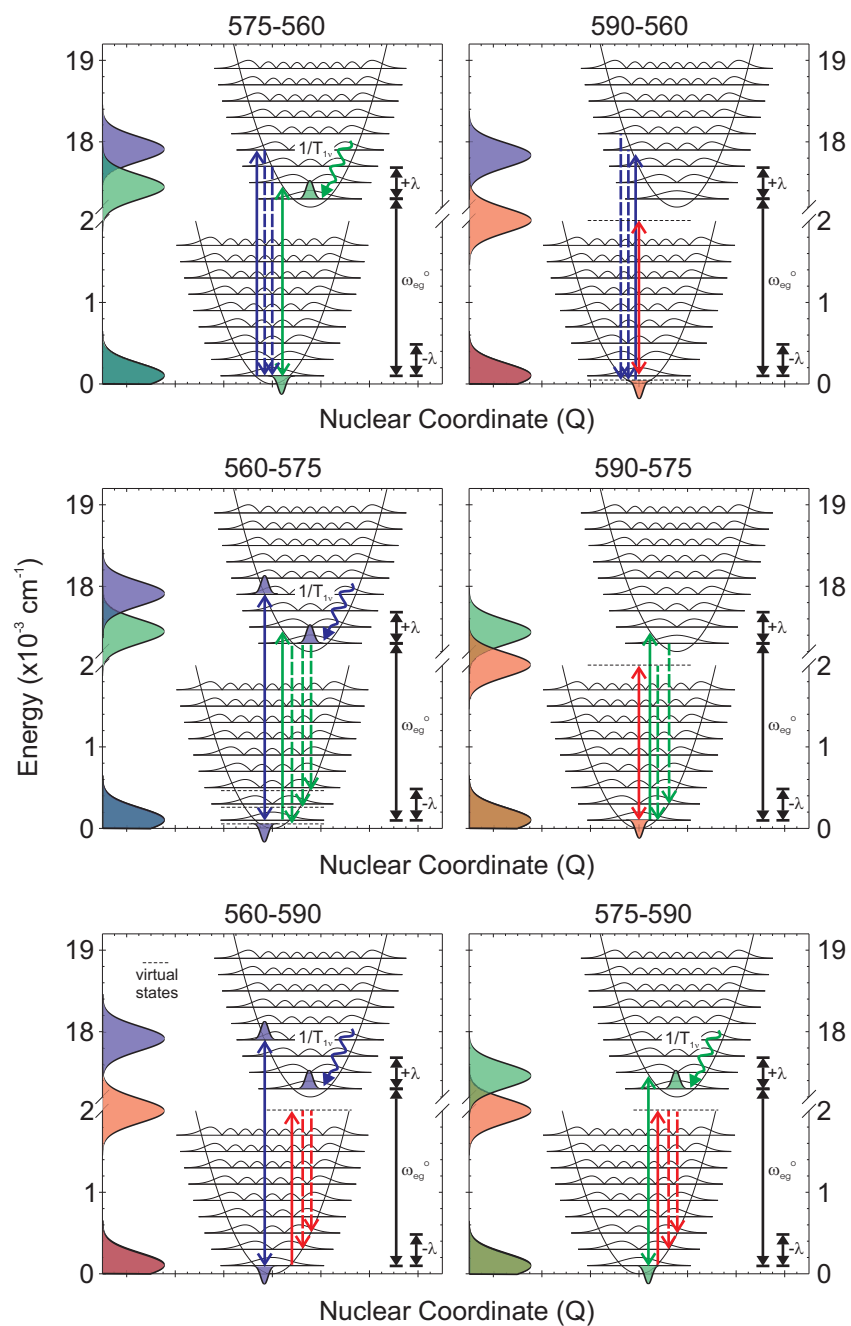


Figure 4.12: Energy level diagrams for a simple harmonic oscillator with absorption maximum of 567 nm coupled to a single vibrational mode of 200 cm^{-1} . Solid double headed arrows indicate energy of first two laser pulses and solid single headed arrows indicate energy of the third laser pulse. Dashed lines indicate proposed transitions for the emission of the scattered signals for six different two-colour transient grating experiments as indicated.

$\Delta E'$ and broadening of the ground state Γ' are described as follows:

$$\omega_L = \omega_0 \Rightarrow \begin{cases} \Delta E' = 0 \\ \Gamma' = \Gamma \left(\frac{\Omega}{\Gamma} \right)^2 \ll \Gamma \end{cases} \quad (4.9)$$

and

$$|\omega_L - \omega_0| \gg \Gamma \Rightarrow \begin{cases} \Delta E' = \frac{(\Omega/2)^2}{\omega_L - \omega_0} \\ \Gamma' = \Gamma \left(\frac{\Omega/2}{\omega_L - \omega_0} \right)^2, \end{cases} \quad (4.10)$$

where ω_L is the laser frequency and ω_0 is the transition frequency. Note the broadening produced by the AC-Stark effect in this limit is small compared to the linewidth corresponding to $1/T_2$.

Figure 4.13 shows the laser-wavelength-dependent light shifts and broadening for a system with a Rabi frequency of 0.04 fs^{-1} , total dephasing rate of 0.10 fs^{-1} and transitions at 580.7, 587.7 and 595.0 nm. When the laser wavelength is equal to the transition wavelength there are no light shifts and the ground state broadening is at a maximum (Fig. 4.13). As the laser wavelength is detuned from the transition energy the magnitude of the light shift increases and the broadening decreases. Finally the light shift peaks and then begins to gradually asymptote to the unperturbed transition wavelength. It is important to note that the magnitude of the broadening as a function of detuning decreases significantly faster than the light shift. It is noted that a Rabi frequency of 0.04 fs^{-1} using femtosecond pulses of around $160 \text{ mJ/cm}^2/\text{pulse}$ is in reasonable agreement with those calculated for another rhodamine 101 (*not* perchlorate salt) in ethanol that reported Rabi frequency of 0.0052 fs^{-1} using $\Omega = 2(\mu_{ba}E)T_2/\hbar$, nanosecond pulses and a fluence of around $1.4 \text{ mJ/cm}^2/\text{pulse}$ [52].

Figure 4.13 only takes into account an interaction with a single laser

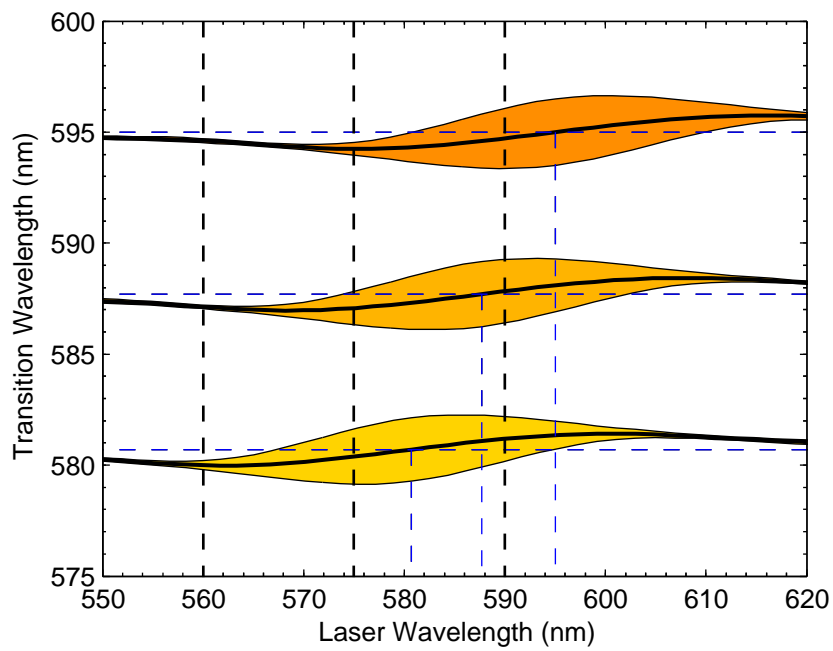


Figure 4.13: Calculated AC-Stark induced light shifts and broadening for three transition of wavelengths 580.7, 587.7 and 595.0 nm. Light shifts shown as thick black line and the broadening overlaid as shaded area. Transition wavelengths indicated as dashed blue lines and position of three laser wavelengths 560, 575 and 590 nm shown as thick dashed black lines. See text for details.

pulse while our experiment involves three pulses impinging on the system. In order to take account of the additional laser interactions, a final light shift was calculated by feeding the shifted transition wavelength from one laser interaction into the next and so on until three laser interactions had occurred (Table. 4.5). Moreover, the colour of the first two laser interactions was changed relative to the third and a series of unperturbed transition energies (calculated by assuming an absorption maximum of 567 nm and a vibrational frequency of 207.5 cm^{-1}) were used to build-up a semi-quantitative final transition energy for each of the experiments (Table. 4.5).

Table 4.5: Experimental transition wavelengths for one- and two-colour transient grating spectra (reproduced from Table 4.2) compared to those calculated taking into account the AC-Stark effect. See text for details.

$\lambda_{1,2} \setminus \lambda_3$		560	575			590		
560	Exp	560.4	578.8	586.6	593.5	594.5	600.6	607.5
		0.0	-1.9	-1.1	-1.5	-0.5	-1.9	-2.6
	Theory	560.4	579.0	586.0	593.5	594.0	601.2	608.8
		0.0	-1.6	-1.8	-1.5	-1.0	-1.2	-1.3
575	Exp	560.4	580.5	586.9	593.3	593.8	599.7	607.0
		0.0	-0.2	-0.8	-1.7	-1.2	-2.8	-3.0
	Theory	561.6	579.8	585.9	592.8	593.3	600.5	608.4
		1.1	-0.9	-1.8	-2.3	-1.7	-1.9	-1.7
590	Exp	558.1	579.0	586.5	593.2	595.0	600.5	607.6
		-2.3	-1.6	-1.3	-1.8	0.0	-2.0	-2.5
	Theory	561.3	581.3	587.3	593.7	594.2	600.6	607.8
		0.9	0.6	-0.5	-1.3	-0.8	-1.8	-2.3
UNP ^a		560.4	580.7	587.7	595.0	595.0	602.4	610.1

^a Proposed unperturbed transitions calculated assuming absorption maximum 567 nm and single vibrational frequency of 207.5 cm^{-1} .

Table 4.5 shows the centre wavelengths obtained from the analytical to the time-integrated spectra and an estimate of the AC-Stark shifted transition wavelengths. Also included in Table 4.5 are the differences between the experimental/calculated results and the unperturbed levels. Whilst the calculated and experimental results differ significantly this basic model does

describe some of the light shift trends. Consider the light shifts of the 580, 586, 593 nm signal channels of the 575-575 data. The calculated data follows the trend of increasing the blue-shift as the wavelength of the signal channel increases, albeit with a poor absolute correspondence. Now consider the light shifts for 560-575 compared to the 575-575 results. Here the calculated light shifts predict the blue-shift of the 580 nm and small red-shift of the 593 nm signal channels. There is a small difference for the 586 signal channel though neither the experiment nor theory shift significantly. It is noted that it is only after three laser interactions and associated light shifts that the 593 nm signal channel *red-shifts* for 560-575 the compared 575-575. The light shift trends for the one- and two-colour transition wavelength probed at 590 nm are also reasonably well described by the calculated data. Specifically, the size of the 595 nm signal channel light shifts follow the order $\Delta\lambda_{575} > \Delta\lambda_{560} > \Delta\lambda_{590}$ where the subscript denotes the pump wavelength. It also correctly predicts that all of the transitions are blue-shifted from the proposed unperturbed levels in the 590 nm probed spectra. It is proposed that these results provide evidence that AC-Stark effects are an important consideration when performing photon echo/transient grating experiments with high energy pulses. Moreover, It is proposed that the AC-Stark effect is responsible for the separate signal channels not being separated by one vibrational quantum.

The uphill spectra present another set of problems when considering the spectral light shifts. The results of Table 4.5 for the 560-560 results correctly predict that upon resonant excitation the level is not shifted. The calculated light shifts for the uphill spectra with a 560 nm probe, on the other hand, predict that the transition wavelengths would be red-shifted as the pump wavelength was increased. This does *not* agree with the experimental results

where for 575 nm excitation there was no shift and for 590 nm excitation there was a large blue-shift of 2.3 nm. This discrepancy is also evident in the 580 nm signal channel of the 590-575 spectrum. The uphill process is complex and requires the development of a comprehensive theoretical model in unison with further experimental studies to further our understanding. The current level of theoretical development to describe the uphill spectra is in its infancy and with three laser interactions it is difficult to predict what features an uphill spectra should have.

4.3 Summary

In this chapter the characteristics of a spectrally resolved transient grating signal and the underlying photophysical processes for a relatively *simple* system were investigated. The term simple here is used lightly as it has been shown that the signal response even for a one-colour experiment can be complex. It has been shown that the spectrally resolved signal can greatly facilitate the interpretation of transient grating signals. Here the presence of two-types of signal response may well have gone undetected had the investigator had access to only the integrated intensity data. It was shown that: (i) Rhodamine 101 in methanol undergoes a rapid (pulse width-limited) intra-band population relaxation, three different dephasing processes with relaxation times of < 94 fs, 3-5 ps and $\gg 6$ ps and has a vibrational mode with a characteristic frequency of approximately 208 cm^{-1} and a relaxation time of approximately 240 fs (ii) The spectrally resolved signal with careful selection of a broad probe wavelength can be used to separate the ground and excited state relaxation times. (iii) Two-colour experiments can be used to probe the underlying rapid relaxation processes of a system. (iv) It is important to consider AC-Stark effects when performing photon echo/transient grat-

ing experiments, albeit both require a concerted theoretical effort to extract physically significant results.

Chapter 5

Spectrally-Resolved Photon Echoes of Heme-Based Biological Molecules

Some of this work has appeared in the following publications:

1. L.V. Dao, C.N. Lincoln, R.M. Lowe and P. Hannaford, *Femtosecond Laser Spectroscopy*, ch. 8, "Spectrally Resolved Two-Colour Femtosecond Photon Echoes," pp. 197-224. Springer: New York, 2005.
2. L.V. Dao, C.N. Lincoln, M.T.T. Do, P. Ecker, R.M. Lowe and P. Hannaford, "Spectrally Resolved Femtosecond 2-Colour 3-Pulse Photon Echoes: A New Spectroscopic Tool to Study Molecular Dynamics," *Australasian Physical & Engineering Sciences in Medicine* **27**(4), p. 224-229, 2004.

5.1 Introduction

In the previous Chapter Rhodamine 101 in methanol was studied to determine the intra- and inter-molecular dynamics of an *inert* system in solution. To investigate the intra- and inter-molecular dynamics of a *real* chemical system involved in a chemical reaction the photodissociation reaction of a carbonyl complex of the heme protein myoglobin (Mb) was chosen. Myoglobin and its larger cousin hemoglobin are well studied biological molecules, being the first molecules to have their crystal structure determined using X-ray diffraction techniques, which won Kendrew and Perutz the Nobel prize for chemistry in 1962 [53–57]. Since then and with the advent of pulsed laser sources many photophysical studies have been conducted on myoglobin and hemoglobin including pump-probe and transient absorption [58–70], time resolved resonance Raman [71, 72], transient grating [73–75] and two-pulse photon echo in the infrared [76–78]. More recently, having gone in a full circle, time resolved X-ray crystallography with 150 ps pulses has been applied to myoglobin and hemoglobin [79, 80]. After many years of experimental and theoretical study questions still remain about the temporal dynamics and mechanism of the photodissociation reaction. It is noted that for completeness and to emphasise the biological importance of this class of molecules that hemoglobin is also included in the background discussions.

This Chapter begins with a background discussion of the biological function and the crystal structure of myoglobin and hemoglobin, followed by the electronic and vibrational structure based on the steady-state optical properties and the two major models of the photodissociation process including the supporting experimental results for each. The experimental section is separated into two sections. The first sees the use of spectrally resolved one-colour photon echo spectroscopy to investigate the photochemical states of

myoglobin during the photodissociation reaction and the possible mechanism. The second presents the results for the application of spectrally resolved two-colour transient grating to myoglobin to provide insight into the dynamics of the initial ultrafast processes of the photodissociation reaction.

5.2 Biological Function and Crystal Structure of Heme Proteins

Before the pioneering work of Furchgott, Ignarro and Murad the primary biological function of the heme proteins myoglobin and hemoglobin was considered to be the storage and transport of oxygen, respectively [6]. Hemoglobin was also known to transport H_2CO_2 by allosteric¹ processes and to undergo a structural rearrangement to increase the efficiency of transporting oxygen. However, recent studies have shown that hemoglobin also binds nitric oxide in addition to oxygen in a cooperative effect. When nitric oxide- and oxygen-bound hemoglobin (typically a 1:3 ratio) in blood enters a region of low oxygen concentration in the body the nitric oxide is liberated which signals the blood vessel to dilate thus facilitating further blood flow into the area. Furthermore, the loss of nitric oxide also triggers the oxygen bound hemoglobin to switch from the relaxed (R) to the tense (T) state which has low affinity for oxygen-binding thus increasing the ease with which all three oxygen molecules are released at the oxygen starved site. In the case of myoglobin, it has recently been proposed that the primary function is as an allosteric nitric oxide scavenger when in the oxygen-bound state rather than the storage of oxygen itself [81]. Whilst not directly related to the

¹Used to describe some protein, especially an enzyme, in which a compound combines with a site on the protein other than the active site. This may result in a conformational change at the active site so that the normal substrate cannot bind to it. The allosteric property is useful in the regulation of enzyme activity.

phenomena studied in this Chapter, the subtle synergy between the heme proteins and the nitric oxide and oxygen ligands highlight the importance of understanding the complex relationships between (in)organic molecules, proteins and their surrounding environments, a key motivation for using photon echoes.

Because the functionality of the heme proteins is based on their ability to reversibly bind oxygen and nitric oxide, the ligation of hemoglobin and myoglobin with diatomic molecules such as O₂, NO and CO has been the focus of extensive research (see, for example, [62, 64–67, 69, 82–86]). The importance of oxygen and nitric oxide is obvious; however, since CO-binding is spectroscopically easier to observe many experiments addressing the binding kinetics of heme proteins use CO-ligated hemoglobin and myoglobin. The preference for studying MbCO arises from the quantum yield of unity² of MbCO photodissociation and the absence of a very fast rebinding component and *geminate rebinding*³, as is the case for MbO₂ and MbNO, which complicates studies of the dissociation process. As a result all of the experimental work described in this Chapter is performed using CO-bound heme proteins.

Both myoglobin and hemoglobin have a reactive prosthetic group called *heme* which is supported by a protein matrix called a *globin*. Heme is an Fe-protoporphyrin IX molecule which is an 18 membered aromatic ring with the central iron atom tightly bound to an inner ring of four nitrogen atoms. Hemoglobin contains four heme/globin groups and is considered an allosteric tetrameric protein whereas myoglobin has only a single globin with one prosthetic heme. The three-dimensional structure of the globin(s) of myoglobin

²When a photon is absorbed a photodissociation reaction occurs with a ratio of 1:1.

³Rebinding of the original ligand which after photodissociation has failed to migrate out of the protein and into solution.

and hemoglobin is surprisingly similar as each has an almost entirely different amino acid sequence. The internal environment of the folded protein is nearly exclusively non-polar, whilst the surface is predominantly polar (Fig. 5.1(a)). The heme group is bound in the non-polar pocket with the exception of two histidine residues positioned on either side of the heme plane (Fig. 5.1(b)). The non-polar nature of the heme pocket helps to protect the iron atom at the centre of the heme from oxidation to the non-binding ferric (+3) form. The nitrogen of the imidazole side chain of the proximal⁴ histidine (His93, Fig. 5.1(b)) binds at the fifth coordinate position of the binding ferrous (+2) ion, providing the only covalent link to the surrounding protein. The sixth coordinate position of the ferrous ion is the site for binding of diatomic ligands such as CO. The second distal histidine (His64, Fig. 5.1(b)) reduces the degree of CO binding and provides another mechanism for inhibiting oxidation of the iron atom to the ferric form [87].

Figures 5.1(c-d) show the heme and the proximal histidine residue (His93) for the carbon monoxide-bound myoglobin (MbCO) and the unbound form (deoxy-Mb⁵), respectively. In the bound state the central ferrous ion sits well within the plane of the porphyrin ring, whereas in the unbound state the central ferrous ion is displaced approximately 0.4 Å out of the plane of the ring toward the proximal histidine (His93). Additionally, though not easily seen in Figure 5.1(d), the inner ring of nitrogen atoms binding the central ferrous ion to the ring are also displaced out of the plane of the ring toward the proximal side by approximately 0.1 Å.

⁴**proximal** closest to the central iron atom; **distal** away from the central iron atom.

⁵Although deoxy-Mb implies oxygen-free Mb it is also used to mean carbonmonoxy-free Mb.

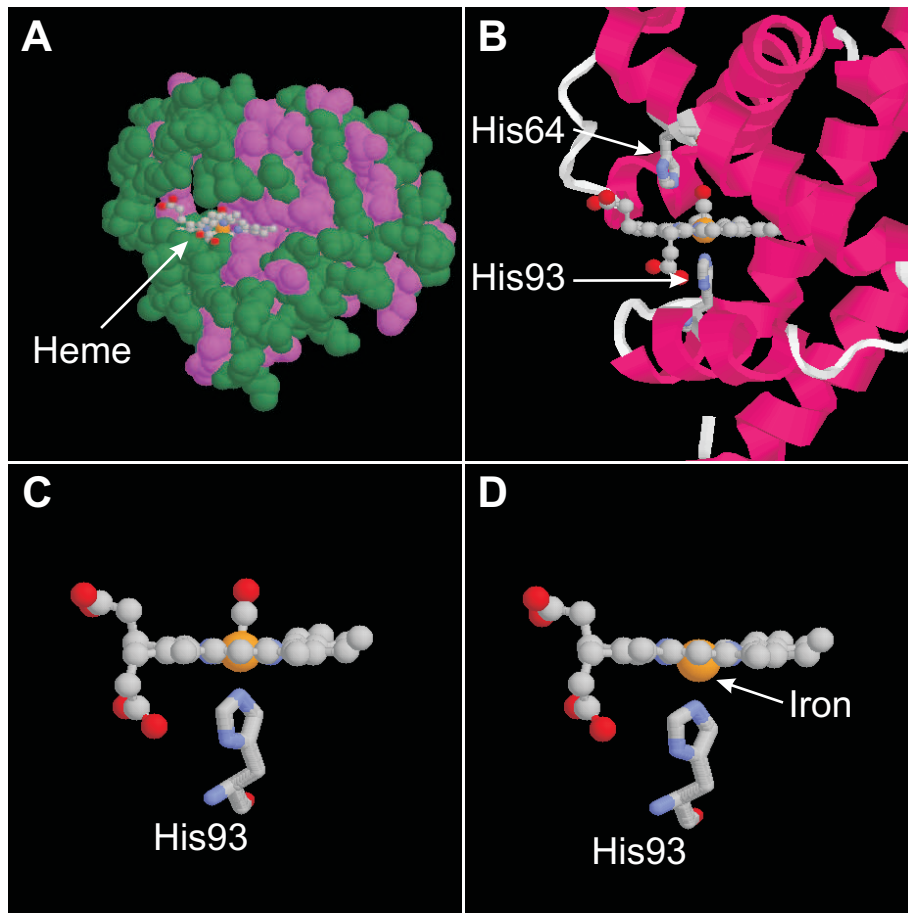


Figure 5.1: Crystal structure of myoglobin [88, 89] showing: (a) The heme pocket within the protein almost entirely non-polar (magenta) while the exterior is predominantly polar (dark green). (b) The proximal histidine (His93) bound to F-helix and distal histidine (His64) bound to the E-helix. (c) Carbon monoxide bound heme of myoglobin including His93. (d) Unbound heme of myoglobin including His93. Note how the central iron atom is significantly shifted out of the plane of the porphyrin ring compared to the bound heme. Colour code is carbon = grey, nitrogen = blue, oxygen = red and yellow = iron which is also enlarged.

5.3 Electronic and Vibrational Spectra

The absorption spectra of heme proteins are dominated by the spectral properties of the porphyrin ring. The electronic spectra and states of porphyrins in the visible and near UV are fairly well described by a simple four level system involving $\pi\pi^*$ transitions. The two highest occupied molecular orbitals (HOMOs) are assigned $a_{1u}(\pi)$ and $a_{2u}(\pi)$ and the two lowest unoccupied molecular orbitals (LUMOs) are assigned $e_g(\pi^*)$ (Fig. 5.2(b)). For molecular symmetry D_{4h} the orbitals $e_g(\pi^*)$ are strictly degenerate, whereas the $a_{1u}(\pi)$ and $a_{2u}(\pi)$ orbitals are non-degenerate. Transitions of the form $a_{1u}(\pi) \rightarrow e_g(\pi^*)$ have strong symmetric configurational symmetry in the singlet excited state and correspond to the intense Soret absorption band in the blue region of the spectrum (Fig. 5.2(a)). The weaker $a_{2u}(\pi) \rightarrow e_g(\pi^*)$ transition has an asymmetric configuration in the singlet form and corresponds to Q-band absorption in the visible spectrum (Fig. 5.2(a)). Vibronic coupling between the $(a_{1u}e_g)$ and $(a_{2u}e_g)$ singlet excited states causes splitting of the Q-band into two bands assigned $Q(\nu)$ and $Q(0)$.

In the case of heme with an iron atom substituted in the centre of the porphyrin it is necessary to consider the mixing of the d -orbitals with the π -orbitals of the porphyrin. The ferrous iron has six $3d$ valence electrons which can contribute additional absorption bands in the spectrum. It is now possible to have transitions due to $\pi\pi^*$, dd localised on the iron atom and charge transfer (CT) either $d\pi^*$ or πd transitions (Fig. 5.2(b)). However, dd and CT absorption bands are of low intensity and generally masked by $\pi\pi^*$ absorption.

Table 5.1 lists the steady-state resonance Raman modes for deoxy-Mb and MbCO. The three most spectroscopically interesting peaks are the $\nu_{\text{Fe-His}}$ ($220/\dots \text{ cm}^{-1}$), ν_7 ($671/676 \text{ cm}^{-1}$), and ν_4 ($1356/1374 \text{ cm}^{-1}$), listed

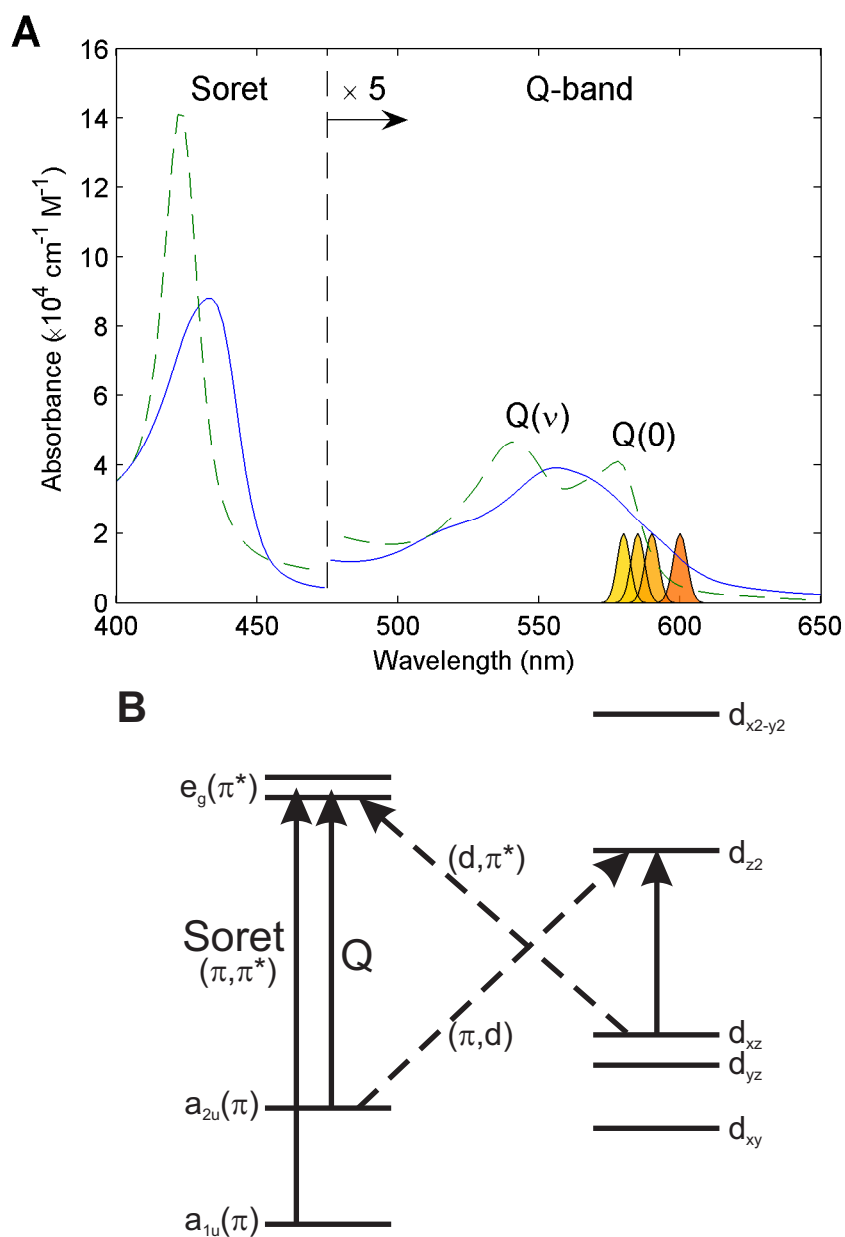


Figure 5.2: (a) Steady-state absorption spectra for Mb (solid curve) and MbCO (dashed curve). Solid Gaussian curves (coloured) indicate the spectral profile of the laser pulses used in the experiments. (b) Electronic levels for Fe-protoporphyrin IX showing the transitions corresponding to the Soret and Q-bands localised on the porphyrin ring and dd -transitions localised on the central iron atom as well as possible charge transfer transitions (dashed lines). Note the latter two are spectrally masked by the strong Q-band absorption.

Assignment	deoxy-Mb	MbCO
	144	
$\nu_{\text{Fe-His}}$	221,220,220,220	
ν_9	-,240,243,-	254,254,253,253
$-\gamma_{16},\gamma_7,-$	294,302,306,301	322,318,316,-
ν_8	343,342,344,-	348,347,345,347
$\delta(C_\beta C_c C_d)$	371,370,372,369	381,379,377,379
	-,390,-,-	-
$\delta(C_\beta C_a C_d)_4$	407,405,406,-	413,412,409,-
$\delta(C_\beta C_a C_d)_2$	436,436,437,-	436,435,434,-
$\nu_{\text{Fe-CO}}$		511,509,507,507
$\delta_{\text{Fe-CO}}$		580,575,577,-
γ_{12}	493,499,500,-	
γ_{21}	-,544,546,-	
ν_{48}	-,585,-,-	
ν_7	674,674,674,671	677,676,676,673
γ_{11}	721,718,719,-	720,718,-,-
γ_5	735,732,734,-	734,733,-,-
$-\nu_{15},\nu_{16},-$	-,758,757,-	756,753,754,752
ν_{47}	-,777,-,-	
ν_6	788,788,-,784	795,794,-,-
γ_{10}		833,830,-,-
	991,-,-,-	
	1091,-,-,-	
ν_5	1115,-,-,1119	
	1133,-,-,-	1135,-,-,1135
	1174,-,-,-	
	1225,-,-,-	1232,-,-,1232
	1317,-,-,-	
ν_4	1356,-,1356,1356	1374,-,1372,1374
	1389,-,-,-	
	1426,-,1425,-	
ν_3	1472,-,1473,-	-,-,1497,-
		1501,-,-,1502
	1524,-,1525,-	
ν_2	1564,-,1564,1564	1586,-,1583,1586
ν_{10}	1618,-,1617,1619	1620,-,-,1632

Table 5.1: Measured resonance Raman spectra for deoxy-Mb and MbCO, taken from four different sources and listed in order [90], [91], [92], [72] and quoted in wavenumbers (cm^{-1}). Note multiple assignments are only listed when the literature disagrees and (-) indicates no assignment or peak not measured. ν = stretch, δ = angle bend, γ = out-of-plane bend.

Assignment	Fe(TPP)(2-MeHIm)	Fe(TPP)(CO)(1-MeIm)
phenyl-imid,op	25	
phenyl-imid,op	32	
phenyl-imid,op	33	
phenyl,op		33
phenyl,ip	54	53
phenyl,ip	56	55
γ_9 ,op	67	
γ_9 ,op	79	
$\gamma_{9,6}$,op		69
$\gamma_{9,6}$,op		75
$\gamma_{9,6}$,op		76
$\gamma_{9,6}$,op		124
$\delta_{\text{Fe-imid}}$,op	110	
$\delta_{\text{Fe-imid}}$,ip		172
ip	191	
ip,op	213	
$\gamma_6 + \nu_{\text{Fe-imid}}$,op	215	
$\nu_{\text{Fe-imid}}$,op		226
ip	222	
$\nu_{42,53}$,ip	224	
$\nu_{42,53}$,ip	225	
$\nu_{42,50}$,op		244
$\nu_{42,50}$,op		255
$\gamma_9 + \nu_{\text{Fe-imid}}$,op	228	
$\gamma_9 + \nu_{\text{Fe-imid}}$,op	248	
$\nu_{53,50}$,ip	288	
$\nu_{53,50}$,ip	293	
ip,op		301
$\nu_{49,53}$,ip		325
$\nu_{49,50,53}$,ip		338
ip		384
$\nu_{50a,53a}$,ip	404	
$\nu_{50b,53b}$,ip	406	
$\nu_{50,53}$,ip		410
$\nu_{50,53}$,ip		420
$\nu_{49,53}$,ip		470
$\nu_{49,53}$,ip		471

Table 5.2: Calculated mode assignments based on measured Nuclear Resonance Vibrational Spectroscopy of iron normal modes quoted in wavenumbers (cm^{-1}) for heme model complexes Fe(TPP)(2-MeHIm) and Fe(TPP)(CO)(1-MeIm) of deoxy- and carbonmonoxy-heme proteins, respectively [93, 94]. ν = stretch, δ = angle bend, γ = out-of-plane bend and ip, op indicate in-plane or out-of-plane motions, respectively.

as deoxy-Mb/MbCO. The first mode $\nu_{\text{Fe-His}}$ refers to the stretching mode between the central iron atom of the porphyrin ring and the nitrogen of the imidazole ring of the proximal histidine (Fig. 5.1(d)). It is noted that this mode is only resonance Raman active in the unbound (deoxy-heme) state and not the bound (heme-CO) state. Thus, the presence of the $\nu_{\text{Fe-His}}$ is a useful indicator for studying the ligated state of heme proteins. The temperature and pressure dependence of this mode has been extensively studied and assigned to anharmonic coupling between the $\nu_{\text{Fe-His}}$ and the out-of-plane and iron motion of the deoxy-heme species (Fig. 5.1(d)) [84, 95–97]. The ν_4 mode is also sensitive to the bound state of the heme group shifting significantly (approximately 20 cm^{-1}) to a lower frequency when in the unbound state. It is assigned to an asymmetric breathing mode of the porphyrin ring which is sensitive to the electrostatic environment of the central iron atom. Finally, the ν_7 mode is very intense and only shifts approximately 4 cm^{-1} and is often used as an internal standard.

Also listed are the iron normal modes measured using Nuclear Resonance Vibrational Spectroscopy (NRVS) (Table 5.2) [93, 94]. This technique does not suffer from the low frequency interference from applied laser fields as in Raman spectroscopy and therefore can determine the sub 200 cm^{-1} modes for the heme group. On the other hand the measurements are not performed directly on heme proteins nor in solution but on the model compounds 2-methylimidazole tetraphenylporphinato iron II [Fe(TTP)(2-MeHIm)] and 1-methylimidazole tetraphenylporphyrin carbonmonooxy iron II [Fe(TPP)(CO)(1-MeIm)] in polycrystalline form, which are considered to accurately mimic deoxy-Mb and MbCO active sites, respectively. Of particular interest are the lowest vibrational modes, which are assigned to deformations of the porphyrin ring called heme *doming* modes which also

modulate the position of the central iron atom in relation to the proximal histidine mentioned above in relation to anharmonic character of the $\nu_{\text{Fe-His}}$ mode.

5.4 Photophysics of Heme-CO photolysis

Proteins with a CO ligated heme undergo dissociation of the Fe-CO bond upon pulsed illumination in either the Soret or Q-bands. This reaction constitutes the most investigated of its kind [86,98]; some of the earliest experiments using femtosecond laser pulses were applied to heme proteins, both bound and unbound as a test system for studying the dynamics of *chemical* reactions. A rich pool of experimental results exists for the study of ligand photodissociation of heme proteins and many schemes for the underlying dynamics and the mechanisms which drive the reaction have been proposed. In more recent times some of the earlier schemes have been dropped in light of new evidence. There now remain two major models, each of which will be described in detail below: (i) the vibrationally excited *hot* electronic ground state model [64,66,67,69,82–85] and (ii) the multiple electronic intermediate excited state model [62,65,86].

5.4.1 Vibrationally Excited *Hot* Ground State Model

In this model [64,66,67,69,82–85], the forces driving ground state vibrational motion have been separated into two different processes called *field* driven or *reaction* driven depending on the initial binding state of the reactant. In the field driven case the ground state vibrational motion is excited by the applied laser fields and *not* by any photochemical processes taking place to affect the structure. The reaction driven case involves a reaction coordinate R and a vibrational coordinate Q (Fig. 5.3). Upon absorption of a pho-

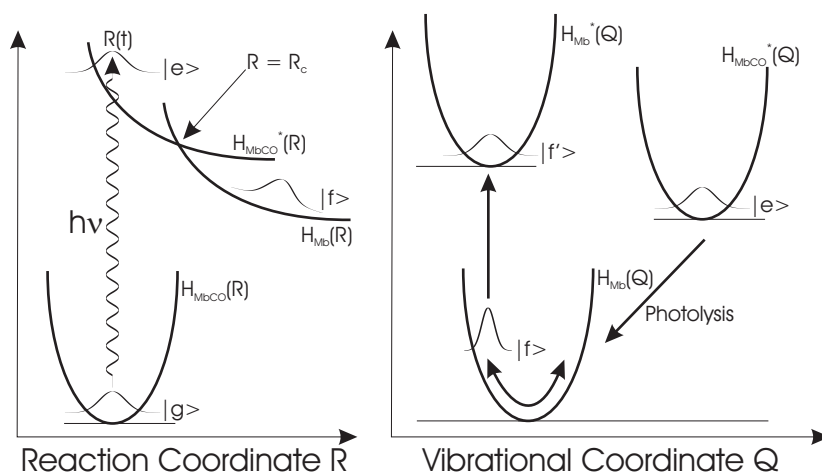


Figure 5.3: Upon excitation into the excited state the population undergoes a rapid nonradiative surface crossing through $R = R_c$ along the reaction coordinate R onto an electronic potential $|f\rangle$ which already resembles the unbound deoxy-Mb photoproduct. The nuclei coupled to the rapid electronic rearrangement find themselves far from equilibrium and undergo coherent vibrational motion along the vibrational coordinate Q . Adapted from [83].

ton the excited state population almost instantaneously ($\ll 150$ fs) crosses through $R = R_c$ onto a potential $|f\rangle$ that already resembles the photoproduct state, deoxy-Mb. The rapid crossing through $R = R_c$ and population of new electronic states leads to impulsive electronic forces being applied to vibrational modes. These impulsive electronic forces are described as follows: in the new electronic configuration which resembles the photoproduct states (deoxy-Mb) the nuclei find themselves far from equilibrium which drives the coherent vibrational motion (along Q) coupled to these nuclei. The remaining two longer relaxation time scales observed for this reaction (0.4 and 0.4-4 ps) [84] are assigned by the authors to the *cooling* of this displaced ground state population as $[\text{deoxy-Mb}]^*$ returns to equilibrium. A clear model addressing the mechanics driving the dissociation reaction is not included in this description. However, the authors [85] suggest that

any such model must include the iron spin states of the reactant (MbNO in this case) and the product (deoxy-Mb) and they consider an admixture of these spin states to accommodate direct electric dipole coupling between the reactant and product state potentials.

The supporting experimental observations are primarily based on measurements performed using femtosecond pump/probe spectroscopy with a novel detection scheme called *wavelength selective modulation* [82]. The wavelength selective modulation scheme is used to select against usually stronger population dynamics and leaves only the coherent component of the signal. This technique is applied to heme proteins to measure low frequency nuclear motion of the heme chromophore and chromophore-protein in the time domain. Of particular interest is the ground state Fe-His stretching mode of deoxy-heme (220 cm^{-1}) which is *not* resonance Raman active in ligand bound heme proteins. The presence of the Fe-His mode is measured from delay times of 150 fs with little or no apparent phase delay relative to the same measurements performed on deoxy-Mb [64, 84]. The authors argue that the absence of any significant phase delay is indicative of the instantaneous formation of the photo-product state after excitation.

Transient absorption measurements using a white light probe to measure the Soret band region for both deoxy-Mb and MbCO are found to exhibit an almost instantaneous red-shift and broadening which is assigned to a vibrationally hot ground state followed by spectral narrowing on a 400 fs timescale and blue shifting on a 4 ps timescale [69]. In the case of MbCO the initial red shift and broadening is superimposed on the photo bleaching of the MbCO Soret band which obscures the analysis though the approximately 300 fs induced absorption measured at 385 nm facilitates the assignment. The 0.4 and 0.4-4 ps processes are tentatively assigned to both an intramolecu-

lar, non-Boltzmann, vibrational redistribution process and *cooling* of a hot, Boltzmann equilibrated heme via vibrational energy transfer between the heme and the protein/solvent thermal bath [69].

Finally, an independent pump/probe study of the resonance Raman modes ν_7 and ν_4 for MbCO and another heme protein cytochrome *c* has been reported [67]. Both ν_7 and ν_4 have different frequencies depending on the binding state of the heme chromophore. A spectral shift of the ν_4 mode to the spectral position characteristic of the unbound deoxy-Mb state was measured for MbCO and notably absent for methionine bound cytochrome *c*. The absence of any significant vibrational quantum beats in the case of cytochrome *c* was explained by the weaker reaction forces imparted by a slower dissociation reaction. In the context of the reaction driven model the slower dissociation (approximately 300 fs) of methionine from cytochrome *c* results in weaker reaction forces that are insufficient to significantly displace the nuclei from equilibrium. This provides support for the reaction driven model proposed above [85] where the reaction forces drive the ground state vibrational motion after the photodissociation of nitric oxide-bound myoglobin. An estimate of < 25 fs for the dissociation process is based on the presence of the deoxy-Mb ν_4 mode (1355 cm^{-1} , period approximately 25 fs) after laser illumination of MbCO [67].

5.4.2 Multiple Excited State Model

A more detailed description of this model can be found in the original text by Franzen *et al.* [65]. The first step in the process is a vertical transition to the lowest excited states, the Q-band (Fig. 5.4). This is the well known π - π^* transition in systems involving porphyrins. The photoexcitation step is followed by fast relaxation, in < 50 fs, to an intermediate excited state

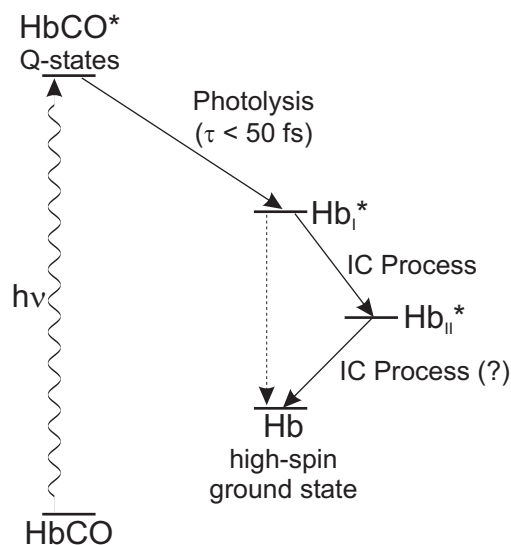


Figure 5.4: Multiple excited state model. Adapted from [86]. IC = inter-system crossing.

[62, 65, 99]. The short time scale of this step is considered to exclude the possibility of a change in the spin state of the system. This is contrary to the proposals of the previous model where the repulsive forces driving the dissociation reaction were directly attributed to rapid changes in the spin state of the heme-ligand complex.

Experimental evidence suggests that photolysis occurs at the beginning of this first fast step. The first intermediate excited state, designated as Hb_I^* , is assigned as a charge transfer, repulsive to the already dissociated ligand. Different models for describing the relevant excited states have been suggested. However, the identification of the first excited intermediate state as a charge transfer state has been given only recently by Franzen *et al.* [65]. The assignment of the first excited intermediate state to a charge transfer state by Franzen *et al.* has suggested a mechanism for the photolysis which was not considered before: the removal of one bonding electron from the iron-CO ($d_{\text{Fe}}-\pi_{\text{CO}}^*$) orbital resulting in reduced back-bonding of the ligands

to the iron. In addition, the possibility of an involvement of a high spin state in the *primary* photodissociation step has been ruled out.

The available experimental data also shows that the iron atom moves out of the plane of the porphyrin ring almost instantaneously upon photodissociation. Although the iron atom is located within the plane of the porphyrin ring in the ligated form of the heme, it is about 0.3 Å out-of-plane in the unligated species. This iron motion is probably related to the change in the spin states, where the iron switches from the low-spin configuration in the ligated species to the high-spin state of the unligated form. Experimentally, the iron motion is observed through the frequency shift of the Fe-His mode in the resonance Raman spectrum [65]. This mode assignment is confirmed by the absence of the mode shift in the spectrum of the ligated form and by X-ray studies [88]. The experimental results show that the iron motion is very fast and happens within about 300 fs. However, it is still unclear whether the iron movement follows the dissociation to yield another intermediate or whether the first intermediate already has the iron displaced from the heme plane.

Head-Gordon and co-workers [86] recently characterised the excited states involved in the initial steps of photodissociation via time dependent density functional theory (DFT) calculations. The results show that the Q states decay into the $5A''$ and $3'$ singlet excited states assigned as mixed states of antibonding Fe_d and $CO\pi^*$ orbital combinations. The latter states are repulsive along the Fe-CO stretch coordinate and, consequently, lead to the dissociation of the heme-CO bond. The nature of the repulsive states can be understood as an excitation from a π -back-bonding orbital into an anti-back-bonding orbital which satisfactorily explains their repulsive nature. However, at a separation distance of 2.5 Å, the state has charge-transfer

character from the iron to the nitrogens of the porphyrin ring as well as the CO and imidazole ligands. This is in accord with a previous experimental assignment of the first intermediate of the photodissociation process to be a charge-transfer state.

The above theoretical results have more recently been independently confirmed using the DFT calculation method [100]. Whereas the previous calculations [86] focused on the Fe-CO stretch coordinate, the recent study investigated the effect of the bending orientation of the Fe-XO moiety⁶, where X = O, C, or N. It is shown that the orbitals localised on Fe and CO all remained above the Q states almost independently of the bending orientation, thereby eliminating their possible contribution to the photodissociation process, including the previously proposed $d_{z^2}^*$ antibonding orbital. The same argument cannot be used for the Fe-O₂ and Fe-NO species thus providing a mechanism to explain the dramatic difference in the photodissociation quantum yields of the O₂ and CO complexes of heme protein.

In addition, experimental data indicate that the fast heme dissociation step is followed by several steps including gradual structural changes and probably more than one excited intermediate state [62,65]. This is depicted in Fig. 5.4, where the path of relaxation to the ground state of the unligated heme proceeds through several inter-system crossing steps. Alternatively, a different interpretation of the Raman spectra has suggested that the relaxation process following the photodissociation is dominated by populating the vibrational modes of the ground electronic state [101].

In the previous model (Sect. 5.4.1) the initial red shift of the MbCO Soret band after excitation was analysed as a broadening and red-shifting of a *single* band and interpreted as an indication of a hot ground state.

⁶Moiety is defined as an indefinite part; a small portion or share.

The alternative interpretation offered by Franzen *et al.* involved two weak absorption bands centred around 440 and 480 nm, assigned to Hb_I^* and Hb_{II}^* , respectively. In this case the spectral narrowing on the time scale of 300 fs was assigned to relaxation of Hb_I^* to Hb_{II}^* before finally equilibrating to the photoproduct state of deoxy-Mb in about 3-4 ps.

5.5 One-Colour Spectrally Resolved Photon Echoes of Deoxy-Mb and MbCO

In this section the one-colour spectrally resolved photon echo (and the related transient grating) technique is applied to the heme protein myoglobin in both the unbound (deoxy-Mb) and bound (MbCO) states. There are two purposes of these experiments: (i) To determine the nature of the ultrashort photophysical states of myoglobin with and without the photodissociation reaction occurring to investigate the mechanism of removing the carbonyl. (ii) To further characterise this new technique and in order to investigate the signal response when a system has a short lived (< 50 fs) finite excited state lifetime.

The one-colour spectrally resolved photon echo results for deoxy-Mb and MbCO presented in this section were measured using the experimental apparatus described in section 3.2 on page 45. The photon echo spectra were measured at fixed coherence times in the range $t_{12} = -80$ to 80 fs while the population time was scanned in the range $t_{23} = -250$ to 3300 fs. The signals were measured in the phase-matching direction $\vec{k}_s = \vec{k}_3 + \vec{k}_2 - \vec{k}_1$ and three experimental laser wavelengths were used 585, 590 and 600 nm.

5.5.1 Results

Figure 5.5 shows the one-colour photon echo and spectrally resolved transient grating ($t_{12} = 0$) signals for MbCO and deoxy-Mb that were fit to produce the data presented in Figure 5.6. Figure 5.6 shows that the photon echo peak shift and the transient grating spectral linewidth for MbCO at 585, 590 and 600 nm have a comparable laser-wavelength dependent signal response. All the signals have an intermediate rise τ_2 of 200-250 fs followed by a constant offset A_3 (Table 5.3). Only the peak shift offset A_3 of 3.3-3.5 fs is meaningful here; the spectral width offset is not background free. The early population time dynamics, on the other hand, exhibit a significant laser-wavelength dependence. Whilst all the signals have a rapid decay during the pulse overlap region, the 590 and 600 nm signals have a pronounced additional rapid decay followed by an equally rapid rise (*dip*) which is described by a Gaussian have a width approximating the laser pulse width (σ_{t_E} approximately 36 fs) that increases in amplitude with increasing laser

Table 5.3: Least-square fit results for measured one-colour peak shift and spectral width signals of MbCO.

λ_E (nm)	A_1	t_0 (fs)	σ_1 (fs)	A_2	τ_2 (fs)	A_3
Peak Shift						
585 ^a				-19.4	240	3.3
590 ^b	-4.3	94	26	-10.7	210	3.5
600 ^b	-12.2	90	44	-7.4	215	3.5
Spectral Width						
585 ^a				-0.2	250	3.1
590 ^b	-0.1	75	16	-0.1	220	3.1
600 ^b	-0.3	73	24	-0.2	200	3.2

^a *Fit* = $A_2 \times \exp(-t_{23}/\tau_2) + A_3$. Data fit for population times $t_{23} > 90$ fs

^b *Fit* = $A_1 \times \exp(-(t_{23} - t_0)^2/\sigma_1^2/2) + A_2 \times \exp(-t_{23}/\tau_2) + A_3$. Data fit for population times $t_{23} > 40$ fs.

wavelength. The 585 nm signals, on the other hand, have the rapid decay but the additional dip is essentially absent.

A comparison of the deoxy-Mb and MbCO peak shift fit parameters (Table 5.4) measured using 600 nm laser pulses reveals the absolute value of the amplitude A_1 of the Gaussian mode fitting the dip is smaller for deoxy-Mb (-1.9/-12.2) and the decay time of the exponential rise τ_2 is longer (approximately 300/200 fs). The same comparison using the transient grating spectral width fit parameters (Table 5.4) shows the absolute value of the Gaussian amplitudes A_1 are approximately equivalent (-0.39/-0.30) but the decay time of the exponential rise τ_2 is similarly longer for deoxy-Mb (approximately 300/200 fs). A comparison of the deoxy-Mb and MbCO transient grating integrated intensity fit parameters (Table 5.4) shows the same trends with the amplitude A_1 of the pulse width-limited decay being significantly smaller for deoxy-Mb (0.20/0.63) and the decay time τ_2 is longer for deoxy-Mb (155/100 fs). The integrated intensity signals are normalised to the deoxy-Mb maximum (Fig. 5.7). The difference of the maximum inte-

Table 5.4: Least-square fit results for measured one-colour transient grating intensity (Int), peak shift (PS) and spectral width (PW) for deoxy-Mb (Mb) and MbCO at 600 nm.

Para	A_1	t_0 (fs)	σ_1 (fs)	A_2	τ_2 (fs)	A_3
Mb, Int ^a	0.20		40	0.73	155	0.07
MbCO, Int	0.63		48	0.33	100	0.04
Mb, PS ^b	-1.87	70	25	-13.06	310	2.83
MbCO, PS	-12.2	90	44	-7.4	215	3.5
Mb, PW ^b	-0.39	87	39	-0.14	300	3.21
MbCO, PW	-0.3	73	24	-0.2	200	3.2

^a $Fit = G(t) \otimes F(t)$, where $G(t) = \exp(-t^2/\sigma^2/2)$ and $F(t) = A_1 \times \exp(-t^2/\sigma_1^2/2) + A_2 \times \exp(-t/\tau_2) + A_3$. The width σ of the response function $G(t)$ was a free fit parameter.

^b See Table 5.3.

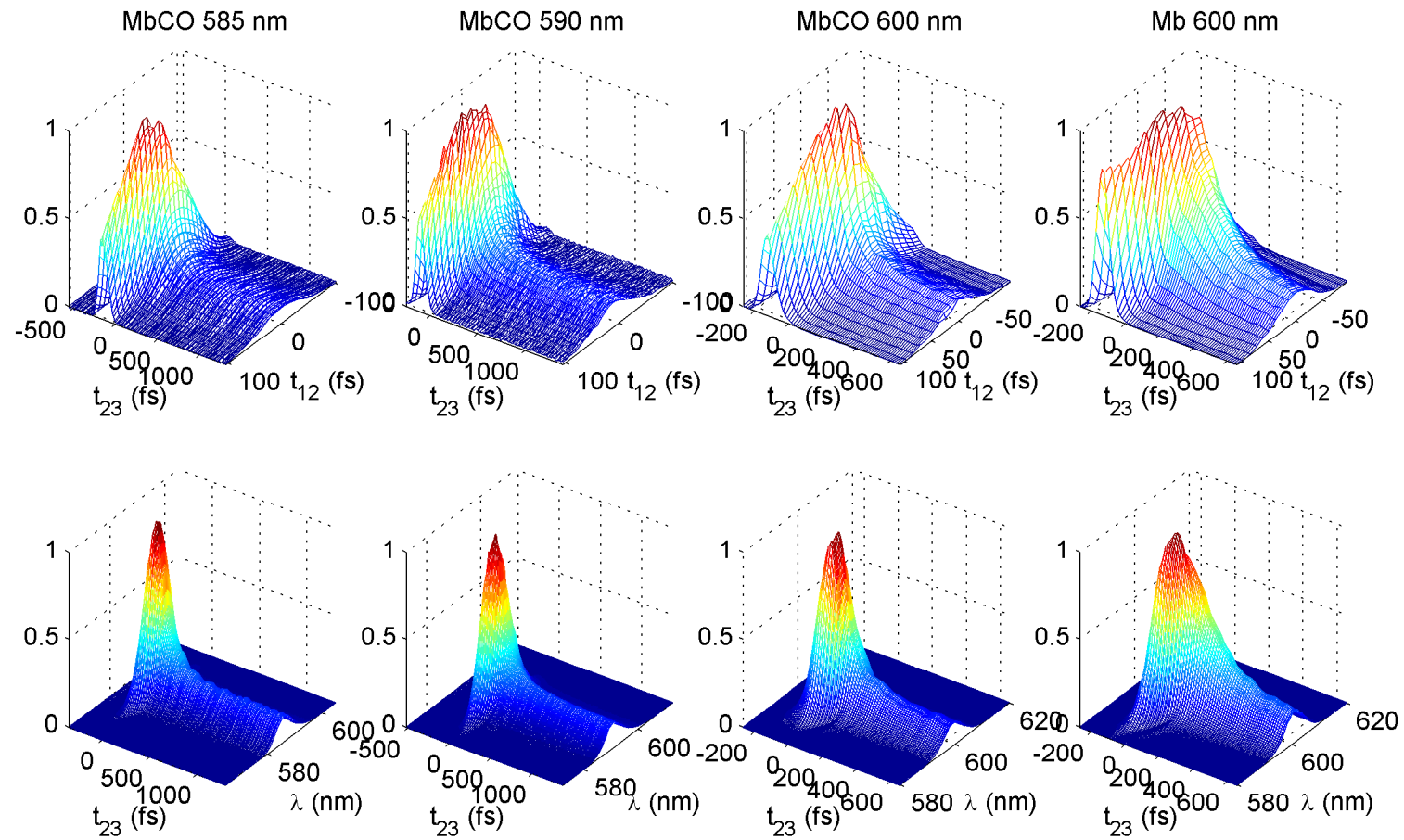


Figure 5.5: Mesh plot of one-colour photon echo (top row) and spectrally resolved transient grating (bottom row) of MbCO and deoxy-Mb at three different wavelengths as indicated. This data was fit to produce the photon echo peak shift and transient grating spectral width data presented in Figure 5.6.

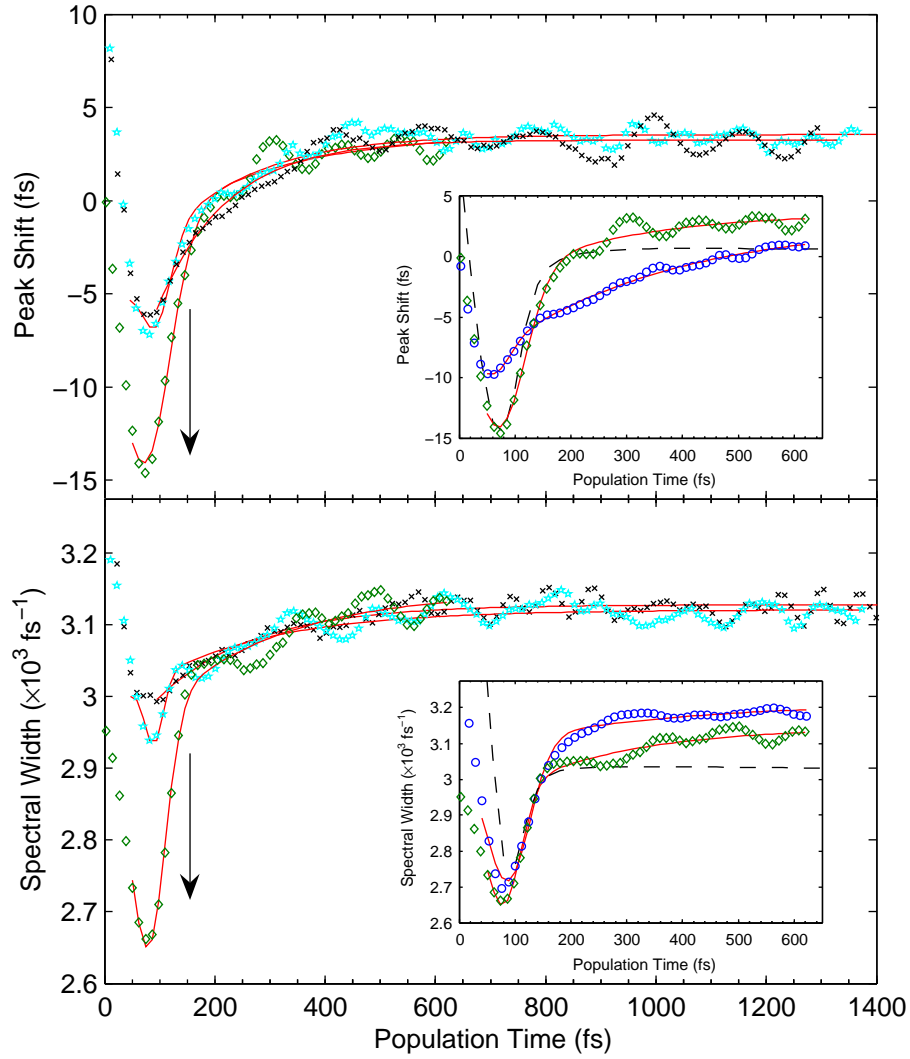


Figure 5.6: One-colour photon echo peak shift and spectrally resolved transient grating spectral width results for MbCO at three laser wavelengths of 585, 590 and 600 nm (crosses, stars and diamonds, respectively). Arrows indicate the increasing dominance of a rapid decay and rise feature for $t_{23} < 150$ fs as the laser wavelength was increased. Insets show the 600 nm results for both deoxy-Mb (circles) and MbCO (diamonds). Least squares fits are shown as solid lines. Calculated results shown as dashed lines - see text on page 126 for details.

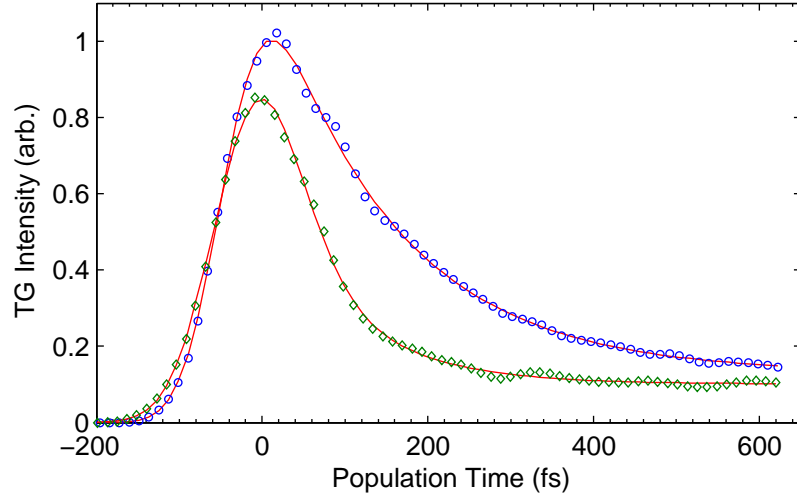


Figure 5.7: One-colour integrated transient grating intensity of deoxy-Mb (circles) and MbCO (diamonds) at 600 nm. Parameters for least-squares fit (solid line) are listed in Table 5.4. Note both traces are normalised to the deoxy-Mb maximum.

grated intensity reflects the difference in the linear absorption for deoxy-Mb and MbCO around 600 nm (Fig. 5.2(a)).

Figure 5.8 shows the difference centre frequency for myoglobin at three different coherence times $t_{12} = -47, 0$ and 47 fs. The difference centre frequency was calculated by subtracting the deoxy-Mb centre frequency from the MbCO centre frequency. The transient grating ($t_{12} = 0$) difference centre frequency shows a rapid rise from zero to approximately 40 cm^{-1} peaking at a population time around 190 fs. The difference centre frequency exhibits a strong coherence time-dependence: All of the signals exhibit the same asymptotic rise to a maximum of approximately 40 cm^{-1} but as the coherence time t_{12} is increased the population time at which this rise occurs shifts towards zero. Importantly, the size of the shift is approximately equal to the change in coherence time, i.e., the difference centre frequency trace measured at the coherence time $t_{12} = 47$ fs is shifted by approximately 47

fs towards the population time zero from the trace measured at $t_{12} = 0$.

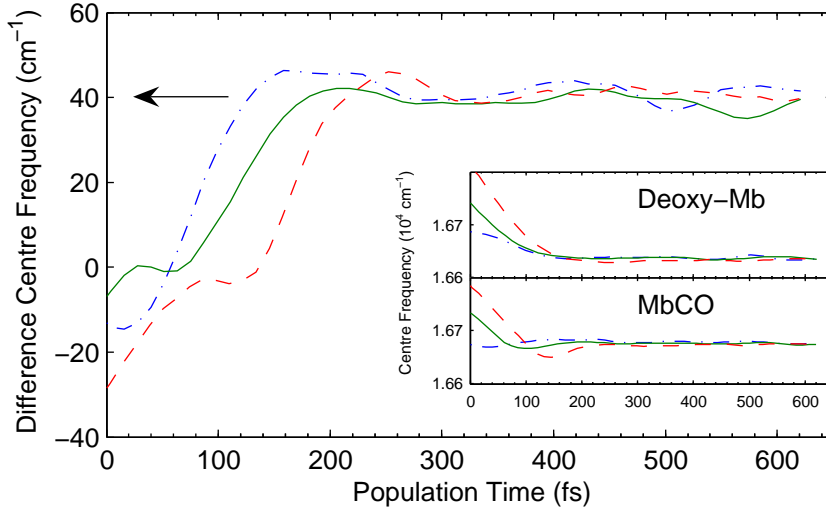


Figure 5.8: One-colour difference centre frequency of MbCO compared to deoxy-Mb at 600 nm for three different coherence times $t_{12} = 47, 0, -47$ fs; dash dot, solid and dashed lines, respectively. Arrow indicates the direction of increasing coherence time t_{12} . Insets show the original centre frequency curves.

Spectrally resolved transient grating signals measured over a longer population time range are presented in Figure 5.9. In this example the short time dynamics are neglected and the population and quantum beat signals are fit simultaneously using the matrix pencil method (see section 3.4.3 on page 54) for population times $t_{23} > 180$ fs. The transient grating intensity has two exponential decays times of 100 and 1700 fs and a constant offset (Table 5.5). The centre frequency exhibits a slow blue shift with a rise time 3800 fs and the spectral width has a rise time of around 180 fs (Table 5.5). The corresponding Fourier spectra with the population components removed are also presented and compare well with those found in the literature (Tables 5.1 and 5.2). All show the presence of the Fe-His stretch mode ($221\text{-}224\text{ cm}^{-1}$) as well as low-frequency doming modes ($< 125\text{ cm}^{-1}$)

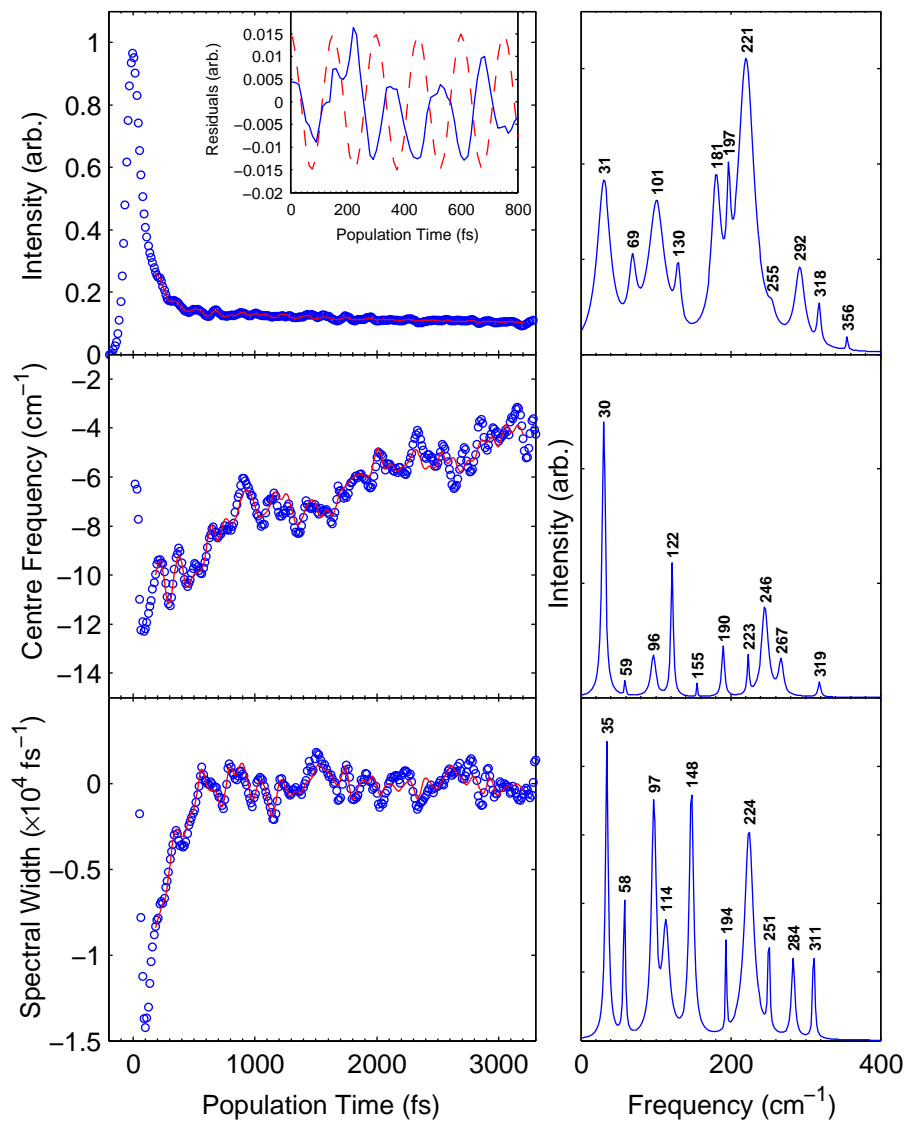


Figure 5.9: Transient grating intensity, centre frequency and spectral width results for MbCO measured using 585 nm laser pulses. Fits to the data using the matrix pencil method (solid lines) and the retrieved Fourier spectra (right column) are included. Note fits were applied for population times $t_{23} > 180$ fs - see text for details. Inset shows the transient grating intensity residuals after the population components were removed (solid line) and a cosine function with the same period as the Fe-His mode and a phase shift of zero (dashed line).

and an additional mode which is attributed to difference and sum frequency modes of the coupling between the Fe-His stretch and the doming modes (approximately 190 and 250 cm^{-1}). Figure 5.9 (inset) also shows the transient grating residuals after an analytical fit of the population dynamics compared to a cosinusoid with a phase shift of zero and period of the Fe-His stretch mode. It can be seen in the inset that at early population times $t_{23} < 180$ fs the quantum beat signal follows the Fe-His stretch mode with approximately the same phase. At around $t_{23} = 180$ fs the quantum beat signal rapidly changes phase and becomes approximately π out of phase with the cosinusoid.

Table 5.5: Exponential components of matrix pencil method fits to transient grating intensity (Int), spectral width (PW) and centre frequency (CF) for MbCO measured using 585 nm laser pulses. Note that the fit was applied to population times $t_{23} > 130$ fs.

Para	A_1	τ_1 (fs)	A_2	τ_2 (fs)	A_3
Int	0.11	100	0.05	1700	0.10
PW	1.05	190			28
CF			9.94	3600	17060

5.5.2 Discussion

It is helpful to begin with a description of the photodissociation processes as supported by these results. Upon excitation to the first excited state the Fe-CO bond is stretched from impulsive excitation until it reaches the internuclear distance required for the excited state population to cross (with quantum efficiency of unity) from the first excited state onto the dissociative intermediate excited state. During the initial stretch of the Fe-CO the Fe-His bond is initially compressed and begins to oscillate. The excited state population rapidly migrates along the dissociative potential to an Fe-CO in-

ternuclear separation of approximately 2.5 Å, during which time the system switches from the bound S=0 to the unbound S=2 spin state thus approximating the deoxy-Mb ground state though still in an excited state. The intermediate excited state population then relaxes to a deoxy-Mb ground state with a non-equilibrium charge distribution. The first excited state (Q-band) is quasi-degenerate and localised on the porphyrin ring. The second excited state is also quasi-degenerate and the states are denoted as $5A''$ and $3A'$ (Fig. 5.10). The $5A''$ and $3A'$ states are repulsive to the carbonyl group and at an Fe-CO distance of 2.5 Å have ultrafast iron-to-porphyrin ring charge transfer character [65,86]. A longer-lived (approximately 3 ps) third state has porphyrin ring-to-iron back charge transfer to produce the porphyrin ground state with a non-equilibrium iron d-orbital population [65].

Peak Shift and Spectral Width

To describe the dynamic profile of the photon echo peak shift signal requires the inclusion of a third electronic excited state although the following is initially concerned with a two-level system. It has been shown theoretically for a two-level system with a finite excited state lifetime that a rise in the peak shift occurs [102]. In short the theory has three response functions to describe the nuclear dynamics for a system with a finite electronic lifetime assuming linear electronic-phonon coupling. The first response function describes the ground state nuclear dynamics which do not change during the population period. The second describes the nuclear motion in the excited state which has an exponential decay component that decreases the total contribution during the population period. The third and most interesting response function describes the phase shift associated with the relaxation

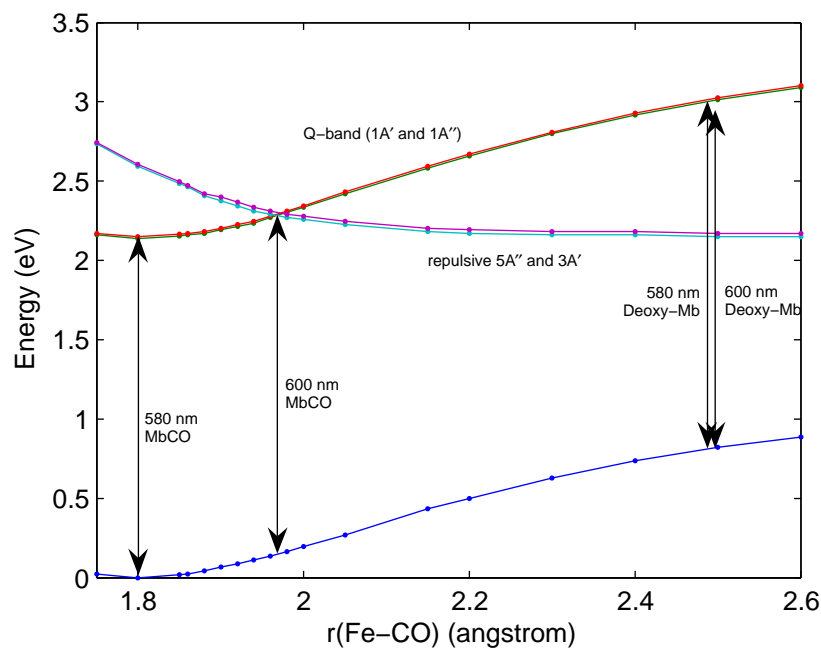


Figure 5.10: Electronic structure of MbCO model complex as a function of the Fe-CO bond distance calculated using density functional theory [86]. The figure has been adapted to correct for the small over-estimation of the excited state energy.

from the excited state to the ground state. The system in this case makes an odd number of interactions with the field on the bra and ket sides and thus contributes to the total response function with a minus sign which reflects the recovery of the hole in the ground state. It is noted that this treatment was extended to a three-level system and a weaker effect was observed; however, there were several important assumptions/simplifications made which do not apply here and could be used to justify extending the above concepts to the three-level system to be proposed here. The first assumption was that the population lifetime was longer than the dephasing time and was subsequently neglected during the coherence period. Secondly, it followed from the first assumption that the transfer of population from the first excited

state to the second was an incoherent process. Thirdly, the third electronic level was assumed to be non-resonant with the laser fields. No negative peak shift values were reported [102] although the numerical calculations of the two-level system with a finite lifetime and finite width laser pulses appear to have been restricted to peak shift values greater than or equal to zero. It is noted that similar peak shift responses have been measured for another heme protein, cytochrome *c* [75]. The results for cytochrome *c* exhibit the initial rapid decay around time zero followed by a slower rise to an asymptotic non-zero position, though again no negative peak shift values were reported. In the following, each of the three above assumptions and proposals for modifying them to support a three-level system model are discussed.

It is proposed, based on the density functional theory results reported by Dunietz *et al.* [86], that the photodissociation of MbCO involves a three-level electronic structure where the transfer of population from the first to the second excited state is a coherent process through an avoided (adiabatic) surface crossing. If the transfer of coherence can be modelled as a coherent process then it follows that it can be included during the coherence period t_1 that describes the system when in a coherent state (see section 2.3 on page 30). Another argument for the inclusion of fast finite population dynamics during the coherence period is the previously reported [11] t_{13} dependence of the population period rather than t_{23} which can also be seen in the difference centre frequency results discussed below. The implication of a t_{13} dependence is that the population dynamics actually begin on the first laser interaction rather than the second. As a qualitative test, a peak shift calculation was performed for a two-level system with different dephasing dynamics in the ground and excited states and an infinite population life-

time. The excited state was given a dephasing time of 30 fs while the ground state had a dephasing time of 1700 fs (Fig. 5.6(inset)). The results show that the peak shift drops to negative times followed by a rapid rise returning to positive times in a similar manner to the measured results. The rapid dephasing in the excited state was intended to reflect the finite population lifetime. Whilst this method for the inclusion of population dynamics is not rigorous it does appear to account for the negative peak shift component of the signal, thus suggesting that finite population lifetimes should be included during the coherence period. Note that the size and position of the dip varies with the laser pulse width and detuning and with the decay time of the excited state dephasing (lifetime).

It is proposed here that the third electronic level is resonant with the laser pulses in contrast to the third assumption above (Fig. 5.10). Furthermore, it is known that the photodissociation occurs with quantum unity and thus it is assumed that there is complete transfer of population from the first to the second excited state. Taking this into account it is possible to consider the relaxation of the second excited state to the ground state in a similar manner to the finite lifetime two-level system investigated by Yang *et al.* [102]. This allows for the inclusion of any nuclear trajectory phase changes associated with the transfer from the first to the second excited state. Using this description of the system it would be possible to account for the slower (200-300 fs) rise seen in peak shift and transient grating spectral width signals (Fig. 5.6).

Developing a model that included the fast finite population lifetime during the coherence period and the third response function described by Yang *et al.* [102] to model the dip and the slower rise, respectively, of the measured peak shift and transient grating spectral width would be ideal. However, de-

velopment of a model of this complexity is beyond the scope of this thesis. Notwithstanding the absence of a theoretical treatment, it is proposed that the first fast decay in the first 50 fs and subsequent rapid rise (dip) results from the rapid loss of the Q-band population to the second CO repulsive excited states $5A''$ and $3A'$ which considerably affect the dynamics during the coherence period. Superimposed on this is the effect of the slower intermediate population relaxation of the $5A''$ and $3A'$ states to a third state which already resembles the deoxy-Mb ground state, albeit with an un-equilibrated charge distribution which through phase changes in the nuclear trajectory causes the signals to rise. There is also some evidence to suggest that there is a slow relaxation of the peak shift; however, this is particularly small and unfortunately obscured by low-frequency quantum beats (i.e., 35 cm^{-1}) and insufficient length of the scans. To confirm this point would require longer scans with a larger dynamic range for the peak shift axis. Regardless, most of the resultant non-zero offset in the peak shift can be attributed to inhomogeneous broadening. Moreover, the underlying photophysics described here are proposed to be analogous to the processes occurring in the deoxy-Mb case albeit with a longer lifetime for the second excited state and different dynamics in the case of the first excited state. However, with approximately 85 fs laser pulses it is not clear how the fast dynamics differ.

The correspondence between the photon echo peak shift and the transient grating spectral width is good, at least for the MbCO signals. The reason for presenting the data as the spectral width in this case (Figs. 5.6 and 5.9) rather than the inverse linewidth as in Chapter 2 is to allow a comparison with the peak shift. It would be equally valid to analyse the data as the inverse linewidth without changing the interpretation, since all the signals in these measurements are dominated by population dynamics rather

than the previously studied dephasing processes, i.e., it is not necessary for the spectral width data to be exhibiting a rise in order to assign the decay to the second electronic excited state. The numerically calculated result also describes the short lived dip for the spectral width though less convincingly (Fig. 5.6). It is this discrepancy and the results of a two-colour measurement discussed below that lead us to assume that the spectral width is more susceptible to pulse overlap (coherence spike) processes than the peak shift in this particular example.

Comparison of Deoxy-Mb and MbCO

The photon echo peak shift and transient grating spectral width results suggest that the first fast pulse width-limited decay has a smaller amplitude A_1 and the population decay time of the second electronic excited state τ_2 is longer for deoxy-Mb than MbCO. The transient grating intensity signals also exhibit this difference in decay times. The amplitude of the pulse width-limited decay A_1 is smaller (0.2 compared with 0.63) and the second decay time τ_2 of approximately 155 fs for deoxy-Mb is significantly longer than the 100 fs for MbCO. These values agree well with the peak shift and spectral width results, if the fact that the transient grating intensity signals decay in half the time of the population lifetime is taken into account. In this case the decay times τ_2 of 155 fs and 100 fs for deoxy-Mb and MbCO, respectively, agree well with those determined using peak shift and spectral width, approximately 300 fs and 200 fs, respectively. The offset A_3 is indicative of longer timescale relaxation processes as seen in the 585 nm results discussed below.

The comparison of deoxy-Mb and MbCO transient grating centre frequencies provides additional insight into the photophysics of the photodis-

sociation of MbCO. The blue shift of the MbCO centre frequency around $t_{23} = 100\text{-}200$ fs of approximately 40 cm^{-1} compared to the equivalent deoxy-Mb signal is attributed to the onset and completion of a change from the low spin $S=0$ of the bound MbCO to the high spin $S=2$ of the unbound deoxy-Mb. The low frequency doming mode approximately 40 cm^{-1} is linked to the displacement of the central iron atom relative to the plane of the porphyrin ring. The displacement of the central iron atom relative to the plane of the porphyrin is linked to the spin state of the system. In the low spin (bound) state the central iron atom is effectively in-plane whilst in the high spin (unbound) state the central iron atom is out-of-plane. Thus the displacement of the centre frequency of MbCO relative to deoxy-Mb of (approximately 40 cm^{-1}) is attributed to the change in spin state associated with the change from the low spin bound state to the high spin unbound state. The absence of any change in the deoxy-Mb centre frequency is attributed to the central iron atom already residing out-of-plane, so that there is no significant perturbation to the system. The onset of this spectral shift occurs at the beginning of the well separated pulse limit for 85 fs FWHM laser pulses and rapidly reaches an equilibrium position at around 200 fs on the measured timescale. This is consistent with the proposal that the intermediate electronic level already exhibits high spin character as previously reported for MbCO photodissociation [65,86]. The apparent discrete nature of the spectral shift (i.e., 40 cm^{-1} compared with the frequency of the heme doming vibrational mode) is not unexpected if one recalls the well resolved vibrational splitting of the transient grating spectra measured for rhodamine 101 in the previous Chapter. In the case of rhodamine 101 the splitting of the spectra was equal to the vibrational splitting of the dominant vibrational mode. In the myoglobin spectra the spectral splitting is less well resolved because of

the high density of vibrational modes, the low-frequency of the vibrational splitting and the amount of spectral smoothing applied to remove what was initially believed to be problems with fibre coupled delivery of the signal to the spectrometer. However, the dominance of the low-frequency vibrational mode can be seen in the retrieved Fourier spectra (Fig. 5.9) and the small shift of the MbCO centre frequency is resolvable because of the ability to remove the background spectral decay using the deoxy-Mb spectra. It is noted that there is further evidence for the assignment of the spectral shift to the displacement of the central iron atom and associated change in spin state in the one-colour transient grating results measured at 585 nm and discussed below.

The coherence-time dependence of the rapid spectral change in the difference centre frequency supports the proposal that the population period is better described by t_{13} and not t_{23} [11]. This is also an important concept for the justification for the inclusion of finite population dynamics during the coherence period which is necessary to adequately model the photon echo peak shift signals for myoglobin.

Spectrally Resolved Transient Grating of MbCO Measured at 585 nm

The reason for fitting the population dynamics and quantum beat signals simultaneously was to avoid complications that arise from the appearance and long period approximately 950 fs of the low-frequency approximately 35 cm^{-1} mode. The residuals of the transient grating intensity exhibit an important feature at early times (Fig. 5.9). At population times $t_{23} < 180 \text{ fs}$ the quantum beat signal appears to follow a cosine function with period equal to that of the Fe-His stretch and phase shift of zero. It is

not possible to see if the low frequency mode is present during this period because it is not long enough. For population times $t_{23} > 180$ fs there was a significant perturbation of the signal and the Fe-His stretch component of the signal now oscillating with a π -phase shift and the presence of the low-frequency approximately 35 cm^{-1} mode can be seen. The underlying photochemical processes is described as follows: (i) Upon excitation the Fe-His mode is initially compressed. This has previously been proposed and can be understood if the Fe-CO bond is lengthening on the opposite side of the porphyrin ring (Fig. 5.11) is considered [64]. (ii) As the central iron atom moves out-of-plane of the porphyrin ring around 180 fs the Fe-His bond is compressed again and to a larger extent causing the Fe-His bond to now be π out of phase relative to time zero (Fig. 5.11) and the significant presence of the low-frequency doming mode. This supports the assignment of the MbCO spectral shift to the out-of-plane displacement of the central iron atom discussed above and thus the proposal of Dunietz *et al.* [86] that the second excited state has high spin character at an Fe-CO bond length around 2.5 \AA . Thus in order to differentiate between the population dynamics and the changes in the quantum beat signal it is necessary to fit all the processes simultaneously and at times after the significant perturbation to the quantum beat signal. It is noted that the population lifetime estimates are all approximate because of these considerations and that all the fitting is performed as a sum of exponentials and/or cosine functions which means they are not independent of each other.

The population dynamics taken from all three signals, intensity, centre frequency and spectral width agree well with the literature values of < 85 fs, 200-400 fs and 2-4 ps, again taking into account that the transient grating intensity decays at twice the rate of the population lifetime [65, 84, 85].

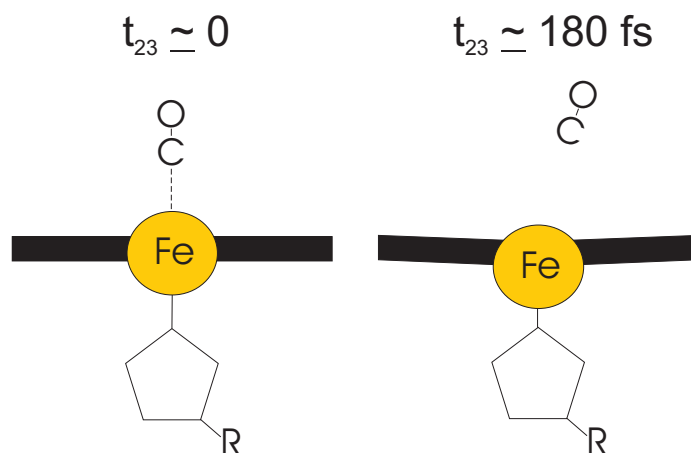


Figure 5.11: At $t_{23} = 0$ the Fe-CO bond is lengthening, the Fe-His bond is compressed and the central iron atom is mostly in-plane with the porphyrin ring. Around $t_{23} = 180$ fs the central iron atom moves out-of-plane with the porphyrin ring which further compresses the Fe-His bond.

The nature of the longer lived species is likely to be a combination of iron-to-porphyrin ring charge transfer and protein-porphyrin vibrational relaxation. The vibrational spectra, and particularly the spectral width result, also agree well with the results found in the literature and across the three different signals (Tables. 5.1 and 5.2) [64, 84]. The shift of the mean Fe-His stretch frequency $222.6 \pm 1.5 \text{ cm}^{-1}$ from the Raman value of approximately 220 cm^{-1} is consistent with the literature and results from the anharmonic coupling of the Fe-His stretch mode, i.e., the frequency is wavelength dependent. It has been shown previously that the heme doming modes have anharmonic coupling and that there is considerable coupling between the heme doming modes and the Fe-His stretch [64, 84]. The coupling between the heme doming modes and the Fe-His stretch mode is apparent here with the presence of the sum and difference frequency modes either side of the Fe-His stretch mode. It is also interesting to note that the initial Fe-His quantum beat has no phase shift at time zero which agrees well with pre-

vious studies suggesting photolysis occurs almost instantaneously [84, 85]. This proposal will be further investigated in the next section. Most of the modes for the Fe-His bond have relaxation times of order 2-3 ps. The Fe-His mode relaxes with a time of approximately 800 fs which is consistent with previous findings and the proposed coupling between the Fe-His and doming modes [64, 82, 84].

5.5.3 Additional Features of One-Colour Spectrally Resolved Photon Echoes

Figure 5.12 shows the spectrally resolved photon echo signals for deoxy-Mb measured at 600 nm and different coherence times while the population time is scanned. The photon echo spectra show significant coherence time-dependent spectral broadening at early population times. For positive coherence times the spectral broadening appears on the red side of the spectra; for negative coherence times the spectra are broadened on the blue-side; while for coherence times near zero the spectral broadening is relatively evenly distributed on both the red and blue sides. This suggests that it is possible to selectively measure either ground or excited state dynamics through tuning of the coherence time and measuring the spectrum. The absence of the effect at longer population times is attributed to the short excited state lifetime of the heme chromophore. Thus it would be interesting to repeat this type of experiment on a molecular system with a longer excited state lifetime. The spectral width as a function of population time taken at different coherence times also shows a significant coherence time-dependence (Fig. 5.13). As the coherence time increases the amplitude of the quantum beat signal increases, a feature which could provide a significant advantage for determining the vibrational dynamics in systems with very small amplitude

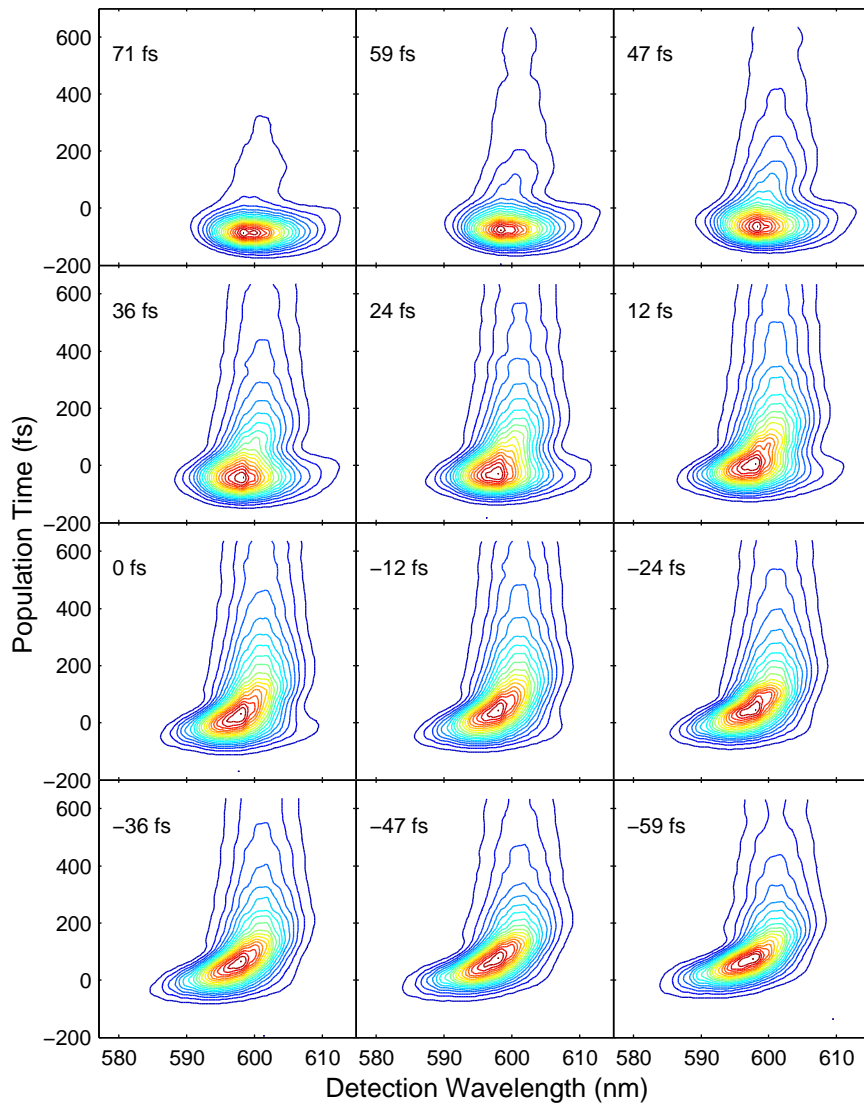


Figure 5.12: Spectrally resolved one-colour photon echo results for deoxy-Mb measured using 600 nm laser pulses. Each plot shows the photon echo spectra measured as a function of population time at a given coherence time as indicated.

quantum beat signals.

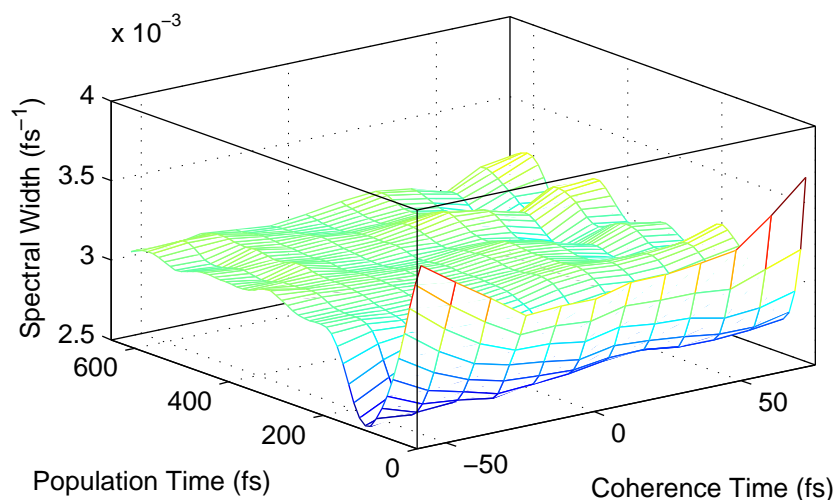


Figure 5.13: Spectral width results from data presented in Fig. 5.12 plotted as a function of both the coherence time and population time. Note how the amplitude of the quantum beat signal increases with increasing coherence time.

5.5.4 Summary

The assignment of the intermediate decay time τ_2 to a second electronic level using photon echo peak shift, the ultrafast change in spin state at around 180 fs associated with the second excited states $5A''$ and $3A'$ states and the demonstrated correspondence between the peak shift and spectral width signals constitute some of the significant findings of this thesis. The lower level of correspondence in the deoxy-Mb case will be reconsidered in the next section and will be shown to be mostly due to issues with coherence *spike* processes. The additional information gained and the more accurate determination of vibrational spectra using the spectrally resolved measurement are also important results.

5.6 Two-Colour Spectrally Resolved Transient Grating of Heme Proteins

The results for two-colour spectrally resolved transient grating measurements of the unbound deoxy-Mb and bound MbCO are presented (Fig. 5.14). In this section advantage is taken of the non-direct coupling of the wavepacket created in the doorway state (580 nm) to the dynamics probed in the window state (600 nm) in the two-colour regime. The non-direct coupling provides more certainty to pulse ordering and thus lessens the effect of coherence spike processes which in turn allows more accurate determination of photophysical processes occurring on a timescale of order of the pulse width. In the two-colour regime it is also possible to spectrally filter any scattered radiation from the pump pulses from the probe spectral region. This in combination with the larger amplitude of quantum beat signals found in spectral width data (see Chapter 2), can be used to advantage, to determine the low frequency vibrational spectrum. The measurements were performed using the experimental procedure described in Chapter 3. The central wavelength for the first two laser pulses $E_{1,2}$ is approximately 580 nm and for the third laser pulse E_3 is approximately 597 nm.

5.6.1 Results

Transient Grating Intensity

The two-colour transient grating intensity signal for MbCO (Fig. 5.15) has two exponential decay times, 100 fs and 1.5 ps, and a constant offset on the measured timescale (Table 5.6). The intensity peak is delayed approximately 35 fs from the corresponding peak in the one-colour measurement (Fig. 5.15). The deoxy-Mb signal also has two exponential decay times,

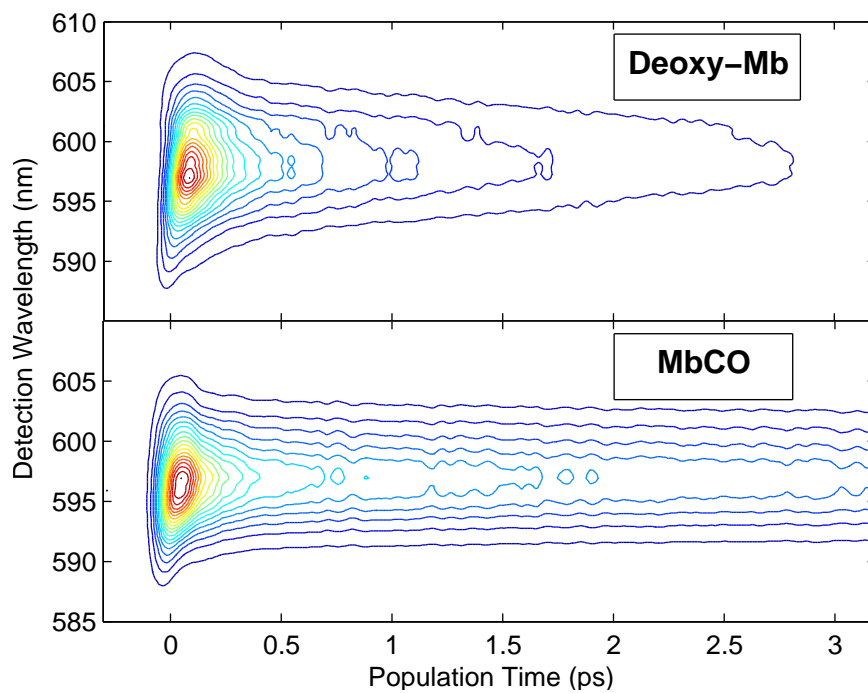


Figure 5.14: Two-colour spectrally resolved transient grating spectra of deoxy-Mb and MbCO as indicated.

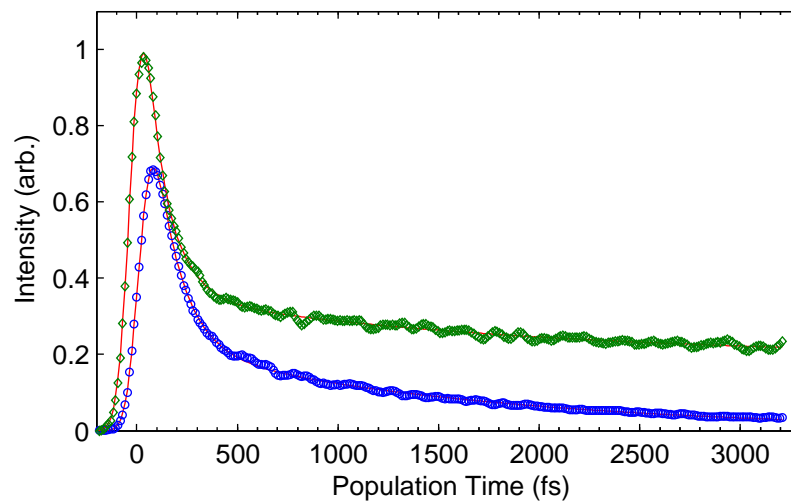


Figure 5.15: Two-colour transient grating intensity results for deoxy-Mb (circles) and MbCO (diamonds) measured using the first two laser pulse at 580 nm and the third at 600 nm. Least squares fits shown as solid lines.

125 fs and 1.5 ps, though in contrast to MbCO the intensity decays to zero. The intensity peak is delayed by approximately 85 fs from the corresponding peak in the one-colour measurement and 45 fs from the two-colour peak intensity for MbCO. The signals are normalised to the MbCO peak intensity and the intensity of the deoxy-Mb maximum is approximately 0.7 of the MbCO signal maximum. This is a reflection, in part, of the difference in the linear absorption of the deoxy-Mb and MbCO at 580 nm (Fig. 5.2).

Difference Centre Frequency

The difference centre frequency was calculated by subtracting the deoxy-Mb centre frequency signal from the corresponding MbCO centre frequency signal in a similar manner to the one-colour signal above. The difference centre frequency shows the same rapid blue shift of approximately 40 cm^{-1} at a population time around 200 fs (Fig. 5.16). This is followed by a very slow blue shift of approximately 5 cm^{-1} which is attributed to errors in the determination of the difference frequency and will not be considered.

Spectral Width

The two-colour transient grating spectral width results have been split into the population and quantum beat components of the signal for clarity. The population component was fit from $t_{23} > 130 \text{ fs}$ (Fig. 5.17). The MbCO signal has a signal exponential rise time of around 200 fs while the deoxy-Mb has a signal exponential rise of around 400 fs (Table 5.6). Both signals have a rapid decay in the pulse overlap region though the rapid rise observed in the corresponding one-colour signals is absent (Fig. 5.17). The quantum beat component of the spectral width signal (Fig. 5.18) is fit from $t_{23} > 180 \text{ fs}$ and has a similar Fourier spectrum to the one-colour Fourier spectrum mea-

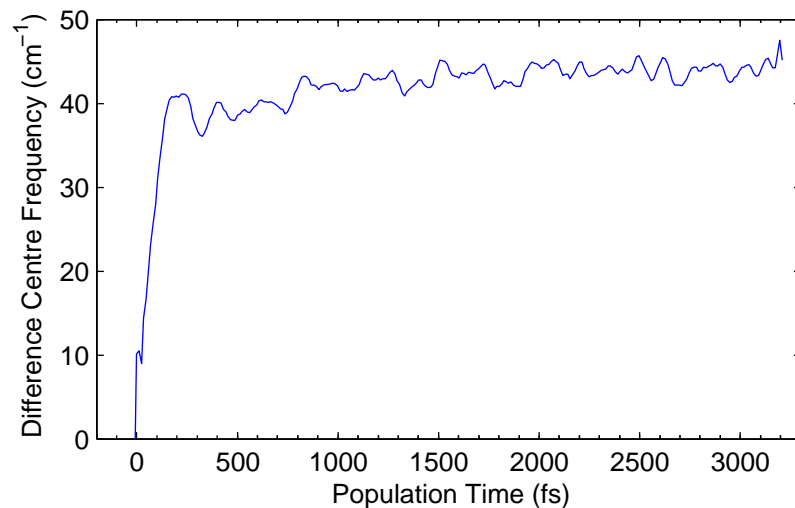


Figure 5.16: Difference centre frequency result taken from the two-colour centre frequency results for deoxy-Mb and MbCO. See text for details.

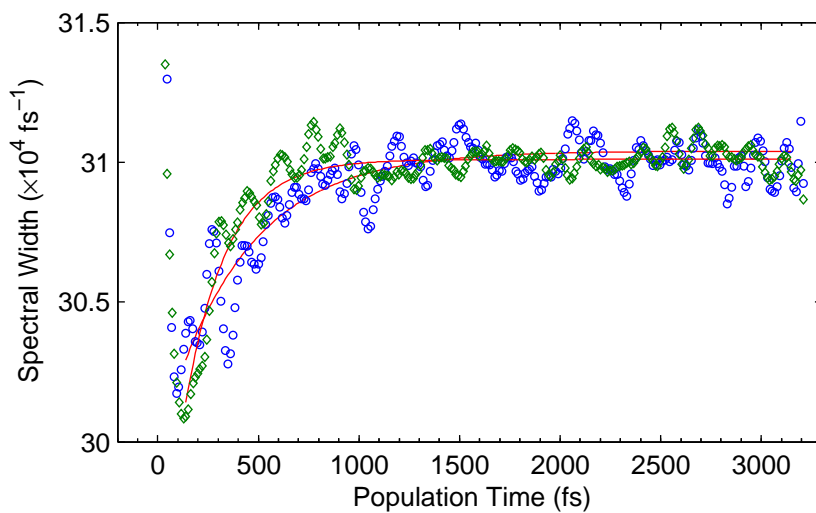


Figure 5.17: Two-colour transient grating spectral width signals for deoxy-Mb (circles) and MbCO (diamonds). Solid lines show the exponential component of matrix pencil method fit applied to population times $t_{23} > 130$ fs.

sured at 585 nm with a few exceptions. The higher frequency heme doming modes ($< 125 \text{ cm}^{-1}$) are dominant in both the deoxy-Mb and MbCO Fourier spectra rather than the lowest frequency doming modes. The relative amplitude of the sum and difference frequency coupled Fe-His/doming modes and the fundamental Fe-His modes is different. In the one-colour Fourier spectra the Fe-His mode dominated and the sum and difference frequency modes were approximately equal in amplitude and approximately 0.3 of the amplitude of the fundamental Fe-His mode, whereas in the deoxy-Mb and MbCO two-colour Fourier spectra the difference frequency mode is significantly larger than the sum frequency mode and comparable in amplitude to the Fe-His mode. The amplitudes of the Fe-His mode of deoxy-Mb and MbCO correspond well. The relative phase of the Fe-His mode for deoxy-Mb is approximately π shifted from the corresponding MbCO mode with an additional delay of approximately 20 fs (Fig. 5.18).

Table 5.6: Results of least squares fitting of two-colour transient grating intensity and spectral width for deoxy-Mb (Mb) and MbCO. Note the intensity was fit using a sum of exponentials convoluted with a Gaussian and the spectral width was fit using the matrix pencil method.

Para	A_1	τ_1 (fs)	A_2	τ_2 (fs)	A_3	A_0	t_0 (fs)
<u>TG Intensity</u>							
Mb	0.77	125	0.23	1500	...	0.70	24
MbCO	0.81	100	0.09	1500	0.10	1.00	-22
<u>Spectral Width</u>							
Mb	0.90	200					
MbCO	0.75	400					

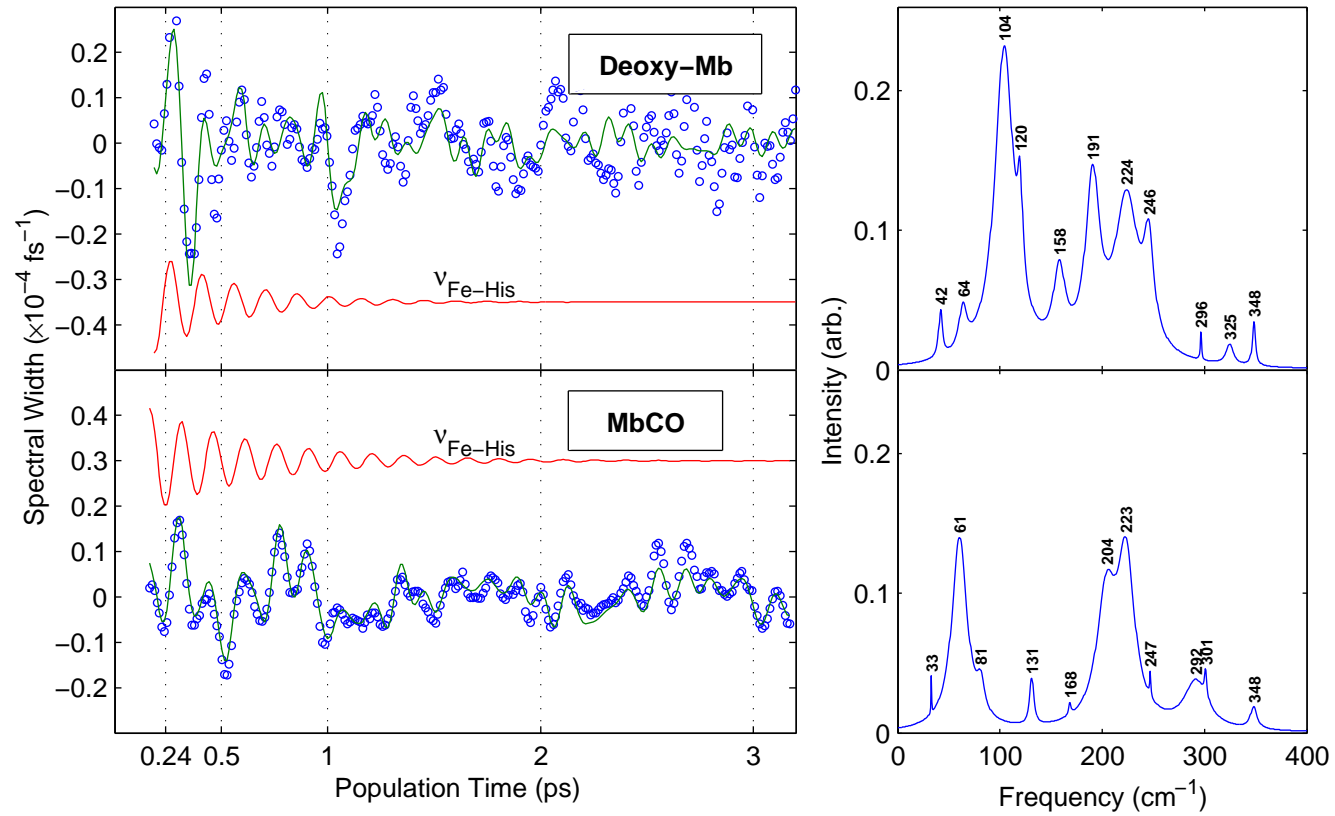


Figure 5.18: Two-colour transient grating spectral width signals with the exponential components removed for deoxy-Mb and MbCO. Matrix pencil method fits shown as solid lines and the retrieved Fe-His component included as an offset solid line. The retrieved Fourier spectra of the fit are shown in the right column.

5.6.2 Discussion

In a previously reported two-colour transient grating experiment the apparent population time delay in the signal was attributed to the time it takes for the initially created wavepacket to propagate from the doorway to the window state [41]. The rate of propagation is determined by the dynamic Stokes shift which is governed by the amount of homogeneous dephasing. In the case of a two-level system when the third laser pulse (window state) is tuned to the bottom (zero phonon) level of the excited state the two-colour transient grating intensity initially increases under the control of the dynamic Stokes shift and essentially asymptotes to a maximum if the excited state lifetime is long. In the two-colour results presented here for myoglobin where the window state is tuned near the transition of the second excited state the initial rise is assumed to be controlled by the dynamic Stokes shift and the fast finite lifetime of the first excited state. The delay in the MbCO signal could reflect the time it takes for the excited state wavepacket in the doorway state to migrate to the second excited state which has better spectral overlap with the window state (Fig. 5.10). The apparent 35 fs population time delay would be consistent with the proposed excited state lifetime of approximately 35 fs taken from literature [84,85]. This would also be consistent with the absence of the pulse width-limited decay that dominated the MbCO one-colour intensity signal. If the same theory is applied to the deoxy-Mb signal this would suggest that the excited state lifetime was considerably longer approximately 85 fs; however, this is more difficult to accept because the electronic structure of deoxy-Mb is not nearly as well understood. The absence of the *dip* in the two-colour spectral width signals compared to their corresponding one-colour signals also supports the suggestion that the two-colour signals are no longer sensitive to the dynamics

of the first excited states (Q-bands).

The first decay of the intensity and spectral signals is again attributed to the population lifetime of the second excited states ($5A''$ and $3A'$) which are proposed to be approximately 200 fs and 300-400 fs (recall intensity decays twice as fast as the population lifetime) for MbCO and deoxy-Mb, respectively. The change in spin state is again proposed to occur during the time the excited state population is residing in the second excited states. The second decay is attributed to the third state which is a combination of porphyrin ring-to-iron back charge transfer and protein/heme vibrational relaxation and occurs on a timescale of around 3 ps [65]. The offset in the MbCO, which is absent in the deoxy-Mb spectra, is attributed to the difference in the MbCO and photoproduct (deoxy-Mb) linear absorption spectra and would thus recover fully to zero upon reformation of the MbCO which is known to occur on the millisecond timescale.

The relative phase of the Fe-His modes can be used to estimate the time it takes for the Fe-CO bond to break. It is proposed from the signals that the Fe-CO dissociation occurs in around 25 fs. It is expected from the one-colour 585 nm signals that the MbCO Fe-His mode should be π out of phase relative to the deoxy-Mb mode because of the spin change occurring for MbCO. The deoxy-Mb signal here was delayed (taking into account the π phase difference) by approximately 20 fs; however, the deoxy-Mb signal is delayed approximately 45 fs from the MbCO signal (peak intensity difference). Thus, taking into account the delay of the deoxy-Mb signal and the π phase change, the MbCO Fe-His mode is delayed by approximately 25 fs. Whilst this is a rather indirect justification it agrees well with the phase of the Fe-His mode discussed above for the 585 nm intensity residuals (Fig. 5.9(inset)) and the previously proposed value of <25 fs [67]. The differences

between the two-colour and one-colour Fourier spectra are attributed to the 600 nm laser pulses coupling preferentially to higher energy vibrational levels than in the one-colour 585 nm experiment.

5.7 Summary

It has been shown that using one-colour and two-colour spectrally resolved photon echo (transient grating) spectroscopy, to varying degrees of certainty, that (i) MbCO photodissociates in approximately 25 fs, (ii) the excited state lifetime is approximately 35 fs, (iii) the intermediate decay of approximately 200 fs is a second excited state and not cooling of a hot photoproduct ground state, (iv) the longer lived (2-4 ps) relaxation is attributable to protein/heme vibrational relaxation and from the literature porphyrin ring-to-iron back charge transfer [65]. The photophysical properties of deoxy-Mb are similar to those found for MbCO after photodissociation although the population lifetimes for the two excited states are higher, approximately 80 fs and 300-400 fs, respectively.

There were clear advantages to spectrally resolving the measured photon echo (transient grating) signal. The additional information gained allowed for the determination of the time scale of the change in spin state of MbCO photodissociation. It was shown that the spectral width was able to provide similar information to the photon echo peak shift though, importantly, requiring only a single time axis to be scanned. By maintaining control of the coherence time it was shown that the relative amplitudes of the population and quantum beat signals in the spectral width signal could be changed. It was shown that by controlling the coherence time and measuring the spectra it may be possible to separate excited and ground state contributions to the signal though this requires further investigation.

Chapter 6

Summary and Future

Prospects

The aim of this thesis was to apply the technique of spectrally resolved two-colour photon echoes to study ultrafast processes in a biological molecular system. Specifically, we studied the mechanism and dynamics of the photodissociation reaction of carbonmonoxy myoglobin on a femtosecond timescale. The spectral resolution of the photon echo and related transient grating signals provides a great deal of additional information and when combined with two-colour excitation provides still more information and control. The spectral resolution of the scattered signal provides similar information to a photon echo peak shift experiment but requires only one time axis instead of two to be scanned that makes the experiment easier to perform. This also allows the coherence time axis to be used to control the relative contributions of population/overdamped modes and vibrational relaxation processes. The future success of two-colour and spectrally resolved techniques relies on the further characterisation of the signal response for

different systems and the development of theoretical models to extract the additional useful information.

The results calculated using the theoretical model show that the inverse linewidth of the spectrally resolved signal corresponds well with the temporal width of the photon echo pulse. Further investigation may reveal that this feature of the data could be used to determine fast processes in a similar manner to the time-gated photon echo technique. Moreover, least squares fitting of the inverse linewidth could be used to obtain a reasonable estimate of the underlying correlation function $M(t)$. However, the coupling strength and relaxation time estimates using the inverse linewidth were less accurate than those obtained using photon echo peak shift results. It is also unclear whether the inverse linewidth results can accurately determine the ratio of inhomogeneous to homogeneous broadening. Further experimental and theoretical studies into the relationship between the linewidth of the laser pulses and the linewidth of the scattered signals may resolve this potential limitation.

Application of the spectrally resolved transient grating technique to the laser dye rhodamine 101 in Chapter 4 showed additional advantages of measuring the signal spectrum. The absence of signal near the centre wavelength of the 575 and 590 nm laser pulses was used to unambiguously identify the existence of the intraband population relaxation and determine that it occurred on a pulse width-limited timescale. Moreover, the laser wavelength dependent signals could not be fitted only using the degenerate four wave mixing model but required the addition of contributions from a model describing coherent Raman scattering processes. The measurement of the signal spectrum in this case made identification of the Raman scattering contribution a case of comparing the overlap of the laser and signal spectra.

The identification of both these physical processes would have been more difficult had only the integrated intensity of the transient grating signal been measured.

The spectral resolution of the rhodamine 101 transient grating signal and the fitting of the centre frequency for different signal channels provided a means to separate ground and excited state decay times. The application of the spectrally resolved technique in the two-colour regime provided spectra rich in information. It was possible to determine the transit time for the propagating wavepacket and measure the effects of using pulses of high intensity, e.g., the AC-Stark shift induced by excitation on the blue side of the absorption maximum.

In Chapter 5 the technique was applied to a complex molecular system carbonmonoxy myoglobin in which a photochemical reaction takes place. It was shown the ultrafast change in spin state from the low spin bound state to the high spin unbound state occurred in the first 200 fs after excitation. Moreover, it was shown that the photophysics of photodissociation involved a second (intermediate) excited state with a lifetime of around 200 fs for MbCO and not vibrational cooling of a hot ground state on a similar timescale. Other photophysical time scales were also estimated: the Fe-CO bond breakage occurred within 25 fs and the lifetime of the Q-band levels was 35 fs. These are significant results given the laser pulses were approximately 85 fs FWHM.

Furthermore, there were clear advantages to spectrally resolving the measured signal. The additional information gained allowed (i) the determination of the time scale for the change in spin state of MbCO photodissociation; (ii) provided similar information to the photon echo peak shift while only requiring a single time axis to be scanned; (iii) the control, by varying coher-

ence time, of the relative amplitudes of population and quantum beat signals in the spectral width signal; (iv) the possibility of separating ground and excited state contributions to the signal, through control of the coherence time and measuring the spectra.

The advantages of extending existing nonlinear spectroscopic techniques through the addition of a spectrometer are numerous including the ability to determine the temporal width of the photon echo signal pulse without the addition of another experimental time axis and nonlinear crystal (a time consuming and technically intricate measurement to perform, e.g., phase-matching for every laser wavelength change); having control of the coherence time as a free experimental variable rather than it being required to generate the experimental observable, as is the case for peak shift scans; and provides a more detailed picture for analysing the photophysics and photochemistry under investigation.

In future it would be interesting to further investigate the correspondence between the inverse linewidth of the transient grating spectra and the temporal width of the photon echo signal pulse. A good system for performing this study would be semi conductor nanocrystals of sufficiently high quality that they essentially behave as two-level systems with few vibrational degrees of freedom. This study would involve measuring the transient grating spectra and the temporal width of the scattered signal. To investigate the sensitivity of the technique for determining the effect of different protein environments on a chromophore or reactive species it would be interesting to study a system with different point mutations around the area of interest. A good target for this type of study is the abundant wild type and mutant fluorescent proteins currently available. Finally, it is encouraging to see a raft of new theoretical packages that can calculate time-dependent

wavefunctions for various electronic potentials. These hold promise of being modified into a form capable of determining the signal response of many different nonlinear signals.

Bibliography

- [1] <http://www.uh.edu/engines/epi658.htm>.
- [2] <http://www.med.virginia.edu/hs-library/historical/classics/Haller.html>.
- [3] W. L. Marmelzat, "History of Dermatologic Surgery. From the Beginnings to Late Antiquity," *Clin Dermatol.* **5**(4), pp. 1–10, 1987.
- [4] A. Haller, *First Lines of Physiology*, New York: Johnson Reprint Corp., this is a reprint of the 1786 english ed., 1966.
- [5] E. Hintsche, and A. Haller, *Dictionary of Scientific Biography*, Chas. Scribner's Sons, c.c. gilespie ed., 1970-1980.
- [6] S. S. Gross and P. Lane, "Physiological Reactions of Nitric Oxide and Hemoglobin: A Radical Rethink," *Proc. Natl. Acad. Sci. U.S.A.* **96**(18), pp. 9967–9969, 1999.
- [7] Y. Nagasawa, A. Watanabe, H. Takikawa, T. Okada, "Solute Dependence of Three Pulse Photon Echo Peak Shift Measurements in Methanol Solution," *J. Phys. Chem. A* **107**(5), pp. 632–641, 2003.
- [8] T. Joo, Y. Jia, J-Y. Yu, M. J. Lang and G. R. Fleming, "Third-Order Nonlinear Time Domain Probes of Solvation Dynamics," *J. Chem. Phys.* **104**(16), pp. 6089–6108, 1996.

- [9] X. J. Jordanides, M. J. Lang, X. Song and G. R. Fleming, "Solvation Dynamics in Protein Environments Studied by Photon Echo Spectroscopy," *J. Phys. Chem. B* **103**(37), pp. 7995–8005, 1999.
- [10] Q-H. Xu, G. D. Scholes, M. Yang, G. R. Fleming, "Probing Solvation and Reaction Coordinates of Ultrafast Photoinduced Electron-Transfer Reactions Using Nonlinear Spectroscopies: Rhodamine 6G in Electron-Donating Solvents," *J. Phys. Chem. A* **103**(49), pp. 10348–10358, 1999.
- [11] W. P. deBoeij, M. S. Pshenichnikov and D. A. Wiersma, "Ultrafast Solvation Dynamics Explored by Femtosecond Photon Echo Spectroscopies," *Annu. Rev. Phys. Chem.* **49**, pp. 99–123, 1998.
- [12] H. Bursing, S. Kundu, P. Vohringer, "Solvation Dynamics at Aqueous Lipid-Membrane Interfaces Explored by Temperature-Dependent 3-Pulse-Echo Peak Shifts: Influence of the Lipid Polymorphism," *J. Phys. Chem. B* **107**(10), pp. 2404–2414, 2003.
- [13] D. P. Zhong, S. K. Pal and A. H. Zewail, "Femtosecond Studies of Protein - DNA Binding and Dynamics: Histone I," *ChemPhysChem* **2**(4), pp. 219–227, 2001.
- [14] C. J. Bardeen, S. J. Rosenthal and C. V. Shank, "Ultrafast Solvation Processes in Polar Liquids Probed with Large Organic Molecules," *J. Phys. Chem. B* **103**(49), pp. 10506–10516, 1999.
- [15] L. D. Book and N. F. Scherer, "Wavelength-Resolved Stimulated Photon Echoes: Direct Observation of Ultrafast Intramolecular Vibrational Contributions to Electronic Dephasing," *J. Chem. Phys.* **111**(3), pp. 792–795, 1999.

- [16] D. S. Larsen, K. Ohta, Q-H. Xu, M. Cyrier and G. R. Fleming, "Influence of Intramolecular Vibrations in Third-Order, Time Domain Resonant Spectroscopies. I. Experiments," *J. Chem. Phys.* **114**(18), pp. 8008–8019, 2001.
- [17] Y. R. Shen, *The Principle of Nonlinear Optics*, Wiley: New York, 1984.
- [18] R. W. Boyd, *Nonlinear Optics*, Academic Press: San Diego, CA, 1992.
- [19] S. Mukamel, *Principles of Nonlinear Optical Spectroscopy*, vol. 6 of *Oxford Series in Optical and Imaging Sciences*, Oxford University Press: New York, 1995.
- [20] S. Mukamel, "Multidimensional Femtosecond Correlation Spectroscopies of Electronic and Vibrational Excitations," *Annu. Rev. Phys. Chem.* **51**, pp. 691–729, 2000.
- [21] W. P. deBoeij, M. S. Pshenichnikov and D. A. Wiersma, "On the Relation Between the Echo-Peak Shift and Brownian-Oscillator Correlation Function," *Chem. Phys. Lett.* **253**(1-2), pp. 53–60, 1996.
- [22] M. Cho, M., J.-Y Yu., T. Joo, Y. Nagasawa, S. A. Passino, G. R. Fleming, "The Integrated Photon Echo and Solvation Dynamics," *J. Phys. Chem.* **100**(29), pp. 11944–11953, 1996.
- [23] W. Zinth and W. Kaiser, *Topics in Applied Physics*, vol. 60, ch. 6: Ultrafast Coherence Spectroscopy, pp. 235–277. Springer-Verlag: Heidelberg, 1988.
- [24] K. Ohta, D. S. Larsen, M. Yang and G. R. Fleming, "Influence of Intramolecular Vibrations in Third-Order, Time Domain Resonant

- Spectroscopies. II. Numerical Calculations,” *J. Chem. Phys.* **114**(18), pp. 8020–8039, 2001.
- [25] Ryan B. Williams, *Condensed Phase Dynamics Elucidated by Linear and Nonlinear Vibrational Spectroscopy*. PhD thesis, Cornell University, 2001.
- [26] J. T. Fourkas, “Higher-Order Optical Correlation Spectroscopy in Liquids,” *Annu. Rev. Phys. Chem.* **54**, pp. 17–40, 2002.
- [27] J. Erland and I. Balslev, “Theory of Quantum Beat and Polarization Interference in Four-Wave Mixing,” *Phys. Rev. A* **48**(3), pp. R1765–R1768, 1993.
- [28] J. Erland, K.-H. Pantke and V. Mizeikis, “Spectrally Resolved Four-Wave Mixing in Semiconductor: Influence of Inhomogeneous Broadening,” *Phys. Rev. B* **50**(20), pp. 15047–15055, 1994.
- [29] J. Erland, V. G. Lyssenko and J. M. Hvam, “Optical Coherent Control in Semiconductors: Fringe Contrast and Inhomogeneous Broadening,” *Phys. Rev. A* **63**(15), pp. 155317–155317, 2001.
- [30] B. I. Grimberg, V. V. Lozovoy, M. Dantus and S. Mukamel, “Ultrafast Nonlinear Spectroscopy Techniques in the Gas Phase and their Density Matrix Representation,” *J. Phys. Chem. A* **106**(5), pp. 697–718, 2002.
- [31] V. V. Lozovoy, B. I. Grimberg, E. I. Pastirk and M. Dantus, “Femtosecond Spectrally Dispersed Three-Pulse Four-Wave Mixing: The Role of Sequence and Chirp in Controlling Intramolecular Dynamics,” *J. Raman Spec.* **31**(1-2), pp. 41–49, 2000.
- [32] L. V. Dao, C. N. Lincoln, R. M. Lowe and P. Hannaford, “Spectrally Resolved Two-Colour Three-Pulse Photon Echo Studies of Vibra-

- tional Dynamics of Molecules,” *Physica B-Condensed Matter* **327**(1), pp. 123–128, 2003.
- [33] L. V. Dao, C. N. Lincoln, R. M. Lowe and P. Hannaford, “Spectrally Resolved Two-Colour Three-Pulse Photon Echoes: Study of Ground and Excited State Dynamics in Molecules,” *J. Chem. Phys.* **120**(18), pp. 8434–8442, 2004.
- [34] N. Demirdöven, M. Khalil, O. Golonzka and A. Tokmakoff, “Correlation Effects in the Two-Dimensional Vibrational Spectroscopy of Coupled Vibrations,” *J. Phys. Chem. A* **105**(34), pp. 8025–8030, 2001.
- [35] L. D. Book, A. E. Ostafin, N. Ponomarenko, J. R. Norris and N. F. Scherer, “Exciton Delocalization and Initial Dephasing Dynamics of Purple Bacteria LH2,” *J. Phys. Chem. B* **104**(34), pp. 8295–8307, 2000.
- [36] M. Dantus, “Coherent Nonlinear Spectroscopy: From Femtosecond Dynamics to Control,” *Annu. Rev. Phys. Chem.* **52**, pp. 639–679, 2001.
- [37] K. Duppen, D. P. Weitekamp and D. A. Wiersma, “Two-Colour Picosecond Stimulated Photon Echoes in Solids,” *Chem. Phys. Lett.* **108**(6), pp. 551–554, 1984.
- [38] K. Duppen, D. P. Weitekamp and D. A. Wiersma, “Picosecond Tri-Transition and Two-Colour Photon Echoes in a Doped Molecular Solid,” *Chem. Phys. Lett.* **106**(3), pp. 147–152, 1984.
- [39] M. Yang and G. R. Fleming, “Two-Colour Three-Pulse Photon Echoes as a Probe of Electronic Coupling in Molecular Complexes,” *J. Chem. Phys.* **110**(6), pp. 2983–2990, 1999.

- [40] R. Agarwal, B. S. Prall, A. H. Rizvi, M. Yang and G. R. Fleming, "Two-Color Three Pulse Photon Echo Peak Shift Spectroscopy," *J. Chem. Phys.* **116**(14), pp. 6243–6252, 2002.
- [41] K. Kwak, M. Cho, G. R. Fleming, R. Agarwal and B. S. Prall, "Two-Colour Transient Grating Spectroscopy of a Two-Level System," *Bull. Korean. Chem. Soc.* **24**(8), pp. 1069–1074, 2003.
- [42] G. R. Fleming, *Chemical Applications of Ultrafast Spectroscopy*, vol. 13 of *The International Series of Monographs on Chemistry*, Oxford University Press: New York, 1986.
- [43] Y. Y. Lin, P. Hodgkinson, M. Ernst and A. Pines, "A Novel Detection-Estimation Scheme for Noisy NMR Signals: Applications to Delayed Acquisition Data," *Journal of Magnetic Resonance* **128**(1), pp. 30–41, 1997.
- [44] R. Kumaresan, D. W. Tufts, "Estimating the Parameters of Exponentially Damped Sinusoids and Pole-Zeros Modeling in Noise," *IEEE Trans. Acoust. Speech Signal Processing* **30**(6), pp. 833–840, 1982.
- [45] A. Marcano O. and I. Urdaneta, "Fluorescence Quantum Yield of Rhodamine 101 in the Presence of Absorption Saturation," *Appl. Phys. B* **72**, pp. 207–213, 2001.
- [46] B. S. Neporent and A. G. Spiro, "4-Photon Scattering in Some Rhodamine Solutions at Different Pump Powers," *Opt. Spectrosc.* **78**(1), pp. 31–36, 1995.
- [47] M. Takayanagi, H Hamaguchi and M. Tasumi, "Probe-Frequency Dependence of the Resonant Inverse Raman Band Shape," *J. Chem. Phys.* **89**(7), pp. 3945–3950, 1988.

- [48] T. Siebert, M. Schmitt, T. Michelis, A. Materny and W. Kiefer, “CCD Broadband Detection Technique for the Spectral Characterisation of the Inhomogeneous Signal in Femtosecond Time-Resolved Four-wave Mixing Spectroscopy,”
- [49] A. Materny, T. Chen, M. Siebert, A. Vierheilg, V. Engel and W. Kiefer, “Wave Packet Dynamics in Different Electronic States Investigated by Femtosecond Time-Resolved Four-Wave-Mixing Spectroscopy,” *Appl. Phys. B* **71**(3), pp. 299–317, 2000.
- [50] J.-S. Park and T. Joo, “Nuclear Dynamics in Electronic Ground and Excited States Probed by Spectrally Resolved Four Wave Mixing,” *J. Chem. Phys.* **116**(24), pp. 10801–10808, 2002.
- [51] C. Cohen-Tannoudji, “Effect of a Non-Resonant Irradiation on Atomic Energy Levels - Application to Light-Shifts in Two-Photon Spectroscopy and to Perturbation of Rydberg States,” *Metrologia* **13**(3), pp. 161–166, 1977.
- [52] A. Marcano O., N. Melikechi and G. Verde, “Shift of the Absorption Spectrum of Organic Dyes Due to Saturation,” *J. Chem. Phys.* **113**(14), pp. 5830–5835, 2000.
- [53] <http://nobelprize.org/chemistry/laureates/1962/index.html>.
- [54] M. F. Perutz, “X-ray Analysis of Haemoglobin,” *Nature* **149**, pp. 491–496, 1942.
- [55] M. F. Perutz, “Crystal Structure of Oxyhaemoglobin,” *Nature* **152**, pp. 324–329, 1942.

- [56] J. C. Kendrew and M. F. Perutz, "A Comparative X-ray Study of Foetal and Adult Sheep Haemoglobins," *Proc. Roy. Soc. London* **A194**, pp. 375–398, 1948.
- [57] L. Bragg, J. C. Kendrew and M. F. Perutz, "Polypeptide Chain Configurations in Crystalline Proteins," *Proc. Roy. Soc. London* **A203**, pp. 321–357, 1950.
- [58] J. L. Martin, A. Migus, C. Poyart, Y. Lecarpentier, A. Antonettie, and A. Orszag, "Femtosecond Photodissociation and Picosecond Recombination of O₂ in Myoglobin: A Plausible Explanation for the Low Quantum Yield in MbO₂," *Biochem. Biophys. Res. Commun.* **107**(3), pp. 803–810, 1982.
- [59] J. L. Martin, A. Migus, C. Poyart, Y. Lecarpentier, R. Astier and A. Antonettie, "Femtosecond Photolysis of CO-Ligated Protoheme and Hemoproteins: Appearance of Deoxy Species with a 350-fsec Time Constant," *Proc. Natl. Acad. Sci. U.S.A.* **80**(1), pp. 173–177, 1983.
- [60] J. L. Martin, A. Migus, C. Poyart, Y. Lecarpentier, R. Astier and A. Antonettie, "Spectral Evidence for Sub-Picosecond Iron Displacement After Ligand Detachment from Hemoproteins by Femtosecond Light Pulses," *The EMBO J.* **2**(10), pp. 1815–1819, 1983.
- [61] L. Zhu, T. J. Sage and P. M. Champion, "Observation of Coherent Reaction Dynamics in Heme Proteins," *Science* **266**(5185), pp. 629–632, 1994.
- [62] J. W. Petrich, C. Poyart and J. L. Martin, "Photophysics and Reactivity of Heme Proteins: A Femtosecond Absorption Study of

- Hemoglobin, Myoglobin and Protoheme,” *Biochem.* **27**(11), pp. 4049–4060, 1988.
- [63] Y. Kholodenko, M. Volk, E. Gooding and R. M. Hochstrasser, “Energy Dissipation and Relaxation Processes in Deoxy Myoglobin After Photoexcitation in the Soret Region,” *Chem. Phys.* **259**(1), pp. 71–87, 2000.
- [64] F. Rosca, A. T. N. Kumar, X. Ye, T. Sjödin, A. A. Demidov and P. M. Champion, “Investigations of Coherent Vibrational Oscillations in Myoglobin,” *J. Phys. Chem. A* **104**(18), pp. 4280–4290, 2000.
- [65] S. Franzen, L. Kiger, C. Poyart and J.-L. Martin, “Heme Photolysis Occurs by Ultrafast Excited State Metal-to-Ring Charge Transfer,” *Biophys. J.* **80**(5), pp. 2372–2385, 2001.
- [66] X. Ye, A. Demidov and P. M. Champion, “Measurement of the Photodissociation Quantum Yields of MbNO and MbO₂ and the Vibrational Relaxation of the Six-Coordinate Heme Species,” *J. Am. Chem. Soc.* **124**(20), pp. 5914–5924, 2002.
- [67] M. R. Armstrong, J. P. Ogilvie, M. L. Cowan, A. M. Nagy and R. J. Miller, “Observation of the Cascaded Atomic-to-Global Length Scales Driving Protein Motion,” *Proc. Natl. Acad. Sci. U.S.A.* **100**(9), pp. 4990–4994, 2003.
- [68] M. Halder, K. Das, P. K. Chowdhury, S. Kundu, M. S. Hargrove and J. Petrich, “A Comparative Femtosecond Coherence Study of the Unligated Monomeric Hemeproteins Myoglobin and Leghemoglobin,” *J. Phys. Chem. B* **107**(36), pp. 9933–9938, 2003.

- [69] X. Ye, A. Demidov, F. Rosca, W. Wang, A. Kumar, D. Ionascu, L. Zhu, D. Barrick, D. Wharton and P. M. Champion, “Investigations of Heme Protein Absorption Line Shapes, Vibrational Relaxation, and Resonance Raman Scattering on Ultrafast Time Scales,” *J. Phys. Chem. A* **107**(40), pp. 8156–8165, 2003.
- [70] T. Polack, J. P. Ogilvie, S. Franzen, M. H. Vos, M. Joffe, J. L. Martin, A. Alexandrou, “CO Vibration as a Probe of Ligand Dissociation and Transfer in Myoglobin,” **93**(1), pp. 018102–1–4, 2004.
- [71] J. W. Petrich, J. L. Martin, D. Houde, C. Poyart and A Orszag, “Time-Resolved Raman Spectroscopy with Subpicosecond Resolution: vibrational Cooling and Delocalization of Strain Energy in Photodissociated (Carbonmonoxy)hemoglobin,” *Biochem.* **26**(24), pp. 7914–7923, 1987.
- [72] T. Kitagawa, N. Haruta and Y. Mizutani, “Time-Resolved Resonance Raman Study of Ultrafast Structural Relaxation and Vibrational Cooling of Photodissociated Carbonmonoxy Myoglobin,” *Biopolymers(Biospectroscopy)* **67**, pp. 207–213, 2002.
- [73] G. D. Goodno and R. J. D. Miller, “Femtosecond Heterodyne-Detected Four-Wave-Mixing Studies of Deterministic Protein Motions. 1. Theory and Experimental Technique of Diffractive Optics-Based Spectroscopy,” *J. Phys. Chem. A* **103**(49), pp. 10619–10629, 1999.
- [74] G. D. Goodno, V. Astinov and R. J. D. Miller, “Femtosecond Heterodyne-Detected Four-Wave-Mixing Studies of Deterministic Protein Motions. 2. Protein Response,” *J. Phys. Chem. A* **103**(49), pp. 10630–10643, 1999.

- [75] R. Jimenez and F. E. Romesberg, “Excited State Dynamics and Heterogeneity of Folded and Unfolded States of Cytochrome *c*,” *J. Phys. Chem. B* **106**(35), pp. 9172–9180, 2002.
- [76] M. D. Fayer, “Fast Protein Dynamics Probed with Infrared Vibrational Echo Experiments,” *Annu. Rev. Phys. Chem.* **52**, pp. 315–356, 2001.
- [77] K. D. Rector, D. E. Thompson, K. Merchant, M. D. Fayer, “Dynamics in Globular Proteins: Vibrational Echo Experiments,” **316**(1-2), pp. 122–128, 2000.
- [78] B. L. McClain, I. J. Finkelstein, M. D. Fayer, “Dynamics of Hemoglobin in Human Erythrocytes and in Solution: Influence of Viscosity Studied by Ultrafast Vibrational Echo Experiments,” *J. Am. Chem. Soc.* **126**(48), pp. 15702–15710, 2004.
- [79] F. Schotte, M. H. Lim, T. A. Jackson, A. V. Smirnov, J. Soman, J. S. Olson, G. N. Phillips, M. Wulff, P. A. Anfinrud, “Watching a Protein as it Functions with 150-ps Time-Resolved X-ray Crystallography,” *Science* **300**(5627), pp. 1944–1947, 2003.
- [80] G. Hummer, F. Schotte, P. A. Anfinrud, “Unveiling Functional Protein Motions with Picosecond X-ray Crystallography and Molecular Dynamics Simulations,” *Proc. Natl. Acad. Sci. U.S.A.* **101**(43), pp. 15330–15334, 2004.
- [81] H. Frauenfelder, B. H. McMahon, R. H. Austin, K. Chu and J. T. Groves, “The Role of Structure, Energy Landscape, Dynamics, and Allostery in the Enzymatic Function of Myoglobin,” *Proc. Natl. Acad. Sci. U.S.A.* **98**(5), p. 23702374, 2001.

- [82] F. Rosca, A. T. N. Kumar, D. Ionascu, T. Sjodin, A. A. Demidov and P. M. Champion, “Wavelength Selective Modulation in Femtosecond Pump-Probe Spectroscopy and its Application to Heme Proteins,” *J. Chem. Phys.* **114**(24), pp. 10884–10898, 2001.
- [83] A. T. N. Kumar, F. Rosca, A. Widom and P. M. Champion, “Investigations of Amplitude and Phase Excitation Profiles in Femtosecond Coherence Spectroscopy,” *J. Chem. Phys.* **114**(2), pp. 701–724, 2001.
- [84] F. Rosca, A. T. N. Kumar, D. Ionascu, X. Ye, A. A. Demidov, T. Sjodin, D. Wharton, D. Barrick, S. G. Sligar, T. Yonetani and P. M. Champion, “Investigation of Anharmonic Low-Frequency Oscillations in Heme Proteins,” *J. Phys. Chem. A* **106**(14), pp. 3540–3552, 2002.
- [85] P. M. Champion, F. Rosca, D. Ionascu, W. Cao and X. Ye, “Rapid Timescale Processes and the Role of Electronic Surface Coupling in the Photolysis of Diatomic Ligands from Heme Proteins,” *Faraday Discussions* **127**, pp. 123–135, 2004.
- [86] B. D. Dunietz, A. Dreuw, M. Head-Gordon, “Initial Steps of the Photodissociation of the CO Ligated Heme Group,” *J. Phys. Chem. B* **107**(23), pp. 5623–5629, 2003.
- [87] Lubert Stryer, *Biochemistry 4th ed.*, W. H. Freeman and Company, 1995.
- [88] G. S. Kachalova, A. N. Pepov and H. D. Bartunik, “A Steric Mechanism for Inhibition of CO Binding to Heme Proteins,” *Science* **284**(5413), pp. 473–476, 1999.

- [89] J. Vojtechovsky, I. Schlichting, K. Chu and R. M. Sweet, “Crystal Structures of Myoglobin-Ligand Complexes at Near-Atomic Resolution,” *Biophys. J.* **77**(4), pp. 2153–2174, 1999.
- [90] T. Uno, R. Sakamoto, Y. Tommisugi, Y. Ishikawa and A. J. Wilkinson, “Inversion of Axial Coordination in Myoglobin to Create a “Proximal” Ligand Binding Pocket,” *Biochem.* **42**(34), pp. 10191–10199, 2003.
- [91] S. Hu, K. M. Smith and T. G. Spiro, “Assignment of Protoheme Resonance Raman Spectrum by Heme Labeling in Myoglobin,” *J. Am. Chem. Soc.* **118**(50), pp. 12638–12646, 1996.
- [92] S. Takahashi, J. Wang and D. L. Rousseau, “Heme-Heme Oxygenase Complex: Structure and Properties of the Catalytic Site from Resonance Raman Scattering,” *Biochem.* **33**(18), pp. 5531–5538, 1994.
- [93] B. K. Rai, S. M. Durbin, E. W. Prohofsky, T. J. Sage, M. K. Ellison, W. R. Scheidt, W. Sturhahn and E. E. Alp, “Iron Normal Mode Dynamics in a Porphyrin-Imidazole Model for Deoxyheme Proteins,” *Phys. Rev. E* **66**(5), p. 05190(12), 2002.
- [94] B. K. Rai, S. M. Durbin, E. W. Prohofsky, T. J. Sage, M. K. Ellison, A. Roth, W. R. Scheidt, W. Sturhahn and E. E. Alp, “Direct Determination of the Complete Set of Iron Normal Modes in a Porphyrin-Imidazole model for Carbonmonoxy-Heme Proteins: [Fe(TPP)(CO)(1-MeIm)],” *J. Am. Chem. Soc.* **125**(23), pp. 6927–6936, 2003.
- [95] S. Franzen, K. Fritsch and S. H. Brewer, “Experimental Observation of Anharmonic Coupling of the Heme-Doming and Iron-ligand Out-of-

- Plane Vibrational Modes Confirmed by Density Functional Theory,” *J. Phys. Chem. B* **106**(44), pp. 11641–11646, 2002.
- [96] S. S. Stavrov, “Correct Interpretation of Heme Protein Spectra Allows Distinguishing Between the Heme and the Protein Dynamics,” *Biopolymers* **74**(1-2), pp. 37–40, 2004.
- [97] M. Korostishevsky, Z. Zaslavsky and S. S. Stavrov, “Temperature dependence of the iron-histidine resonance Raman band of deoxyheme proteins: Anharmonic coupling versus distribution over taxonomic conformational substates,” *Biophys. J.* **86**(1), pp. 656–659, 2004.
- [98] E. Antonini and M. Brunori, *Hemoglobin and Myoglobin in their Reaction with Ligands*, North-Holland: Amsterdam, 1971.
- [99] B. I. Greene, R. M. Hochstrasser, R. B. Weisman, W. A. Eaton, “Spectroscopic Studies of Oxy- and Carbonmonoxyhemoglobin After Pulsed Optical Excitation,” *Proc. Natl. Acad. Sci. U.S.A.* **75**(11), pp. 5255–5259, 1978.
- [100] F. D. Angelis, R. Car, T. G. Spiro, “Role of Ligand Bending in the Photodissociation of O₂ vs CO-heme: A Time-Dependent Density Functional Study,” *J. Am. Chem. Soc.* **125**(51), pp. 15710–15711, 2003.
- [101] Y. Mizutani and T. Kitagawa, “Ultrafast Structural Relaxation of Myoglobin Following Photodissociation of Carbon Monoxide Probed by Time-Resolved Resonance Raman Spectroscopy,” *J. Phys. Chem. B* **105**(44), pp. 10992–10999, 2001.
- [102] M. Yang, K Ohta and G. R. Fleming, “Three-Pulse Photon Echoes for Model Reactive Systems,” *J. Chem. Phys.* **110**(21), pp. 10243–10252, 1999.

Appendix A

Example Code

A.1 RunP3_Calc

```
clear tic;
% Matlab script for calculation third-order polrisation using the
% multimode Brownian oscillator model. Note the file P3_t_t12_t23.m
% is for unordered pulses, i.e., the temporal width of the laser is
% NOT short compared to the coherence time (t12) or the population
% time (t23).
% Author: Craig Lincoln 2005
% References:
% S. Mukamel, Principles of Nonlinear Optical Spectroscopy, Oxford
% University Press: New York, 1995.
%
%%%%%%%%%%%%%%%%%%%%%%%%%%%%%%%%%%%%%%%%%%%%%%%%%%%%%%%%%%%%%%%%%%%%%%%%
% Parameters
%%%%%%%%%%%%%%%%%%%%%%%%%%%%%%%%%%%%%%%%%%%%%%%%%%%%%%%%%%%%%%%%%%%%%%%%
% BO Inputs
% wj = 0 = Gaussian Mode
%     = 1 = Overdamped Mode
%     = 2 = Const. Mode (Inhomogeneous Broadening)
%     = 2*pi*(frequency in wavenumbers)/33356.4 = Underdamped Mode
Lfrac = [ 0.37 0.13 0.26 0.24 ];
Lfrac = Lfrac / sum(Lfrac);
Lambda = 216; %cm-1
L = Lfrac * (2e-15*pi*3e10/(1/Lambda));
wj = [ 1 1 2 (2e-15*pi*3e10/(1/154)) ];
gj = 1./ [ 140 5000 1 190 ]; %fs
T = 300; %Kelvin

% Temporal Variables (fs)
t23 = [[-50:10:60] [80:20:2000]];
t12 = 0; dt = 10;
Nopts = 31; %eg, 127 255 511 1023
Noptsint = 18;
t = [-(dt*(ceil(Nopts*1/3)+1)):dt:(dt*(floor(Nopts*2/3)-1))];
width = 80/2.3548; %Pulse Width FWHM (fs)

% Spectral Properties of system and lasers
% spec = [weg om1 om2 om3] in nm
spec = [ 500 511.5 511.5 511.5 ];

%%%%%%%%%%%%%%%%%%%%%%%%%%%%%%%%%%%%%%%%%%%%%%%%%%%%%%%%%%%%%%%%%%%%%%%%
% Call Calculation
%%%%%%%%%%%%%%%%%%%%%%%%%%%%%%%%%%%%%%%%%%%%%%%%%%%%%%%%%%%%%%%%%%%%%%%%
```

```
[ P3t,om3,weg,D2 ] = ...  
P3_t_t12_t23(L,wj,gj,T,t23,t12,dt,t,width,spec,Noptsint);  
  
toc  
filename = [ pwd '\Autosave.mat'];  
save(filename);
```

A.2 P3_t_t12_t23.m

```

function [ P3t,om3,weg,D2 ] = ...
P3_t_t12_t23_allR_nm(L,wj,gj,T,t23,t12,dt,t,width,spec,Noptsint);
% Physical Const.
hbar = 0.6582122; %eVfs
kb = 8.617385e-5; %eVK-1

% D2
D2 = 2*kb*T*L/hbar;

% Spectral Properties
weg = 2*pi*3e2/(spec(1));
om1 = 2*pi*3e2/(spec(2));
om2 = 2*pi*3e2/(spec(3));
om3 = 2*pi*3e2/(spec(4));

%%%%%%%%%%%%%%%%%%%%%%%%%%%%%%%%%%%%%%%%%%%%%%%%%%%%%%%%%%%%%%%%%%%%%%%%
%%%%%%%%%%%%%%%%%%%%%%%%%%%%%%%%%%%%%%%%%%%%%%%%%%%%%%%%%%%%%%%%%%%%%%%%
% Calculations
%%%%%%%%%%%%%%%%%%%%%%%%%%%%%%%%%%%%%%%%%%%%%%%%%%%%%%%%%%%%%%%%%%%%%%%%
%%%%%%%%%%%%%%%%%%%%%%%%%%%%%%%%%%%%%%%%%%%%%%%%%%%%%%%%%%%%%%%%%%%%%%%%
indt = find(t>=0);
indt12 = find(t12>=0);
indt23 = find(t23>=0);

t3 = [0:dt:((Noptsint*dt)+max(t(indt)))];
t2 = [0:dt:((Noptsint*dt)+max(t23(indt23)))];
t1 = [0:dt:((Noptsint*dt)+max(t12(indt12)))];
[t1int,t2int,t3int] = meshgrid(t1,t2,t3);

[rer1and4,imr1,imr4] = RIRIV(kb,T,hbar,wj,gj,t1int,t2int,t3int,L,D2);
[rer2and3,imr2,imr3] = RIIRIII(kb,T,hbar,wj,gj,t1int,t2int,t3int,L,D2);

echo = zeros(length(t),length(t23),length(t12));

for coh = 1:length(t12)
for pop = 1:length(t23)
for a = 1:length(t)

clear t3 t2 t1 t3int t2int t1int
if t(a) < 0 & t12(coh) < 0 & t23(pop) < 0
t3 = [0:dt:((Noptsint*dt))];
t2 = [0:dt:((Noptsint*dt))];
t1 = [0:dt:((Noptsint*dt))];

```

```

        [t1int,t2int,t3int] = meshgrid(t1,t2,t3);

elseif t(a) < 0 & t12(coh) < 0
    t3 = [0:dt:((Noptsint*dt))];
    t2 = [0:dt:((Noptsint*dt)+t23(pop))];
    t1 = [0:dt:((Noptsint*dt))];
    [t1int,t2int,t3int] = meshgrid(t1,t2,t3);

elseif t(a) < 0 & t23(pop) < 0
    t3 = [0:dt:((Noptsint*dt))];
    t2 = [0:dt:((Noptsint*dt))];
    t1 = [0:dt:((Noptsint*dt)+t12(coh))];
    [t1int,t2int,t3int] = meshgrid(t1,t2,t3);

elseif t12(coh) < 0 & t23(pop) < 0
    t3 = [0:dt:((Noptsint*dt)+t(a))];
    t2 = [0:dt:((Noptsint*dt))];
    t1 = [0:dt:((Noptsint*dt))];
    [t1int,t2int,t3int] = meshgrid(t1,t2,t3);

elseif t(a) < 0
    t3 = [0:dt:((Noptsint*dt))];
    t2 = [0:dt:((Noptsint*dt)+t23(pop))];
    t1 = [0:dt:((Noptsint*dt)+t12(coh))];
    [t1int,t2int,t3int] = meshgrid(t1,t2,t3);

elseif t12(coh) < 0
    t3 = [0:dt:((Noptsint*dt)+t(a))];
    t2 = [0:dt:((Noptsint*dt)+t23(pop))];
    t1 = [0:dt:((Noptsint*dt))];
    [t1int,t2int,t3int] = meshgrid(t1,t2,t3);

elseif t23(pop) < 0
    t3 = [0:dt:((Noptsint*dt)+t(a))];
    t2 = [0:dt:((Noptsint*dt))];
    t1 = [0:dt:((Noptsint*dt)+t12(coh))];
    [t1int,t2int,t3int] = meshgrid(t1,t2,t3);

else
    t3 = [0:dt:((Noptsint*dt)+t(a))];
    t2 = [0:dt:((Noptsint*dt)+t23(pop))];
    t1 = [0:dt:((Noptsint*dt)+t12(coh))];
    [t1int,t2int,t3int] = meshgrid(t1,t2,t3);
end

```

```

[m n o] = size(t1int);
echo3 = zeros(size(t1int));
echo2 = zeros(1,length(t2),length(t3));
echo1 = zeros(1,1,length(t3));

echo3 = (i/hbar)^3 .* (...
(exp(-0.5*((t(a)-t3int)/width).^2) .* ...
exp(-0.5*((t(a)+t23(pop)-t3int-t2int)/width).^2) .* ...
exp(-0.5*((t(a)+t12(coh)+t23(pop)-t3int-t2int-t1int)/width).^2) .* ...
exp(i*(om3+om2-om1)*t3int + i*(om2-om1)*t2int - i*om1*t1int) .* ...
exp(i*weg*t1int-i*weg*t3int) .* ...
((exp(rer2and3((1:m),(1:n),(1:o)) + imr2((1:m),(1:n),(1:o))))...
+(exp(rer2and3((1:m),(1:n),(1:o)) + imr3((1:m),(1:n),(1:o))))...
+(exp(-0.5*((t(a)-t3int)/width).^2) .* ...
exp(-0.5*((t(a)+t23(pop)-t3int-t2int-t1int)/width).^2) .* ...
exp(-0.5*((t(a)+t12(coh)+t23(pop)-t3int-t2int)/width).^2) .* ...
exp(i*(om3+om2-om1)*t3int + i*(om2-om1)*t2int + i*om2*t1int) .* ...
exp(-i*weg*t1int-i*weg*t3int) .* ...
((exp(rer1and4((1:m),(1:n),(1:o)) + imr1((1:m),(1:n),(1:o))))...
+(exp(rer1and4((1:m),(1:n),(1:o)) + imr4((1:m),(1:n),(1:o))))...
+ ((i/hbar)^3 .* (...
(exp(-0.5*((t(a)-t3int-t2int)/width).^2) .* ...
exp(-0.5*((t(a)+t23(pop)-t3int)/width).^2) .* ...
exp(-0.5*((t(a)+t12(coh)+t23(pop)-t3int-t2int-t1int)/width).^2) .* ...
exp(i*(om3+om2-om1)*t3int + i*(om3-om1)*t2int - i*om1*t1int) .* ...
exp(i*weg*t1int-i*weg*t3int) .* ...
((exp(rer2and3((1:m),(1:n),(1:o)) + imr2((1:m),(1:n),(1:o))))...
+(exp(rer2and3((1:m),(1:n),(1:o)) + imr3((1:m),(1:n),(1:o))))...
+(exp(-0.5*((t(a)-t3int-t2int-t1int)/width).^2) .* ...
exp(-0.5*((t(a)+t23(pop)-t3int)/width).^2) .* ...
exp(-0.5*((t(a)+t12(coh)+t23(pop)-t3int-t2int)/width).^2) .* ...
exp(i*(om3+om2-om1)*t3int + i*(om3-om1)*t2int + i*om3*t1int) .* ...
exp(-i*weg*t1int-i*weg*t3int) .* ...
((exp(rer1and4((1:m),(1:n),(1:o)) + imr1((1:m),(1:n),(1:o))))...
+(exp(rer1and4((1:m),(1:n),(1:o)) + imr4((1:m),(1:n),(1:o))))...
));

echo2 = trapz(echo3);
echo1 = trapz(echo2);
P3t(a,pop,coh) = trapz(echo1);
end
end
end

```

A.3 RIRIV.m

```

function [reRIRIV,imRI,imRIV] = RIRIV(kb,T,hbar,w,g,t1,t2,t3,L,D2)
reRIRIV = zeros(size(t1));
imRI = zeros(size(t1));
imRIV = zeros(size(t1));

t4 = t2+t3;
t5 = t1+t2;
t6 = t1+t2+t3;

for u = 1:length(w)
%%%%%%%%%%%%%%%%%%%%%%%%%%%%%%%%%%%%%%%%%%%%%%%%%%%%%%%%%%%%%%%%%%%%%%%%
if w(u) == 0;%Gaussian Mode

reRIRIV = reRIRIV + (D2(u)/(2*g(u).^2)) * (...
-(sqrt(2*pi)*g(u)*t3.*erf(g(u)*t3/sqrt(2)) + ...
  2.*exp(-0.5*t3.^2*g(u).^2) - 2) ...
-(sqrt(2*pi)*g(u)*t1.*erf(g(u)*t1/sqrt(2)) + ...
  2.*exp(-0.5*t1.^2*g(u).^2) - 2) ...
-(sqrt(2*pi)*g(u)*t2.*erf(g(u)*t2/sqrt(2)) + ...
  2.*exp(-0.5*t2.^2*g(u).^2) - 2) ...
+(sqrt(2*pi)*g(u)*t4.*erf(g(u)*t4/sqrt(2)) + ...
  2.*exp(-0.5*t4.^2*g(u).^2) - 2) ...
+(sqrt(2*pi)*g(u)*t5.*erf(g(u)*t5/sqrt(2)) + ...
  2.*exp(-0.5*t5.^2*g(u).^2) - 2) ...
-(sqrt(2*pi)*g(u)*t6.*erf(g(u)*t6/sqrt(2)) + ...
  2.*exp(-0.5*t6.^2*g(u).^2) - 2));

imRI = imRI + (i*L(u)/g(u)) * (...
-(g(u)*t3-sqrt(pi/2)*erf(g(u)*t3/sqrt(2))) ...
+(g(u)*t1-sqrt(pi/2)*erf(g(u)*t1/sqrt(2))) ...
-(g(u)*t2-sqrt(pi/2)*erf(g(u)*t2/sqrt(2))) ...
+(g(u)*t4-sqrt(pi/2)*erf(g(u)*t4/sqrt(2))) ...
-(g(u)*t5-sqrt(pi/2)*erf(g(u)*t5/sqrt(2))) ...
+(g(u)*t6-sqrt(pi/2)*erf(g(u)*t6/sqrt(2))));

imRIV = imRIV + (i*L(u)/g(u)) * (...
+(g(u)*t3-sqrt(pi/2)*erf(g(u)*t3/sqrt(2))) ...
+(g(u)*t1-sqrt(pi/2)*erf(g(u)*t1/sqrt(2))) ...
+(g(u)*t2-sqrt(pi/2)*erf(g(u)*t2/sqrt(2))) ...
-(g(u)*t4-sqrt(pi/2)*erf(g(u)*t4/sqrt(2))) ...
-(g(u)*t5-sqrt(pi/2)*erf(g(u)*t5/sqrt(2))) ...
+(g(u)*t6-sqrt(pi/2)*erf(g(u)*t6/sqrt(2))));

```

```

%%%%%%%%%%%%%%%%%%%%%%%%%%%%%%%%%%%%%%%%%%%%%%%%%%%%%%%%%%%%%%%%%%%%%%%%
elseif w(u) == 1;%Overdamped Mode

reRIRIV = reRIRIV + (D2(u)/g(u).^2) * (...
-exp(-g(u)*t3) + (g(u)*t3 - 1) ...
-exp(-g(u)*t1) + (g(u)*t1 - 1) ...
-exp(-g(u)*t2) + (g(u)*t2 - 1) ...
+exp(-g(u)*t4) + (g(u)*t4 - 1) ...
+exp(-g(u)*t5) + (g(u)*t5 - 1) ...
-exp(-g(u)*t6) + (g(u)*t6 - 1));

imRI = imRI + (i*L(u)/g(u)) * (...
-exp(-g(u)*t3) + (g(u)*t3 - 1) ...
+exp(-g(u)*t1) + (g(u)*t1 - 1) ...
-exp(-g(u)*t2) + (g(u)*t2 - 1) ...
+exp(-g(u)*t4) + (g(u)*t4 - 1) ...
-exp(-g(u)*t5) + (g(u)*t5 - 1) ...
+exp(-g(u)*t6) + (g(u)*t6 - 1));

imRIV = imRIV + (i*L(u)/g(u)) * (...
+exp(-g(u)*t3) + (g(u)*t3 - 1) ...
+exp(-g(u)*t1) + (g(u)*t1 - 1) ...
+exp(-g(u)*t2) + (g(u)*t2 - 1) ...
-exp(-g(u)*t4) + (g(u)*t4 - 1) ...
-exp(-g(u)*t5) + (g(u)*t5 - 1) ...
+exp(-g(u)*t6) + (g(u)*t6 - 1));

%%%%%%%%%%%%%%%%%%%%%%%%%%%%%%%%%%%%%%%%%%%%%%%%%%%%%%%%%%%%%%%%%%%%%%%%
elseif w(u) == 2;%Const. Mode (Inhomogeneous Broadening)

reRIRIV = reRIRIV + D2(u) * (...
-(t3.^2 / 2) ...
-(t1.^2 / 2) ...
-(t2.^2 / 2) ...
+(t4.^2 / 2) ...
+(t5.^2 / 2) ...
-(t6.^2 / 2));

imRI = imRI;

imRIV = imRIV;

%%%%%%%%%%%%%%%%%%%%%%%%%%%%%%%%%%%%%%%%%%%%%%%%%%%%%%%%%%%%%%%%%%%%%%%%

```

else%Underdamped Mode

```

reRIRIV = reRIRIV + (2*D2(u)/(w(u)*(g(u).^2+4*w(u).^2)).* (...
-(2*w(u)*(-3*g(u).^2+g(u).^3*t3+4*w(u).^2+4*g(u)*w(u).^2*t3) + ...
    exp(-g(u)*t3/2)*(6*g(u).^2*w(u)-8*w(u).^3).*cos(w(u)*t3) + ...
    exp(-g(u)*t3/2)*(g(u)*(g(u).^2-12*w(u).^2)).*sin(w(u)*t3)) ...
-(2*w(u)*(-3*g(u).^2+g(u).^3*t1+4*w(u).^2+4*g(u)*w(u).^2*t1) + ...
    exp(-g(u)*t1/2)*(6*g(u).^2*w(u)-8*w(u).^3).*cos(w(u)*t1) + ...
    exp(-g(u)*t1/2)*(g(u)*(g(u).^2-12*w(u).^2)).*sin(w(u)*t1)) ...
-(2*w(u)*(-3*g(u).^2+g(u).^3*t2+4*w(u).^2+4*g(u)*w(u).^2*t2) + ...
    exp(-g(u)*t2/2)*(6*g(u).^2*w(u)-8*w(u).^3).*cos(w(u)*t2) + ...
    exp(-g(u)*t2/2)*(g(u)*(g(u).^2-12*w(u).^2)).*sin(w(u)*t2)) ...
+(2*w(u)*(-3*g(u).^2+g(u).^3*t4+4*w(u).^2+4*g(u)*w(u).^2*t4) + ...
    exp(-g(u)*t4/2)*(6*g(u).^2*w(u)-8*w(u).^3).*cos(w(u)*t4) + ...
    exp(-g(u)*t4/2)*(g(u)*(g(u).^2-12*w(u).^2)).*sin(w(u)*t4)) ...
+(2*w(u)*(-3*g(u).^2+g(u).^3*t5+4*w(u).^2+4*g(u)*w(u).^2*t5) + ...
    exp(-g(u)*t5/2)*(6*g(u).^2*w(u)-8*w(u).^3).*cos(w(u)*t5) + ...
    exp(-g(u)*t5/2)*(g(u)*(g(u).^2-12*w(u).^2)).*sin(w(u)*t5)) ...
-(2*w(u)*(-3*g(u).^2+g(u).^3*t6+4*w(u).^2+4*g(u)*w(u).^2*t6) + ...
    exp(-g(u)*t6/2)*(6*g(u).^2*w(u)-8*w(u).^3).*cos(w(u)*t6) + ...
    exp(-g(u)*t6/2)*(g(u)*(g(u).^2-12*w(u).^2)).*sin(w(u)*t6)));

```

```

imRI = imRI + (i*L(u)/(w(u)*(g(u).^2+4*w(u).^2)).* (...
-(w(u)*(-4*g(u)+g(u).^2*t3+4*w(u).^2*t3) + ...
    exp(-g(u)*t3/2)*4*g(u)*w(u).*cos(w(u)*t3) + ...
    exp(-g(u)*t3/2)*(g(u).^2-4*w(u).^2).*sin(w(u)*t3))...
+(w(u)*(-4*g(u)+g(u).^2*t1+4*w(u).^2*t1) + ...
    exp(-g(u)*t1/2)*4*g(u)*w(u).*cos(w(u)*t1) + ...
    exp(-g(u)*t1/2)*(g(u).^2-4*w(u).^2).*sin(w(u)*t1))...
-(w(u)*(-4*g(u)+g(u).^2*t2+4*w(u).^2*t2) + ...
    exp(-g(u)*t2/2)*4*g(u)*w(u).*cos(w(u)*t2) + ...
    exp(-g(u)*t2/2)*(g(u).^2-4*w(u).^2).*sin(w(u)*t2))...
+(w(u)*(-4*g(u)+g(u).^2*t4+4*w(u).^2*t4) + ...
    exp(-g(u)*t4/2)*4*g(u)*w(u).*cos(w(u)*t4) + ...
    exp(-g(u)*t4/2)*(g(u).^2-4*w(u).^2).*sin(w(u)*t4))...
-(w(u)*(-4*g(u)+g(u).^2*t5+4*w(u).^2*t5) + ...
    exp(-g(u)*t5/2)*4*g(u)*w(u).*cos(w(u)*t5) + ...
    exp(-g(u)*t5/2)*(g(u).^2-4*w(u).^2).*sin(w(u)*t5))...
+(w(u)*(-4*g(u)+g(u).^2*t6+4*w(u).^2*t6) + ...
    exp(-g(u)*t6/2)*4*g(u)*w(u).*cos(w(u)*t6) + ...
    exp(-g(u)*t6/2)*(g(u).^2-4*w(u).^2).*sin(w(u)*t6)));

```

```

imRIV = imRIV + (i*L(u)/(w(u)*(g(u).^2+4*w(u).^2)).* (...
+(w(u)*(-4*g(u)+g(u).^2*t3+4*w(u).^2*t3) + ...

```

```

exp(-g(u)*t3/2)*4*g(u)*w(u).*cos(w(u)*t3) + ...
exp(-g(u)*t3/2)*(g(u).^2-4*w(u).^2).*sin(w(u)*t3))...
+(w(u)*(-4*g(u)+g(u).^2*t1+4*w(u).^2*t1) + ...
exp(-g(u)*t1/2)*4*g(u)*w(u).*cos(w(u)*t1) + ...
exp(-g(u)*t1/2)*(g(u).^2-4*w(u).^2).*sin(w(u)*t1))...
+(w(u)*(-4*g(u)+g(u).^2*t2+4*w(u).^2*t2) + ...
exp(-g(u)*t2/2)*4*g(u)*w(u).*cos(w(u)*t2) + ...
exp(-g(u)*t2/2)*(g(u).^2-4*w(u).^2).*sin(w(u)*t2))...
-(w(u)*(-4*g(u)+g(u).^2*t4+4*w(u).^2*t4) + ...
exp(-g(u)*t4/2)*4*g(u)*w(u).*cos(w(u)*t4) + ...
exp(-g(u)*t4/2)*(g(u).^2-4*w(u).^2).*sin(w(u)*t4))...
-(w(u)*(-4*g(u)+g(u).^2*t5+4*w(u).^2*t5) + ...
exp(-g(u)*t5/2)*4*g(u)*w(u).*cos(w(u)*t5) + ...
exp(-g(u)*t5/2)*(g(u).^2-4*w(u).^2).*sin(w(u)*t5))...
+(w(u)*(-4*g(u)+g(u).^2*t6+4*w(u).^2*t6) + ...
exp(-g(u)*t6/2)*4*g(u)*w(u).*cos(w(u)*t6) + ...
exp(-g(u)*t6/2)*(g(u).^2-4*w(u).^2).*sin(w(u)*t6)));

end
end

```

A.4 RIIRIII.m

```

function [reRIIRIII,imRII,imRIII] = RIIRIII(kb,T,hbar,w,g,t1,t2,t3,L,D2)
reRIIRIII = zeros(size(t1));
imRII = zeros(size(t1));
imRIII = zeros(size(t1));

t4 = t2+t3;
t5 = t1+t2;
t6 = t1+t2+t3;

for u = 1:length(w)
%%%%%%%%%%%%%%%%%%%%%%%%%%%%%%%%%%%%%%%%%%%%%%%%%%%%%%%%%%%%%%%%%%%%%%%%
if w(u) == 0;%Gaussian Mode

reRIIRIII = reRIIRIII + (D2(u)/(2*g(u).^2)) * (...
-(sqrt(2*pi)*g(u)*t3.*erf(g(u)*t3/sqrt(2)) + ...
  2.*exp(-0.5*t3.^2*g(u).^2) - 2) ...
-(sqrt(2*pi)*g(u)*t1.*erf(g(u)*t1/sqrt(2)) + ...
  2.*exp(-0.5*t1.^2*g(u).^2) - 2) ...
+(sqrt(2*pi)*g(u)*t2.*erf(g(u)*t2/sqrt(2)) + ...
  2.*exp(-0.5*t2.^2*g(u).^2) - 2) ...
-(sqrt(2*pi)*g(u)*t4.*erf(g(u)*t4/sqrt(2)) + ...
  2.*exp(-0.5*t4.^2*g(u).^2) - 2) ...
-(sqrt(2*pi)*g(u)*t5.*erf(g(u)*t5/sqrt(2)) + ...
  2.*exp(-0.5*t5.^2*g(u).^2) - 2) ...
+(sqrt(2*pi)*g(u)*t6.*erf(g(u)*t6/sqrt(2)) + ...
  2.*exp(-0.5*t6.^2*g(u).^2) - 2));

imRII = imRII + (i*L(u)/g(u)) * (...
-(g(u)*t3-sqrt(pi/2)*erf(g(u)*t3/sqrt(2))) ...
-(g(u)*t1-sqrt(pi/2)*erf(g(u)*t1/sqrt(2))) ...
-(g(u)*t2-sqrt(pi/2)*erf(g(u)*t2/sqrt(2))) ...
+(g(u)*t4-sqrt(pi/2)*erf(g(u)*t4/sqrt(2))) ...
-(g(u)*t5-sqrt(pi/2)*erf(g(u)*t5/sqrt(2))) ...
+(g(u)*t6-sqrt(pi/2)*erf(g(u)*t6/sqrt(2))));

imRIII = imRIII + (i*L(u)/g(u)) * (...
+(g(u)*t3-sqrt(pi/2)*erf(g(u)*t3/sqrt(2))) ...
-(g(u)*t1-sqrt(pi/2)*erf(g(u)*t1/sqrt(2))) ...
+(g(u)*t2-sqrt(pi/2)*erf(g(u)*t2/sqrt(2))) ...
-(g(u)*t4-sqrt(pi/2)*erf(g(u)*t4/sqrt(2))) ...
-(g(u)*t5-sqrt(pi/2)*erf(g(u)*t5/sqrt(2))) ...
+(g(u)*t6-sqrt(pi/2)*erf(g(u)*t6/sqrt(2))));

```

```

%%%%%%%%%%%%%%%%%%%%%%%%%%%%%%%%%%%%%%%%%%%%%%%%%%%%%%%%%%%%%%%%%%%%%%%%
elseif w(u) == 1;%Overdamped Mode

reRIIRIII = reRIIRIII + (D2(u)/g(u).^2) * (...
-exp(-g(u)*t3) + (g(u)*t3) - 1) ...
-exp(-g(u)*t1) + (g(u)*t1) - 1) ...
+(exp(-g(u)*t2) + (g(u)*t2) - 1) ...
-(exp(-g(u)*t4) + (g(u)*t4) - 1) ...
-(exp(-g(u)*t5) + (g(u)*t5) - 1) ...
+(exp(-g(u)*t6) + (g(u)*t6) - 1));

imRII = imRII + (i*L(u)/g(u)) * (...
-exp(-g(u)*t3) + (g(u)*t3) - 1) ...
-exp(-g(u)*t1) + (g(u)*t1) - 1) ...
-(exp(-g(u)*t2) + (g(u)*t2) - 1) ...
+(exp(-g(u)*t4) + (g(u)*t4) - 1) ...
-(exp(-g(u)*t5) + (g(u)*t5) - 1) ...
+(exp(-g(u)*t6) + (g(u)*t6) - 1));

imRIII = imRIII + (i*L(u)/g(u)) * (...
+(exp(-g(u)*t3) + (g(u)*t3) - 1) ...
-(exp(-g(u)*t1) + (g(u)*t1) - 1) ...
+(exp(-g(u)*t2) + (g(u)*t2) - 1) ...
-(exp(-g(u)*t4) + (g(u)*t4) - 1) ...
-(exp(-g(u)*t5) + (g(u)*t5) - 1) ...
+(exp(-g(u)*t6) + (g(u)*t6) - 1));

%%%%%%%%%%%%%%%%%%%%%%%%%%%%%%%%%%%%%%%%%%%%%%%%%%%%%%%%%%%%%%%%%%%%%%%%
elseif w(u) == 2;%Const. Mode (Inhomogeneous Broadening)

reRIIRIII = reRIIRIII + D2(u) * (...
-(t3.^2 / 2) ...
-(t1.^2 / 2) ...
+(t2.^2 / 2) ...
-(t4.^2 / 2) ...
-(t5.^2 / 2) ...
+(t6.^2 / 2));

imRII = imRII;

imRIII = imRIII;

%%%%%%%%%%%%%%%%%%%%%%%%%%%%%%%%%%%%%%%%%%%%%%%%%%%%%%%%%%%%%%%%%%%%%%%%

```

else%Underdamped Mode

```

reRIIRIII = reRIIRIII + (2*D2(u)/(w(u)*(g(u).^2+4*w(u).^2).^2)) .* (...
-(2*w(u)*(-3*g(u).^2+g(u).^3*t3+4*w(u).^2+4*g(u)*w(u).^2*t3) + ...
    exp(-g(u)*t3/2)*(6*g(u).^2*w(u)-8*w(u).^3).*cos(w(u)*t3) + ...
    exp(-g(u)*t3/2)*(g(u)*(g(u).^2-12*w(u).^2)).*sin(w(u)*t3)) ...
-(2*w(u)*(-3*g(u).^2+g(u).^3*t1+4*w(u).^2+4*g(u)*w(u).^2*t1) + ...
    exp(-g(u)*t1/2)*(6*g(u).^2*w(u)-8*w(u).^3).*cos(w(u)*t1) + ...
    exp(-g(u)*t1/2)*(g(u)*(g(u).^2-12*w(u).^2)).*sin(w(u)*t1)) ...
+(2*w(u)*(-3*g(u).^2+g(u).^3*t2+4*w(u).^2+4*g(u)*w(u).^2*t2) + ...
    exp(-g(u)*t2/2)*(6*g(u).^2*w(u)-8*w(u).^3).*cos(w(u)*t2) + ...
    exp(-g(u)*t2/2)*(g(u)*(g(u).^2-12*w(u).^2)).*sin(w(u)*t2)) ...
-(2*w(u)*(-3*g(u).^2+g(u).^3*t4+4*w(u).^2+4*g(u)*w(u).^2*t4) + ...
    exp(-g(u)*t4/2)*(6*g(u).^2*w(u)-8*w(u).^3).*cos(w(u)*t4) + ...
    exp(-g(u)*t4/2)*(g(u)*(g(u).^2-12*w(u).^2)).*sin(w(u)*t4)) ...
-(2*w(u)*(-3*g(u).^2+g(u).^3*t5+4*w(u).^2+4*g(u)*w(u).^2*t5) + ...
    exp(-g(u)*t5/2)*(6*g(u).^2*w(u)-8*w(u).^3).*cos(w(u)*t5) + ...
    exp(-g(u)*t5/2)*(g(u)*(g(u).^2-12*w(u).^2)).*sin(w(u)*t5)) ...
+(2*w(u)*(-3*g(u).^2+g(u).^3*t6+4*w(u).^2+4*g(u)*w(u).^2*t6) + ...
    exp(-g(u)*t6/2)*(6*g(u).^2*w(u)-8*w(u).^3).*cos(w(u)*t6) + ...
    exp(-g(u)*t6/2)*(g(u)*(g(u).^2-12*w(u).^2)).*sin(w(u)*t6)));

```

```

imRII = imRII + (i*L(u)/(w(u)*(g(u).^2+4*w(u).^2))) .* (...
-(w(u)*(-4*g(u)+g(u).^2*t3+4*w(u).^2*t3) + ...
    exp(-g(u)*t3/2)*4*g(u)*w(u).*cos(w(u)*t3) + ...
    exp(-g(u)*t3/2)*(g(u).^2-4*w(u).^2).*sin(w(u)*t3))...
-(w(u)*(-4*g(u)+g(u).^2*t1+4*w(u).^2*t1) + ...
    exp(-g(u)*t1/2)*4*g(u)*w(u).*cos(w(u)*t1) + ...
    exp(-g(u)*t1/2)*(g(u).^2-4*w(u).^2).*sin(w(u)*t1))...
-(w(u)*(-4*g(u)+g(u).^2*t2+4*w(u).^2*t2) + ...
    exp(-g(u)*t2/2)*4*g(u)*w(u).*cos(w(u)*t2) + ...
    exp(-g(u)*t2/2)*(g(u).^2-4*w(u).^2).*sin(w(u)*t2))...
+(w(u)*(-4*g(u)+g(u).^2*t4+4*w(u).^2*t4) + ...
    exp(-g(u)*t4/2)*4*g(u)*w(u).*cos(w(u)*t4) + ...
    exp(-g(u)*t4/2)*(g(u).^2-4*w(u).^2).*sin(w(u)*t4))...
-(w(u)*(-4*g(u)+g(u).^2*t5+4*w(u).^2*t5) + ...
    exp(-g(u)*t5/2)*4*g(u)*w(u).*cos(w(u)*t5) + ...
    exp(-g(u)*t5/2)*(g(u).^2-4*w(u).^2).*sin(w(u)*t5))...
+(w(u)*(-4*g(u)+g(u).^2*t6+4*w(u).^2*t6) + ...
    exp(-g(u)*t6/2)*4*g(u)*w(u).*cos(w(u)*t6) + ...
    exp(-g(u)*t6/2)*(g(u).^2-4*w(u).^2).*sin(w(u)*t6)));

```

```

imRIII = imRIII + (i*L(u)/(w(u)*(g(u).^2+4*w(u).^2))) .* (...
+(w(u)*(-4*g(u)+g(u).^2*t3+4*w(u).^2*t3) + ...

```

```

exp(-g(u)*t3/2)*4*g(u)*w(u).*cos(w(u)*t3) + ...
exp(-g(u)*t3/2)*(g(u).^2-4*w(u).^2).*sin(w(u)*t3))...
-(w(u)*(-4*g(u)+g(u).^2*t1+4*w(u).^2*t1) + ...
exp(-g(u)*t1/2)*4*g(u)*w(u).*cos(w(u)*t1) + ...
exp(-g(u)*t1/2)*(g(u).^2-4*w(u).^2).*sin(w(u)*t1))...
+(w(u)*(-4*g(u)+g(u).^2*t2+4*w(u).^2*t2) + ...
exp(-g(u)*t2/2)*4*g(u)*w(u).*cos(w(u)*t2) + ...
exp(-g(u)*t2/2)*(g(u).^2-4*w(u).^2).*sin(w(u)*t2))...
-(w(u)*(-4*g(u)+g(u).^2*t4+4*w(u).^2*t4) + ...
exp(-g(u)*t4/2)*4*g(u)*w(u).*cos(w(u)*t4) + ...
exp(-g(u)*t4/2)*(g(u).^2-4*w(u).^2).*sin(w(u)*t4))...
-(w(u)*(-4*g(u)+g(u).^2*t5+4*w(u).^2*t5) + ...
exp(-g(u)*t5/2)*4*g(u)*w(u).*cos(w(u)*t5) + ...
exp(-g(u)*t5/2)*(g(u).^2-4*w(u).^2).*sin(w(u)*t5))...
+(w(u)*(-4*g(u)+g(u).^2*t6+4*w(u).^2*t6) + ...
exp(-g(u)*t6/2)*4*g(u)*w(u).*cos(w(u)*t6) + ...
exp(-g(u)*t6/2)*(g(u).^2-4*w(u).^2).*sin(w(u)*t6)));

end
end

```